Università degli studi di Bologna

Facoltà di Scienze Matematiche Fisiche e Naturali

Dottorato di Ricerca in Fisica
XVII ciclo

Study of the pion identification in the Emulsion Cloud Chambers of the OPERA experiment

Author: **Michela Cozzi**

Advisors:

Prof. Giorgio Giacomelli

Dott. Gianni Mandrioli

Dott. Maximiliano Sioli

PhD Coordinator:

Prof. Roberto Soldati

Bologna, Marzo 2005

Contents

Introduction

The Standard Model of particle physics includes neutrinos as massless particles and only left-handed neutrinos and right-handed antineutrinos are considered. A clear signature of non-zero neutrino mass is provided by neutrino oscillations. The possibility of such oscillations was first investigated by Bruno Pontecorvo in 1958 [1] in the form of neutrino-antineutrino oscillations, similar to the oscillations of neutral kaons. After the discovery of muon neutrinos, the idea was also extended to oscillations among different flavors.

Increasing evidences for neutrino oscillations, and hence for non-zero ν masses, obtained in the last decade, could be an indication for physics beyond the Standard Model or, at least, would force an extension of the Standard Model in order to accommodate a neutrino mass term.

The first indication of neutrino oscillations came in the 70s from the observations of a deficit of the solar neutrino flux measured on Earth. Later on, other experimental results on solar neutrinos reinforced the hypothesis of flavor oscillations. Nowadays the accepted interpretation of the solar neutrino problem is the flavor oscillation in matter with a mass-square difference parameter of the order of 10^{-5}eV^2 and a relatively large mixing angle between mass and flavor eigenstates.

Other indications for ν oscillations came from atmospheric neutrinos in the 80's. More recently, other experimental results reinforced the evidence for an atmospheric neutrino anomaly. The most favourable and accepted explanation of this phenomenon is $\nu_\mu \rightarrow \nu_\tau$ oscillations; other oscillation hypothesis like $\nu_\mu \rightarrow \nu_e$, $\nu_\mu \rightarrow \nu_{sterile}$, Lorentz invariance violation induced oscillations, etc. are strongly disfavoured. How-

ever, even if the $\nu_\mu \rightarrow \nu_\tau$ oscillation hypothesis seems nowadays very probable, a direct observation of the ν_τ appearance is still missing. This would constitute the definite proof of ν oscillation.

OPERA plans to prove the neutrino oscillation conjecture in an unambiguous way, with the observation of the appearance of ν_τs in a pure ν_μ beam. The production and the decay of the τ lepton will be observed thanks to the excellent space resolution of nuclear emulsions. OPERA is a hybrid experiment with electronic detectors used to locate possible candidates and nuclear emulsions to precisely measure their features. The use of emulsions is based on the concept of the Emulsion Cloud Chambers (ECC), a sandwich of dense passive material plates (lead) and of emulsion sheets, disposed in structures called *bricks*. In this way, the need of both a large mass and high precision track capability to detect τ decays, will be satisfied simultaneously.

The large scale of the experiment translates in a large amount of emulsion plates to be scanned with optical microscopes. This scenario boosted a large R&D effort inside the Collaboration in order to automatize as much as possible data acquisition and online reconstruction. Part of the work presented here has been devoted to the set-up, calibration and test of an automatic, computer driven, high-speed scanning system in the Bologna Lab. Performances of the system, in terms of scanning speed, efficiencies and purity, will be presented. The optimization and calibration of the automatic microscope were obtained with dedicated test beam exposures at the CERN PS, where emulsion bricks have been exposed to a flux of pions incidents at different angles.

The main part of this work focuses on the experimental study of pion-electron separation capability using OPERA ECC bricks. Most of the estimated performances of the OPERA experiment (including detection efficiencies and background sources) are based on detailed Monte Carlo simulations, tuned with available experimental data. In the case of pion-electron identification an extensive study is missing, since the current estimates are based directly or indirectly on Monte Carlo simulations.

For this purpose, we exposed nuclear emulsion bricks to pure pion beams at different energies. We developed a dedicated code to propagate events inside the brick and an identification algorithm based on the different behaviours of energy losses suffered by electrons and hadrons in matter. The same algorithm has been applied to data of pure electrons, which have been collected in a complementary test beam exposure at DESY during the same period [2].

These data, both from pion and electron exposures, have been analysed in [2] in a different and complementary way, using the information from the shower development along the ECC bricks. Finally the results will be presented and compared together.

This thesis is organized as follows.

The formalism of neutrino mass, mixing and oscillations is introduced in the first chapter, while the second chapter summarize the main experimental results and their implications for neutrino physics.

The OPERA experiment, its layout, the estimated performances and sensitivity to oscillation parameters are presented in the third chapter; the fourth chapter illustrates nuclear emulsions properties and their use in OPERA.

The automatic scanning system installed in the Bologna Lab. is fully described in the fifth chapter, where performances, scanning speed, efficiencies and purity are reported.

In the last chapter we describe the pion exposure at CERN for the study of pion-electron separation and we report the results of the work.

Chapter 1

Neutrino masses and oscillations

The neutrino was the first particle proposed by a theorist to guarantee the validity of a symmetry principle: Pauli suggested [3] that neutrinos (invisible then and remaining so for another 25 years) are emitted together with electrons in nuclear beta decays to conserve both energy and angular momentum.

The Standard Model of electroweak interactions, developed in the late 1960's [4], provided a theoretical framework to incorporate neutrinos as left-handed (LH) partners to the charged leptons. In particular, neutrinos were thought to be massless, following the so-called two-component theory of Landau [5] and Lee and Yang [6], in which the massless neutrinos are described by left-handed Weyl spinors. This description has been reproduced in the Standard Model assuming the non existence of right-handed (RH) neutrino fields, which are necessary in order to generate Dirac neutrino masses with the same Higgs mechanism that generates the Dirac masses of quarks and charged leptons.

After the successes of the theory of the big-bang nucleosynthesis (BBN) and the discovery of the Cosmic Microwave Background, it became clear that neutrinos could be potentially major players in the history of the early universe. The increasing evidence for the existence (and dominance) of dark matter in the universe led to the hypothesis that neutrinos, with small but finite mass, could provide at least part of the dark matter mass. This possibility determined a large experimental effort on the issue of neutrino mass and its role in cosmology, and provided substantial impetus

to a worldwide program of experiments addressing the issue of finite neutrino mass and the possibility of mixing between lepton families.

Although it now appears that neutrinos are not likely the main source of dark matter in the universe and the neutrino oscillation hypothesis is still waiting for its final confirmation, the experimental evidence obtained in the last decade for finite neutrino mass and mixing between generations is strong.

The existence of neutrino oscillations requires a change in the Standard Model in order to accommodate three massive neutrinos, three mixing angles and one Dirac-type CP-phase. If neutrinos are Majorana particles, also other two Majorana phases enter in the extension of the Standard Model.

Neutrino masses are peculiar because they are at least five orders of magnitude smaller than the mass of the electron. The most popular explanation of the small neutrino masses is the "see-saw mechanism" in which the neutrino masses are inversely proportional to some large mass scale. If that explanation of the small neutrino mass is true, then the experimentally observed neutrinos are Majorana particles (i.e. indistinguishable from their own antiparticles), and hence the total lepton number is not conserved.

1.1 The neutrino mass term

In a field theory the mass is determined by the mass term in the Lagrangian. Let us suppose that we now try to extend the SM to accommodate a nonzero mass for neutrinos in the same way that the SM already accommodates nonzero masses for quarks and charged leptons. The latter masses are all of Dirac type and arise from Yukawa coupling of the form:

$$- f_q \varphi \overline{q_L} q_R + h.c. \tag{1.1}$$

Here, q is some quark, φ is the neutral Higgs field and f_q is a coupling constant.

When φ develops a vacuum expectation value $\langle\varphi\rangle_0$, the coupling (1.1) yields a term

$$- f_q \langle\varphi\rangle_0 \overline{q_L} q_R + h.c. \tag{1.2}$$

This is a Dirac mass term for the quark q, and $f_q \langle\varphi\rangle_0$ is the corresponding mass. Extending the SM to include neutrino masses that parallel the masses of the quarks (and charged leptons) is a simple matter of adding to the model a right-handed neutrino field ν_R and a Yukawa coupling $-f_\nu \varphi \overline{\nu_L} \nu_R + h.c.$, where f_ν is a suitable coupling constant. When φ develops its vacuum expectation value, this coupling will yield a Dirac mass term

$$\mathcal{L}_D = -f_\nu \langle\varphi\rangle_0 \overline{\nu_L} \nu_R + h.c. \tag{1.3}$$

which provides a neutrino mass $m_\nu = f_\nu \langle\varphi\rangle_0$. Now suppose, for example, that m_ν is of the order 0.05 eV, the neutrino mass scale suggested by the observed atmospheric neutrino oscillations. Since the vacuum expectation value of the Higgs field is $\langle\varphi\rangle_0 = 174$ GeV, the coupling f_ν must then be of the order of 10^{-13}. Such a small coupling constant, even if acceptable in principle, is unlikely to be the ultimate explanation of neutrino mass.

In 1937 Majorana [7] discovered that a massive neutral fermion such as a neutrino can be described by a spinor ψ with only two independent components imposing the so-called Majorana condition:

$$\psi = \psi^c \tag{1.4}$$

where $\psi^c = C\overline{\psi}^T$ is the operation of charge conjugation (C is the charge conjugation matrix).

It can be shown that the right-handed component ψ_R of a Majorana neutrino field ψ is not independent from the left-handed component ($\psi_R = \psi_L^c$ and vice-versa). The majorana field can be re-expressed as

$$\psi = \psi_L + \psi_L^c = \psi_R^c + \psi_R \tag{1.5}$$

A Majorana mass term may be constructed out of ν_L alone, in which case we have "left-handed Majorana mass":

$$\mathcal{L}_{M_L} = -\frac{m_L}{2} \overline{\nu_L}^c \nu_L + h.c. \tag{1.6}$$

or out of ν_R alone, in which case we have the "right-handed Majorana mass"

$$\mathcal{L}_{M_R} = -\frac{m_R}{2}\overline{\nu_R}^c \nu_R + h.c. \tag{1.7}$$

An electrically charged fermion cannot have a Majorana mass term, because such a term would convert it into an antifermion, in violation of electric charge conservation. However, for electrically neutral neutrinos, once the field ν_R exists, there is nothing in the SM to prevent the occurrence of a right-handed Majorana mass term: such a term does not violate neither the conservation of weak isospin nor that of electric charge. Consequently, if nature contains a Dirac neutrino mass term, then it is likely that it contains a Majorana mass term as well. And, needless to say, if the neutrino does not contain a Dirac neutrino mass term, then it certainly contains a Majorana mass term, which would then be the only source of neutrino mass.

Suppose that a neutrino has a Dirac mass, like for quarks and charged leptons, and also a right-handed Majorana mass as in (1.7). Its total mass term $\mathcal{L}_{m_\nu}$ is then

$$\begin{aligned} \mathcal{L}_{m_\nu} &= -m_D\overline{\nu_R}\nu_L - (m_R/2)\overline{\nu_R}^c\nu_R + h.c. \\ &= -\tfrac{1}{2}\left[\overline{\nu_L}^c, \overline{\nu_R}\right]\begin{bmatrix} 0 & m_D \\ m_D & m_R \end{bmatrix}\begin{bmatrix} \nu_L \\ \nu_R^c \end{bmatrix} + h.c. \end{aligned} \tag{1.8}$$

The matrix $\mathcal{M}_\nu$

$$\mathcal{M}_\nu = \begin{bmatrix} 0 & m_D \\ m_D & m_R \end{bmatrix} \tag{1.9}$$

appearing in $\mathcal{L}_{m_\nu}$ is called the neutrino mass matrix.

1.2 The see-saw mechanism

It is natural to assume that the neutrino Dirac mass m_D is of the same order of magnitude as the Dirac masses of the quarks and charged leptons, since in the SM all Dirac masses arise from coupling to the same Higgs field. The Dirac masses of the quarks and charged leptons are their total masses, so we expect m_D to be of the same order of magnitude as the mass of a typical quark or charged lepton.

Furthermore, since nothing in the SM requires the right-handed Majorana mass m_R to be small, one may expect that this mass could be "large": $m_R \gg m_D$.

The mass matrix $\mathcal{M}_\nu$ can be diagonalized by the transformation

$$Z^T \mathcal{M}_\nu Z = \mathcal{D}_\nu \tag{1.10}$$

where

$$\mathcal{D}_\nu = \begin{bmatrix} m_1 & 0 \\ 0 & m_2 \end{bmatrix} \tag{1.11}$$

is a diagonal matrix whose diagonals elements are the positive-definite eigenvalues of $\mathcal{M}_\nu$, Z is a unitary matrix and T denotes transposition. To first order in the small parameter $\rho \equiv m_D/m_R$,

$$Z = \begin{bmatrix} 1 & \rho \\ -\rho & 1 \end{bmatrix} \begin{bmatrix} i & 0 \\ 0 & 1 \end{bmatrix} \tag{1.12}$$

Using this Z in (1.10), we find that, to order ρ^2,

$$\mathcal{D}_\nu = \begin{bmatrix} m_D^2/m_R & 0 \\ 0 & m_R \end{bmatrix} \tag{1.13}$$

Thus the mass eigenvalues are $m_1 \simeq m_D^2/m_R$ and $m_2 \simeq m_R$.

To express $\mathcal{L}_{m_\nu}$ in terms of mass eigenfields, we define the two-component column vector ν_L by

$$\nu_L \equiv Z^{-1} \begin{bmatrix} \nu_L \\ \nu_R^c \end{bmatrix} \tag{1.14}$$

(The column-vector field ν_L is chirally left-handed, since by definition the charge conjugate of a field with a given chirality always has the opposite chirality.) We then define the two-component field ν, with components ν_{light} and ν_{heavy}, by

$$\nu \equiv \nu_L + \nu_L^c \equiv \begin{bmatrix} \nu_{light} \\ \nu_{heavy} \end{bmatrix} \tag{1.15}$$

(the meaning of the subscripts *light* and *heavy* will become clear in the following). Using the fact that scalar covariant combinations of fermion fields can connect only fields of opposite chirality, the $\mathcal{L}_{m_\nu}$ of (1.8) may be rewritten as

$$\mathcal{L}_{m_\nu} = -\sum_{i=light}^{heavy} \frac{m_i}{2} \overline{\nu_i}\, \nu_i + h.c. \tag{1.16}$$

We recognize the i-th term of this expression as the mass term for a neutrino ν_i.

From the definition (1.15), $\nu_i = \nu_{Li} + \nu_{Li}^c$ goes into itself under charge conjugation. A neutrino whose field has this property is identical to its antiparticle, and is known as a Majorana neutrino. Thus, the eigenstates of the combined Dirac-Majorana mass term $\mathcal{L}_{m_\nu}$ of (1.8) are Majorana neutrinos.

As we have seen, with m_D of the order of the mass of a typical quark or charged leptons, and $m_R \gg m_D$, the mass of ν_{light},

$$m_{light} \cong m_D^2/m_R \tag{1.17}$$

can be very small. Thus, if we define ν_{light} as one of the light neutrinos, we have an elegant explanation of why it is so light. This explanation, in which physical neutrino masses are so small because the right-handed Majorana mass m_R is large, is know as the *see-saw mechanism*, and (1.17) is referred to as the see-saw relation [8]. The mass m_R is assumed to reflect some high mass scale where new physics responsible for neutrino mass resides. Interestingly, if m_R is just a little below the grand unification scale, e.g. $m_R \sim 10^{15}$ GeV, and $m_D \sim m_{top} \simeq 175$ GeV, then from the see-saw relation (1.17) we obtain $m_{light} \sim 3 \times 10^{-2}$ eV. This is in the range of neutrino mass suggested by the experiments on atmospheric neutrino oscillations.

Under these assumptions about m_D and m_R, the mass of ν_h is very large

$$m_{heavy} \cong m_R \tag{1.18}$$

The eigenstate ν_{heavy} cannot be one of the light neutrinos, but is an hypothetical very heavy neutral lepton. Such neutral leptons are candidates to explain the baryon-antibaryon asymmetry of the Universe.

The seesaw mechanism predicts that light neutrinos such as ν_{light}, as well as the hypothetical heavy neutral leptons such as ν_{heavy}, are Majorana particles. The prediction of light neutrinos of this model is one of the factors driving a major effort to look for neutrinoless double beta decay. This is the $L-$violating decay $A \to A' + 2e^-$ in which one nucleus decays to another plus two electrons, with no emission of neutrinos. The observation of this reaction would show that the light neutrinos are indeed Majorana particles [9].

1.3 Three-neutrino mixing

So far, we have analyzed the simplified case in which there is only one light neutrino and one heavy neutral lepton. In the real world, there are three leptonic generations, with a light neutrino in each one. The analysis could be extended to accommodate this situation.[1]

In the SM, there are left-handed weak-eigenstate charged leptons $l_{L\alpha}$, where $\alpha = e, \mu$, or τ. Each of them couples to an LH weak-eigenstate neutrino $\nu_{L\alpha}$, via the charged-current weak interaction

$$\mathcal{L}_W = -(g/\sqrt{2})W_\rho^- \sum_{\alpha=e,\mu,\tau} \overline{l_{L\alpha}}\gamma^\rho \nu_{L\alpha} + h.c. \tag{1.19}$$

Here, W_ρ are the charged weak bosons and g is the weak coupling constant. To allow for neutrino masses, we add to the model the RH fields $\nu_{R\alpha}$, where $\alpha = e, \mu$, or τ. Then, in analogy with (1.8), we introduce the neutrino mass term

$$\mathcal{L}_{m_\nu} = -\frac{1}{2}\,[\overline{\nu_L}^c, \overline{\nu_R}] \begin{bmatrix} 0 & m_D^T \\ m_D & m_R \end{bmatrix} \begin{bmatrix} \nu_L \\ \nu_R^c \end{bmatrix} + h.c. \tag{1.20}$$

In this case, ν_L is the column vector

$$\nu_L \equiv \begin{bmatrix} \nu_{Le} \\ \nu_{L\mu} \\ \nu_{L\tau} \end{bmatrix} \tag{1.21}$$

and similarly for ν_R. The quantities m_D and m_R are now 3×3 matrices. Since the matrix m_R may be taken to be symmetric, the 6×6 mass matrix

$$\mathcal{M}_\nu = \begin{bmatrix} 0 & m_D^T \\ m_D & m_R \end{bmatrix} \tag{1.22}$$

is also symmetric. Such a matrix may be diagonalized by the transformation in (1.10), but where Z is a 6×6 unitary matrix and $\mathcal{D}_\nu$ is a 6×6 diagonal matrix whose diagonal elements m_i, $i = 1, ..., 6$, are positive-definite eigenvalues of the $\mathcal{M}_\nu$ defined in (1.22).

[1] For simplicity, the possibility with light sterile neutrinos in addiction to the three light active ones is not included.

To re-express $\mathcal{M}_\nu$ in term of mass-eigenstate neutrinos, we introduce the column vector ν_L via (1.14) as before. In that relation ν_L and ν_R^c each now have three components, Z is a 6×6 matrix, and ν_L has six components. We then introduce the field ν via a six-component version of (1.15):

$$\nu \equiv \nu_L + \nu_L^c \equiv \begin{bmatrix} \nu_1 \\ \nu_2 \\ \vdots \\ \nu_6 \end{bmatrix} \tag{1.23}$$

It can be shown, as before, that the mass term $\mathcal{M}_\nu$ of (1.20) may be rewritten as

$$\mathcal{L}_{m_\nu} = -\sum_{i=1}^{6} \frac{m_i}{2} \overline{\nu_i} \nu_i + h.c. \tag{1.24}$$

Thus, the ν_i are the neutrinos of definite mass, the mass of ν_i being m_i. From (1.23), we see that each ν_i is a Majorana neutrino.

To complete the treatment of the leptonic sector, we introduce for the charged leptons a Dirac mass term $\mathcal{L}_{m_l}$:

$$\mathcal{L}_{m_l} = -\overline{l_R} \mathcal{M}_l l_L + h.c. \tag{1.25}$$

Here,

$$l_L \equiv \begin{bmatrix} l_{Le} \\ l_{L\mu} \\ l_{L\tau} \end{bmatrix} \tag{1.26}$$

is a column vector whose αth component is the LH weak-eigenstate charged lepton field $l_{L\alpha}$. The quantity l_R is an analogous column vector whose α^{th} component is the RH weak isospin singlet charged lepton field $l_{R\alpha}$. Finally, $\mathcal{M}_l$ is the 3×3 charged lepton mass matrix. This matrix may be diagonalized by the transformation:

$$\overline{A_R}^T \mathcal{M}_l A_L = \mathcal{D}_l \tag{1.27}$$

where $A_{L,R}$ are two distinct 3×3 unitary matrices, and

$$\mathcal{D}_l = \begin{pmatrix} m_e & 0 & 0 \\ 0 & m_\mu & 0 \\ 0 & 0 & m_\tau \end{pmatrix} \tag{1.28}$$

is the diagonal matrix whose diagonal elements are the charged-lepton masses.

If we define the three-component column vector

$$l_{L,R} = A_{L,R} l_{L,R} \tag{1.29}$$

and then introduce the vector $l \equiv l_L + l_R$ we find that

$$\mathcal{L}_{m_l} = -\bar{l}\mathcal{D}_l l = -\sum_{\alpha=e,\mu,\tau} \overline{l_\alpha} m_\alpha l_\alpha \tag{1.30}$$

Thus, the components l_α of the vector l are the charged leptons of definite mass: e, μ, and τ.

To recast the SM weak interaction $\mathcal{L}_W$ in terms of mass eigenstates, it is convenient to write the 6×6 matrix Z in the form

$$Z = \begin{bmatrix} V & Y \\ X & W \end{bmatrix} \tag{1.31}$$

in which V, Y, X and W are 3×3 sub matrices. If the Dirac mass matrix m_D is much smaller than the Majorana mass matrix m_R, then X and Y are much smaller than V and W for the same reason as the off-diagonal elements of the 2×2 version of Z, are small. Similarly, from (1.13) we may conclude that in the three generation, six-neutrino case, the first three neutrinos, $\nu_{1,2,3}$, are light, but the second three, $\nu_{4,5,6}$ are very heavy. Also in this general case, we call the first three neutrinos $\nu_{1,2,3}^{light}$, and the second three $\nu_{4,5,6}^{heavy}$.

From experimental searches for heavy neutral leptons, we know that there are none with masses below 80 GeV [10]. Thus, in neutrino experiments at energies less than this (and even at much higher energies if the heavy neutrinos are at the TeV or even at the grand unification scale), it is only the light neutrinos that play a significant role. Now from the 6×6 analogue of (1.14) and from (1.31),

$$\nu_{L\alpha} = \sum_{i=1}^{3} \left(V_{\alpha i} \nu_{Li}^{light} + Y_{\alpha i} \nu_{Li}^{heavy} \right) \cong \sum_{i=1}^{3} V_{\alpha i} \nu_{Li}^{light} \tag{1.32}$$

where we have used $V \gg Y$ in the second step. This scenario, called *three-neutrino mixing* can accommodate the experimental evidences of neutrino oscillations in solar and atmospheric neutrino experiments.

From (1.32) and (1.29), we may rewrite the weak interaction (1.19) as

$$\mathcal{L}_W \cong -\frac{g}{\sqrt{2}} W_\rho^- \overline{l_L} \gamma^\rho U \nu_L^{Light} - \frac{g}{\sqrt{2}} W_\rho^+ \overline{\nu_L^{Light}} \gamma^\rho U^+ l_L \tag{1.33}$$

Here,

$$U \equiv A_L^+ V \tag{1.34}$$

is the "leptonic mixing matrix" called PMNS matrix to honor the pioneering contributions of Pontecorvo, Maki, Nakagawa, Sakata [11].

Equation (1.33) expresses the charged-current weak interaction in terms of charged leptons and neutrinos of definite mass. Since the matrix Z is unitary, and X and Y are much smaller than V and W, the matrix V is to a good approximation unitary itself. From the unitarity of A_L and (1.34), this means that the leptonic mixing U is approximately unitary as well.

The matrix U has nine entries, each of which may have a real and an imaginary part, leading to a total of 18 parameters. On these parameters, unitary imposes nine constraints. First of all, each of the three columns of U must be a vector of unit length. Secondly, any two columns must be orthogonal to each other. This requirements lead to three orthogonality conditions, each of which has a real and an imaginary part, for a total of six constraints. With the nine unitary constraints taken into account, nine parameters are left which can be divided in three mixing angles and six phases. However, only three phases are physical. This can be seen by considering (1.33) with the charged-lepton and neutrino indices indicated explicitly

$$\mathcal{L}_W = -\frac{g}{\sqrt{2}}\, W_\rho^- \sum_{\alpha=e,\mu,\tau} \sum_{i=1,2,3} \overline{l_{L\alpha}}\, \gamma^\rho\, U_{\alpha i}\, \nu_{Li}^{light} + h.c. \tag{1.35}$$

Three of the six phases in U can be eliminated by re phasing the charged lepton fields e, μ, τ, whose phases are arbitrary because all other terms in the Lagrangian are invariant under such change of phases. On the other hand, the phases of the Majorana massive neutrino fields cannot be changed, because the Majorana mass term in (1.24) are not invariant under re phasing of ν_i. A common parametrization

of U in terms of mixing angles and phases is

$$U = \begin{bmatrix} 1 & 0 & 0 \\ 0 & c_{23} & s_{23} \\ 0 & -s_{23} & c_{23} \end{bmatrix} \begin{bmatrix} c_{13} & 0 & s_{13}e^{-i\delta} \\ 0 & 1 & 0 \\ -s_{13}e^{i\delta} & 0 & c_{13} \end{bmatrix} \begin{bmatrix} c_{12} & s_{12} & 0 \\ -s_{12} & c_{12} & 0 \\ 0 & 0 & 1 \end{bmatrix} \begin{bmatrix} e^{i\alpha_1/2} & 0 & 0 \\ 0 & e^{i\alpha_2/2} & 0 \\ 0 & 0 & 1 \end{bmatrix}$$

$$= \begin{bmatrix} c_{12}c_{13}e^{i\alpha_1/2} & s_{12}c_{13}e^{i\alpha_2/2} & s_{13}e^{-i\delta} \\ (s_{12}c_{23} - c_{12}s_{23}s_{13}e^{i\delta})e^{i\alpha_1/2} & (c_{12}c_{23} - s_{12}s_{23}s_{13}e^{i\delta})e^{i\alpha_2/2} & s_{23}c_{13} \\ (s_{12}s_{23} - c_{12}c_{23}s_{13}e^{i\delta})e^{i\alpha_1/2} & (-c_{12}s_{23} - s_{12}c_{23}s_{13}e^{i\delta})e^{i\alpha_2/2} & c_{23}c_{13} \end{bmatrix} \tag{1.36}$$

Here, $c_{ij} = \cos\theta_{ij}$ and $s_{ij} = \sin\theta_{ij}$, where θ_{12}, θ_{13} and θ_{23} are the three mixing angles and δ, α_1 and α_2 are the three phases. The phases α_1 and α_2 are usually called "Majorana phases", because they appear only if the massive neutrinos are Majorana particles. The phase δ is usually called "Dirac phase", because it is present also if the massive neutrinos are Dirac particles, being the analogous of the phase in the quark mixing matrix. These complex phases in the mixing matrix generate violations of the CP symmetry.

1.4 Neutrino flavor change in vacuum

Neutrino flavor change in vacuum is the process in which a neutrino is created together with a charged lepton l_α of flavor α, then travels a macroscopic distance L in vacuum, and finally interacts with a target to produce a second charged lepton l_β whose flavor β is different from that of the first charged lepton. That is, in the course of traveling from source to target, the neutrino changes from a ν_α to a ν_β. The intermediate neutrino can be any of the (light) mass eigenstates ν_i, and the amplitude for the oscillation is the coherent sum of the contributions of the various mass eigenstates. The contribution of a given ν_i is a product of three factors. First, from (1.35), the amplitude of the created ν_α to be the mass eigenstate ν_i is $U^*_{\alpha i}$. Secondly, the amplitude for this ν_i to travel a distance L if the neutrino energy is E is $\exp(-im_i^2 L/2E)$ [12]. Thirdly, the amplitude for ν_i, having arrived at the target, to produce the particular charged lepton l_β^- is, from (1.35), $U_{\beta i}$. Thus the amplitude

$Amp\,[\nu_\alpha \to \nu_\beta]$ for $\nu_\alpha \to \nu_\beta$ oscillation is given by

$$Amp\,[\nu_\alpha \to \nu_\beta] = \sum_i U^*_{\alpha i} e^{-i m_i^2 (L/2E)} U_{\beta i} \tag{1.37}$$

where the sum runs over all the light mass eigenstates. Squaring this relation and using the (at least approximate) unitary of the mixing matrix U, we find that the probability $P(\nu_\alpha \to \nu_\beta)$ for $\nu_\alpha \to \nu_\beta$ oscillation is given by [12].

$$\begin{aligned} P(\nu_\alpha \to \nu_\beta) &= |Amp\,[\nu_\alpha \to \nu_\beta]|^2 = \\ &= \delta_{\alpha\beta} - 4 \textstyle\sum_{i>j} Re(U^*_{\alpha i} U_{\beta i} U_{\alpha j} U^*_{\beta j}) \sin^2 \left[\Delta m^2_{ij} (L/4E)\right] \\ &\quad + 2 \textstyle\sum_{i>j} Im(U^*_{\alpha i} U_{\beta i} U_{\alpha j} U^*_{\beta j}) \sin \left[\Delta m^2_{ij} (L/2E)\right] \end{aligned} \tag{1.38}$$

where $\Delta m^2_{ij} \equiv m^2_i - m^2_j$. This expression for $P(\nu_\alpha \to \nu_\beta)$ is valid for an arbitrary number of neutrino mass eigenstates, and holds whether β is different from α or not. If all the neutrino masses, and consequently all the splittings Δm^2_{ij}, vanish, then $P(\nu_\alpha \to \nu_\beta) = \delta_{\alpha\beta}$. Thus the oscillation in vacuum of ν_α into a different flavor ν_β implies neutrino mass. From (1.37), is clear that this change of flavor also implies neutrino mixing: in the absence of mixing, the matrix U is diagonal so that $Amp\,[\nu_\alpha \to \nu_\beta]$ vanishes if $\beta \neq \alpha$. Finally, Eq. (1.38) shows the sinusoidal form of the oscillation probability as a function of L/E, justifying the name "oscillation".

Assuming that CPT invariance holds,

$$P(\overline{\nu_\alpha} \to \overline{\nu_\beta}) = P(\nu_\alpha \to \nu_\beta) \tag{1.39}$$

however, from (1.38), we see that

$$P(\nu_\beta \to \nu_\alpha; U) = P(\nu_\alpha \to \nu_\beta; U^*) \tag{1.40}$$

thus,

$$P(\overline{\nu_\alpha} \to \overline{\nu_\beta}; U) = P(\nu_\alpha \to \nu_\beta; U^*) \tag{1.41}$$

That is, the probability for $\overline{\nu_\alpha} \to \overline{\nu_\beta}$ is the same as for $\nu_\alpha \to \nu_\beta$, except that U is replaced by U^*. But this means that if U is not real, then $P(\overline{\nu_\alpha} \to \overline{\nu_\beta})$ differs from $P(\nu_\alpha \to \nu_\beta)$ by a reversal of the last term of (1.38). This difference is a violation

of CP invariance; CP invariance would require $\nu_\alpha \to \nu_\beta$ and $\overline{\nu_\alpha} \to \overline{\nu_\beta}$ to have equal probabilities.

It is worth noting that, up to now, experiments measured only disappearance probabilities (i.e. $\alpha = \beta$ in Eq. 1.38). Even the SNO experiment, which measures the overall flux of three active neutrinos via NC interactions, cannot distinguish different flavors. On the other hand, in the case of OPERA, it will be possible to consider the appearance probability since the appearance of all the active flavors in the beam could be experimentally observed. However, a complete 3-family scheme and a possible CP invariance violation are far away to be measured and, at present, only experimental proposals exist on this subject.

In the simplest case of two neutrino mixing between ν_α, ν_β and ν_1, ν_2, there is only one squared-mass difference $\Delta m = \Delta m^2_{21} = m^2_2 - m^2_1$ and the mixing matrix can be parameterized in terms of one mixing angle θ:

$$U = \begin{bmatrix} \cos\theta & \sin\theta \\ -\sin\theta & \cos\theta \end{bmatrix} \tag{1.42}$$

The resulting survival probability of a given flavor can be written as

$$P(\nu_\alpha \to \nu_\alpha) = 1 - \sin^2 2\theta \sin^2 \left[1.27 \frac{\Delta m^2(eV^2) L(km)}{E_\nu(GeV)}\right] \tag{1.43}$$

where we introduced the correct c and h factors inside the $\sin^2$ argument. This expression is historically very important, because data from solar and atmospheric neutrino experiments have been analyzed (in first approximation) in the two-neutrino mixing framework using Eq. (1.43).

The oscillations in this approximation are characterized by the amplitude $\sin^2 2\theta$ and by the oscillation length

$$L_{osc}(km) = \frac{2.48\ E_\nu(\mathrm{GeV})}{\Delta m^2(\mathrm{eV}^2)} \tag{1.44}$$

An experiment is characterized by the typical neutrino energy E and by the source-detector distance L. The ratio L/E establishes the Δm^2 range to which an experiment is sensitive.

1.5 Phenomenology of three neutrino mixing

The solar and atmospheric evidences of neutrino oscillations are nicely accommodated in the minimum framework of three-neutrino mixing, in which the three flavor neutrinos are linear combinations of three neutrino ν_1, ν_2 and ν_3 with masses m_1, m_2 and m_3. In the mixing matrix U (1.36), the mixing angle θ_{12} is associated with the solar neutrino oscillations, hence the masses m_1 and m_2 are separated by the smaller interval Δm^2_{solar} (we shall assume, by convention, that $m_2 > m_1$) while m_3 is separated from the 1, 2 pair by the larger interval Δm^2_{atm}, and can be either lighter or heavier than m_1 and m_2. The situation where $m_3 > m_2$ is called "normal hierarchy", while the "inverse hierarchy" has $m_3 < m_1$.

The general formula (1.38) can be simplified in several cases of practical importance. For three neutrino flavors, using the empirical fact that $\Delta m^2_{atm} >> \Delta^2_{sol}$ and considering distances comparable to the atmospheric neutrino oscillation length, only three parameters are relevant at the lowest order of approximation: the angles θ_{23}, θ_{13} and $\Delta_{atm} \equiv \Delta m^2_{atm} L/4E_\nu$. However, corrections of the first order in $\Delta_{sol} \equiv \Delta m^2_{sol} L/4E_\nu$ should be also considered and are included below (some of the terms with Δ_{sol} are further reduced by the presence of the empirically small $sin^2 2\theta_{13}$):

$$\begin{aligned} P(\nu_\mu \to \nu_\tau) \;\; &\approx \cos^4\theta_{13} \sin^2 2\theta_{23} \sin^2 \Delta_{atm} \\ &-\Delta_{sol} \cos^2\theta_{13} \sin^2 2\theta_{23} (\cos^2\theta_{12} - \sin^2\theta_{13} \sin^2\theta_{12}) \sin 2\Delta_{atm} \\ &-\Delta_{sol} \cos\delta \cos\theta_{13} \sin 2\theta_{12} \sin 2\theta_{13} \sin 2\theta_{23} \cos 2\theta_{23} \sin 2\Delta_{atm}/2 \\ &+\Delta_{sol} \sin\delta \cos\theta_{13} \sin 2\theta_{12} \sin 2\theta_{13} \sin 2\theta_{23} \sin^2 \Delta_{atm} \end{aligned} \tag{1.45}$$

$$\begin{aligned} P(\nu_\mu \to \nu_e) \;\; &\approx \sin^2 2\theta_{13} \sin^2\theta_{23} \sin^2 \Delta_{atm} \\ &-\Delta_{sol} \sin^2\theta_{23} \sin^2\theta_{12} \sin^2 2\theta_{13} \sin 2\Delta_{atm} \\ &+\Delta_{sol} \cos\delta \cos\theta_{13} \sin 2\theta_{13} \sin 2\theta_{23} \sin 2\theta_{12} \sin 2\Delta_{atm}/2 \\ &-\Delta_{sol} \sin\delta \cos\theta_{13} \sin 2\theta_{12} \sin 2\theta_{13} \sin 2\theta_{23} \sin^2 \Delta_{atm} \end{aligned} \tag{1.46}$$

where δ is the CP phase of Eq.(1.36)

$$\begin{aligned} P(\nu_\mu \to \nu_x) \quad &\approx \sin^2 2\theta_{13} \left[\sin^2 \Delta_{atm} - \Delta_{sol} \sin^2 \theta_{12} \sin 2\Delta_{atm}\right] \\ &+\Delta^2_{sol} \cos^4 \theta_{13} \sin^2 2\theta_{12} \end{aligned} \tag{1.47}$$

Note that the ν_e disappearance probability is independent of the CP phase δ.

1.6 Neutrino oscillations in matter

If neutrino pass through enough matter between their source and a target detector, then their coherent forward scattering from particles in this matter can significantly modify their oscillation pattern. This is true even if, as in the Standard Model, forward scattering of neutrinos from other particles does not by itself change neutrino flavor. The flavor change in matter that grows out by an interplay between flavor-non changing neutrino-matter interactions and neutrino mass and mixing is know as the Mikheyev-Smirnov-Wolfenstein (MSW) effect [13].

To treat a neutrino in matter, we shall make the simplifying assumption that we are dealing with an effectively "two-neutrino" problem. The neutrino is described by a column vector in flavor space,

$$\begin{bmatrix} a_e(t) \\ a_\mu(t) \end{bmatrix} \tag{1.48}$$

where $a_e(t)$ is the amplitude for the neutrino to be a ν_e at time t, and similarly for the other flavor. The time evolution of the neutrino state is then described by the Schrödinger equation in which the Hamiltonian $\mathcal{H}$ is a 2×2 matrix that acts on this column vector. If our neutrino is travelling in vacuum, the mixing is described by the vacuum mixing matrix

$$U_V = \begin{bmatrix} \cos\theta_V & \sin\theta_V \\ -\sin\theta_V & \cos\theta_V \end{bmatrix} \tag{1.49}$$

in which θ_V is the mixing angle in vacuum. $\mathcal{H}$ in vacuum is then

$$\mathcal{H}_V = \frac{\Delta m^2_V}{4E} \begin{bmatrix} -\cos 2\theta_V & \sin 2\theta_V \\ \sin 2\theta_V & cos2\theta_V \end{bmatrix} \tag{1.50}$$

Here, $\Delta m^2_V \equiv m^2_2 - m^2_1$ is the square of the mass splitting in vacuo, and E is the neutrino energy. The probability $P_V(\nu_e \to \nu_\mu)$ for $\nu_e \to \nu_\mu$ oscillation in vacuo is given by

$$P_V(\nu_e \to \nu_\mu) = \sin^2 2\theta_V \sin^2 \left(\Delta m^2_V \frac{L}{4E} \right) \tag{1.51}$$

In matter, W-exchange-induced coherent forward scattering of ν_e from ambient electrons adds an interaction energy V to the $\nu_e - \nu_e$ element of $\mathcal{H}$. V must be proportional to G_F, the Fermi constant, and to N_e, the number of electrons per unit volume. It can be shown that [14]

$$V = \sqrt{2} G_F N_e \tag{1.52}$$

Thus, the 2×2 Hamiltonian in matter is then

$$\mathcal{H} = \frac{\Delta m^2_V}{4E} \begin{bmatrix} -\cos 2\theta_V & \sin 2\theta_V \\ \sin 2\theta_V & cos2\theta_V \end{bmatrix} + \begin{bmatrix} V & 0 \\ 0 & 0 \end{bmatrix} \tag{1.53}$$

Adding to this $\mathcal{H}$ the multiple $-V/2$ of the identity, we may rewrite it as

$$\mathcal{H} = \frac{\Delta m^2_M}{4E} \begin{bmatrix} -\cos 2\theta_M & \sin 2\theta_M \\ \sin 2\theta_M & cos2\theta_M \end{bmatrix} \tag{1.54}$$

Here,

$$\Delta m^2_M = \Delta m^2_V \sqrt{\sin^2 2\theta_V + (\cos 2\theta_V - x)^2} \tag{1.55}$$

is the effective mass splitting in matter, and

$$\sin^2 2\theta_M = \frac{\sin^2 2\theta_V}{\sin^2 2\theta_V + (\cos 2\theta_V - x)^2} \tag{1.56}$$

is the effective mixing angle in matter. In this expression,

$$x \equiv \frac{V}{\Delta m^2_V / 2E} \tag{1.57}$$

is a dimensionless measure of the relative importance of the interaction with matter in the behavior of the neutrino.

If a neutrino travels through matter of constant density, then $\mathcal{H}$ (1.54) is a position-independent constant. As we can see, it is exactly the same as the vacuum

Hamiltonian (1.50), except that the vacuum mass splitting and mixing angle are replaced by their values in matter. As a result, the oscillation probability is given by the Eq. 1.51, but with the mass splitting and mixing angle replaced by their values in matter. The latter values can largely differ from their vacuum counterparts. A striking example is the case where the vacuum mixing angle θ_V is very small, but $x \cong \cos 2\theta_V$. Then, as we see from Eq. 1.56, $\sin^2 2\theta_M \cong 1$. Interaction with matter has modified a very small mixing angle with a maximal one.

Chapter 2

Experimental results on neutrino oscillations

2.1 Introduction

The last years have seen enormous progresses in the knowledge of neutrino physics. There are now strong experimental evidences of the existence of neutrino oscillations, predicted by Pontecorvo in the late 50's [1], which occur if neutrinos are massive and mixed particles.

The investigation of neutrino oscillations started in 1968 with the pioneering work of Davis (2002 Nobel laureate) and his group using a chlorine detector in the Homestake mine in USA [15]. This experiment made the first report of a deficit in the rate of neutrinos from the sun with respect to the expectation based on the theory of solar energy generation. Pontecorvo attributed the solar neutrino deficit to neutrino flavor oscillations.

Strong indication for neutrino oscillation first came from the observation of atmospheric neutrinos. The IMB [16] and Kamiokande [17] experiments in 1988 raised the problem of a possible ν anomaly and in 1998 the Soudan-2 [18], MACRO [19] and Super-Kamiokande [20] experiments provided a model-independent proof of the oscillations of atmospheric neutrinos. The values of neutrino mixing parameters that generate atmospheric neutrino oscillations have been confirmed at the end of

2002 by the first results of the K2K long-baseline accelerator experiment [21], which observed a disappearance of artificially-produced muon neutrinos due to oscillations.

In 2001 the SNO [22] and Super-Kamiokande [23] experiments provided strong indications for solar electron neutrino oscillations. In 2002 the SNO experiment measured the total flux of active neutrinos from the sun, providing a model-independent evidence of oscillations of electron neutrinos into other flavors [24]. The values of neutrino mixing parameters indicated by solar neutrino data have been confirmed at the end of 2002 by the KamLAND long-baseline reactor experiment [25], which have measured a disappearance of electron antineutrinos.

The recent discoveries and revolutionary breakthroughs in the study of neutrino properties have motivated a new generation of experimental efforts aimed at resolving the remaining issues and establishing new launching points for future explorations.

2.2 Solar neutrino experiments

The first indirect evidence for neutrino oscillations was obtained by Davis, from 1968 onwards, from the observation of a deficit in the neutrino rate from the sun detected in an experiment located in the Homestake mine in South Dakota, USA [15]. This observation, based on the fundamental understanding of the fusion processes inside the sun predicted by Bahcall et al. [26], was subsequently confirmed by several other measurements.

Solar neutrinos are produced by nuclear fusion processes in the core of the sun, which yield exclusively electron neutrinos. The expected spectral composition of solar neutrinos and its uncertainties are indicated in Fig. 2.1 as a function of neutrino energy. The low energy p-p neutrinos are the most abundant and, since they arise from reactions that are responsible for most of the energy output of the sun, the predicted flux of these neutrinos is constrained very precisely ($\pm 2\%$) by the solar luminosity. The higher energy neutrinos are more accessible experimentally, but the fluxes are known with a larger uncertainty.

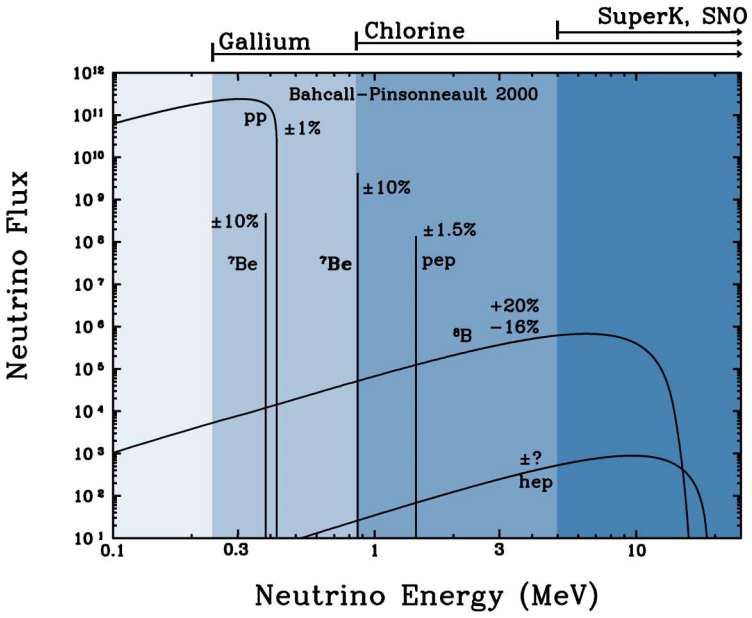

Fig. 2.1: Energy distribution of the flux of solar neutrinos predicted by the standard solar model, as computed by J. Bahcall [26]. The ranges of energies associated with the various experiments are indicated at the top of the figure.

Early measurements include radiochemical experiments sensitive to the integrated solar neutrinos with energies higher than a threshold value, see Fig. 2.1. These are the Chlorine [15] (threshold energy 0.814 MeV) and Gallium [27] (0.233 MeV) experiments. The Kamiokande [17] and SuperKamiokande [20] experiments, on the base of neutrino-electron scattering, measured both the flux and energy spectrum for $E_\nu > 7$ MeV. All these experiments reported a substantial deficit in the solar electron neutrino flux relative to the SSM. While it was realized that neutrino oscillations could be an attractive solution to this problem, it became problematic to establish this explanation with certainty due to the dependence on the SSM.

With the advent of the new millennium, a strong boost toward the solution of the solar neutrino problem came with the first SNO experimental results.

The SNO experiment combines the high performances of water Cerenkov detectors with the unique opportunity of using deuterium to detect solar neutrinos [22, 24]. Low energy neutrinos interact with deuterium in three different reactions: the charged current (CC) interaction of electron neutrinos with deuterium, the neutral current (NC) dissociation of deuterium through the interaction with active neutrino flavour and the elastic scattering of electrons. Only the CC reaction is exclusively sensitive to ν_e.

$$\begin{array}{ll} (CC) & \nu_e + d \rightarrow e^- + 2p \\ (NC) & \nu_x + d \rightarrow \nu_x + p + n \\ (ES) & \nu_x + e^- \rightarrow \nu_x + e^- \end{array} \tag{2.1}$$

The SNO collaboration has published data on the CC, NC and ES rates. The reported results (Fig. 2.2) clearly demonstrate that the total neutrino flux ($\nu_e + \nu_\mu + \nu_\tau$ as determined from NC) is in good agreement with the SSM and that the ν_e flux is suppressed (as determined from CC). This represents a strong evidence that the ν_e suppression is due to flavor-changing processes that convert the ν_e to the other flavors, as expected from ν-oscillations. Furthermore, the observed value of ν_e flux and the observed energy spectrum, when combined with the other solar-ν measurements strongly favor the so-called Large Mixing Angle (LMA) region with effective two-neutrino mixing parameters $\Delta m^2_{SUN} \sim 7 \times 10^{-5}$ eV^2 and $\tan\Theta_{SUN} \sim 0.4$.

In Fig. 2.3 a summary of the solar-ν_e data compared with the SSM with and without neutrino oscillations is shown. The shown results are: combined measurements from GALLEX and SAGE (Ga); Chlorine measurement from Homestake mine (Cl); Sudbury Neutrino Observatory (CC and NC) (SNO) and Super-Kamiokande (SK). In this plot it is possible to see the decreasing survival fraction with increasing energy in the progression $Ga \rightarrow Cl \rightarrow SNO_{CC}$ (all sensitive only to the ν_e component). The SNO$_{NC}$ measurement shows no suppression, whereas SK data exhibit the intermediate suppression due to the partial contribution of NC events to their elastic scattering signal.

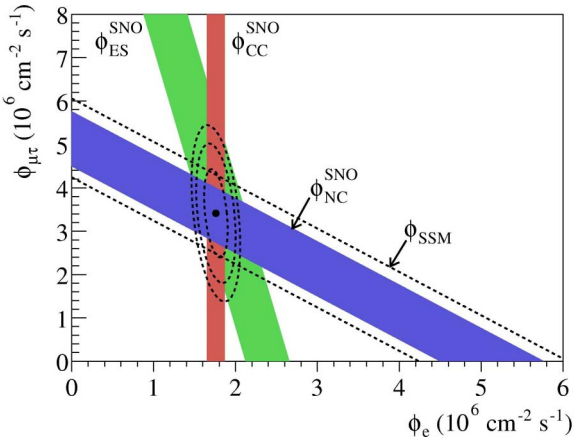

Fig. 2.2: Flux of ^{8}B solar neutrinos which are μ or τ flavor vs. flux of those of e flavor, as measured by SNO. The diagonal bands show the total ^{8}B flux as predicted by the SSM (*dashed lines*) and that measured with the NC reaction by SNO (*shaded bands*). The intercepts of the bands with the axes represent 1 σ errors. The combined fit result (error ellipses) is consistent with neutrino flavor transformation without distortion of the ^{8}B spectrum.

2.2.1 The reactor experiment KamLAND

A proof of the correctness of the LMA region has been obtained at the end of 2002 with the KamLAND long-baseline experiment, which studied disappearance of $\overline{\nu_e}$ from nuclear reactors. Even if this experiment does not study solar neutrinos, the explored region of oscillation parameters is the same as for solar neutrino experiments (pathlengths are $\sim$ 200 km and $\overline{\nu_e}$ energies are in the $\sim MeV$ region).

The KamLAND experiment, a 1000 ton liquid scintillator detector, was built at the old Kamiokande site, protected from cosmic radiation by $\sim$1000 m.w.e. overburden.

Fig. 2.4 shows the measured prompt energy distribution of the positrons for reactor neutrino events from the first 145 days of running, compared with expectations

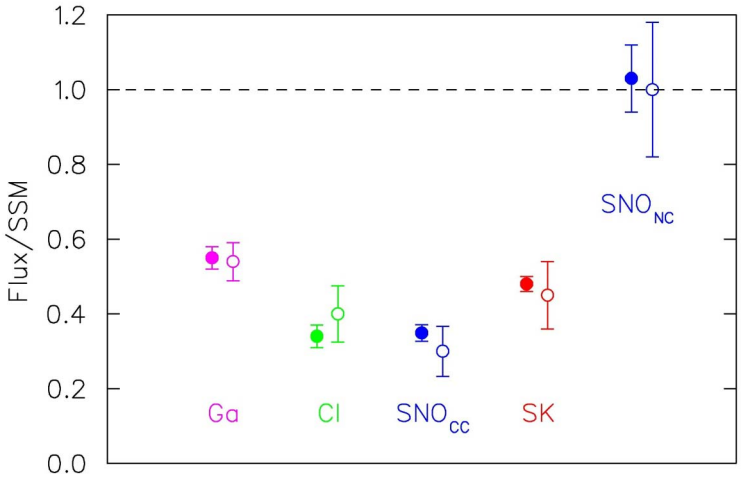

Fig. 2.3: Ratio of solar neutrino flux to SSM (without neutrino oscillations) for various experiments. Filled circles are experimental data (with experimental uncertainties only) and open circles are theoretical expectations based on SSM with best fit parameters to KamLAND and solar-ν data (uncertainties from SSM and oscillation fit combined). All charged current experiments show a substantial deficit and all are in excellent agreement with the expected values.

with and without neutrino oscillations. The absolute event rate,

$$\frac{N_{obs} - N_{bg}}{N_{expected}} = 0.611 \pm 0.085\ (stat) \pm 0.041\ (sys),$$

indicates a deficit of neutrino events consistent with $\overline{\nu_e}$ oscillations. The best fit values of the oscillation parameters allowed by KamLAND, obtained both from the rate suppression and from the analysis of the shape of the energy distribution, are in good agreement with the solar LMA solution. It is important to note that the oscillation parameters from solar experiments are the convolution of the neutrino oscillation hypothesis and matter effects. In the KamLAND case no matter effects are involved, and the comparison between solar and KamLAND results constitute the first experimental evidence of the existence of matter effects in the neutrino

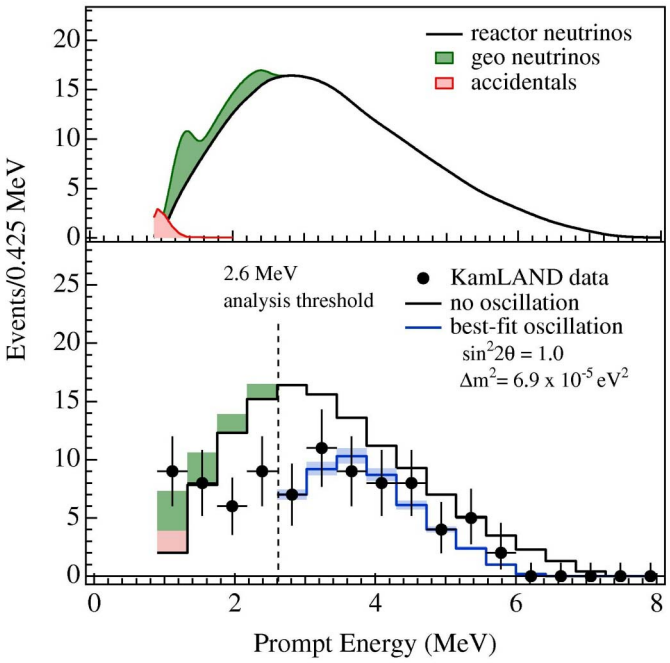

Fig. 2.4: *Upper panel*: expected energy spectrum of reactor $\overline{\nu}_e$'s along with the spectrum of geological neutrinos and the background. *Lower panel*: measured energy spectrum of the observed prompt events, compared with the expectations with and without neutrino oscillations. The *dashed vertical line* indicates the analysis cut used to remove the geological-neutrino and background-neutrino contributions.

oscillation framework (MSW effect).

The combined solution for the oscillation parameters from solar neutrino experiments and KamLAND is shown in Fig. 2.5. The combined best fit solution is $\Delta m^2 = 7.9 \times 10^{-5} eV^2$ and $\tan^2\theta = 0.38$. If the observation of the oscillation pattern will be confirmed, it will finally rule out not only the other solar neutrino oscillation solutions, but also most of the other non oscillation scenarios.

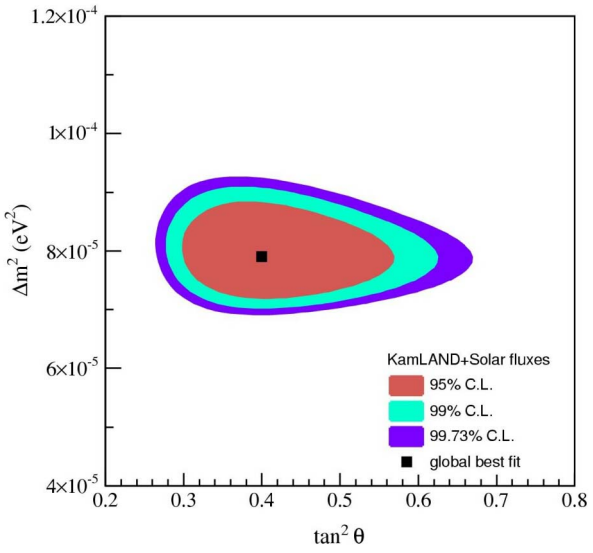

Fig. 2.5: Allowed parameter region from the combination of solar and KamLAND data.

2.3 Atmospheric neutrino experiments

Atmospheric neutrinos are generated through interactions of primary cosmic rays (mainly protons) in the upper atmosphere. The processes that yield neutrinos (π and K decays) are the same as the ones used to produce high-energy neutrino beams. The combination of an isotropic primary cosmic-ray flux with the spherical symmetry of the target (the atmosphere) ensures that the total neutrino flux must be up/down symmetric with respect to the horizon. Small deviations from this symmetry due to the earth's magnetic field are relevant only at lower energies, and corresponding measurements agree with calculations. A detector placed near the earth's surface is therefore simultaneously a medium-baseline (∼20 Km, from above) and very long-baseline (up to 13000 km, from below) experiment (Fig. 2.6).

The first indication of an anomaly in the observation of atmospheric neutrinos came from the detection of the ν_μ/ν_e flavor ratio, which is about 2 at neutrino energies $E \lesssim 1$ GeV. The Kamiokande experiment in Japan [17] and IMB experiment in the US [16] were pioneering experimental projects to develop large volume water

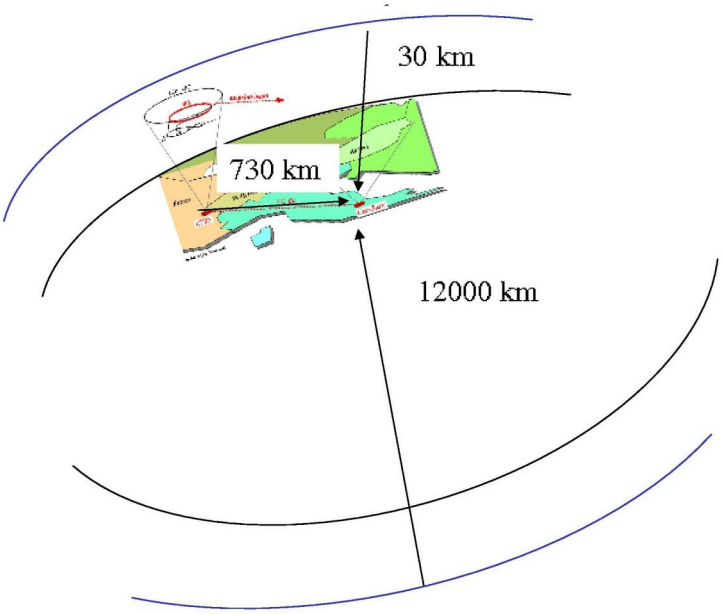

Fig. 2.6: Sketch of the earth which shows the principle of atmospheric neutrino measurements. An atmospheric neutrino detector (at the Gran Sasso laboratory in this picture) simultaneously measures neutrinos from a large range of distances. A typical long-baseline neutrino beam (the CNGS beam from CERN) pointing to the same location is also shown for comparison.

Cherenkov detectors with the primary goal of detecting nucleon decay. Both experiments (along with the Soudan experiment) reported a value significantly smaller that the predicted one. Although the measurements of ν_μ/ν_e flavor ratio suggests that the atmospheric neutrino anomaly is probably due to neutrino oscillations, they are not completely model-independent.

The breakthrough in atmospheric neutrino research occurred in 1998, during the neutrino conference in Takayama.

The Collaboration of the Soudan-2 experiment, a 1 kton fine-grained calorimeter detector, reported on the observation of a ν_μ/ν_e flavor ratio anomaly and of a distorsion of the experimental L/E_ν distribution with respect to the predicted one.

Using a detection technique completely different, based on the time of flight measurement of neutrino induced upthroughgoing muons, the MACRO Collaboration showed a clear distortion of the zenith angle distribution [19]. The observed effect is interpreted as due to the $\nu_\mu \rightarrow \nu_\tau$ oscillations, and disfavors the $\nu_\mu \rightarrow \nu_{sterile}$ hypothesis at 99% [28]. The best fit of experimental data to oscillation hypothesis gave a best fit at $\Delta m^2 = 2.3 \times 10^{-3}$ eV^2 and $\sin^2 2\theta = 1$. Fig. 2.7 shows the zenith angle distribution from the MACRO experiment, compared with the Monte Carlo simulations. The shape of the zenith angle distribution is known with a small systematic error, while the absolute normalization suffers from larger uncertainties, mainly due to the poor knowledge of the cosmic ray spectral index in the high energy region. On the other hand, from the figure it is clear how the experimental data are able to constrain, to some extent, the fluxes computed with Monte Carlo simulations. Recently, MACRO reported the L/E_ν distribution for a subsample of events for which an energy estimate was performed, using the information of MCS in the passive material of the detector Fig. 2.8 [29].

The Super-Kamiokande Collaboration presented the up-down asymmetry of high-energy events generated by atmospheric ν_μ's, providing a model independent proof of atmospheric ν_μ disappearance. Indeed, on the basis of simple geometrical arguments the fluxes of upward-going and downward-going high energy events generated by atmospheric ν_μ's should be equal if nothing happens to neutrinos on their way from the production in the atmosphere to the detector. The ν_e events displayed a normal zenith angle behavior consistent with Monte Carlo simulations. The deduced values of $\sin^2 2\theta > 0.90$ (90 % C.L.) indicate a surprisingly strong mixing scenario where the muon-type neutrino seems to be fully mixed superposition of all three mass eigenstates.

Recently the Super-Kamiokande Collaboration studied the muon neutrino disappearance probability as a function of neutrino flight length L over neutrino energy E using atmospheric neutrino events observed in Super-Kamiokande [30]. A dip

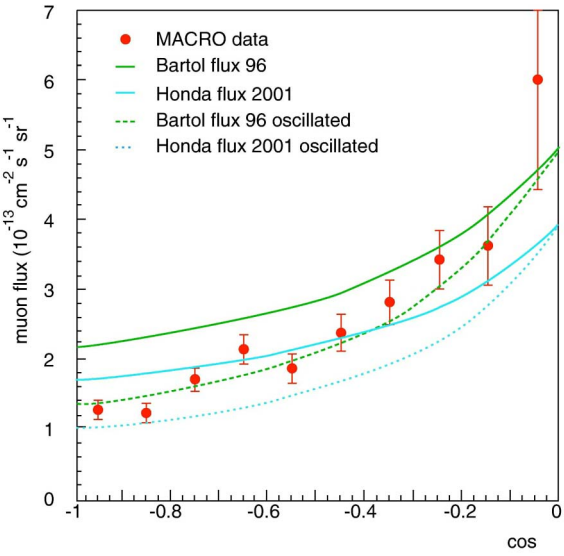

Fig. 2.7: Zenith angle distribution for the MACRO experiment, compared with two different Monte Carlo predictions, with and without assuming oscillations. .

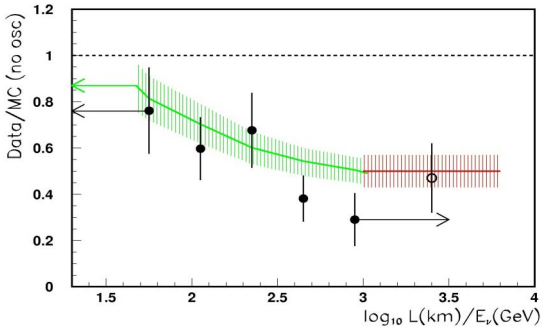

Fig. 2.8: Ratio Data/MC versus the estimated L/E_ν for the upthrougoing muon sample (black circles) and the semi-contained upgoing muons (open circle). The horizontal dashed line at Data/MC=1 is the expectation for no oscillations.

in the L/E distribution was observed in the data, as predicted from the sinusoidal flavor transition probability of neutrino oscillation. The data/prediction at large

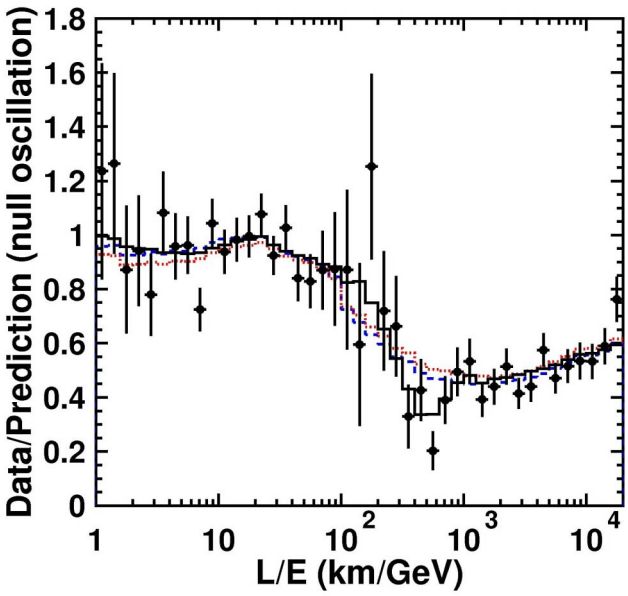

Fig. 2.9: Ratio of the data to the MC events without neutrino oscillation (points) as a function of the reconstructed L/E together with the best-fit expectation for 2-flavor $\nu_\mu \rightarrow \nu_\tau$ oscillations (solid line). The error bars are statistical only. Also shown are the best-fit expectation for neutrino decay (dashed line) and neutrino decoherence (dotted line).

L/E in Fig. 2.9 shows a slight rise from the expected flat distribution. Alternative models that could explain the zenith angle and energy dependent deficit of the atmospheric muon neutrinos are disfavored, since they do not predict any dip in the L/E distribution. This is a very important result because the observed L/E distribution is the first direct evidence that the neutrino survival probability obeys the sinusoidal function as predicted by neutrino flavor oscillations. This analysis constrained $\nu_\mu \rightarrow \nu_\tau$ neutrino oscillation parameters with $1.9\times10^{-3} < \Delta m^2 < 3.0\times10^{-3}$ eV^2 and $\sin^2 2\theta > 0.90$ at 90% confidence level.

In Fig. 2.10 the 90% C.L. allowed region in the oscillation parameter space (Δm^2, $\sin^2 2\theta$) from the atmospheric neutrino experiments Soudan-2, MACRO and Super-Kamiokande.

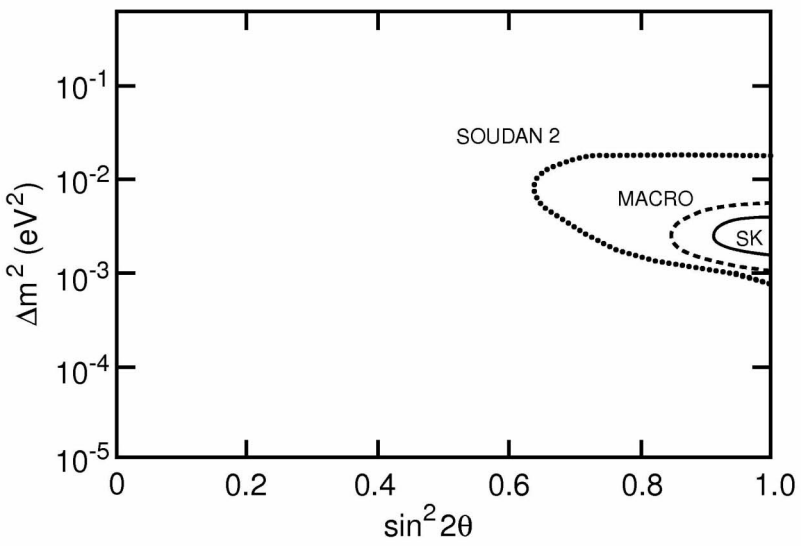

Fig. 2.10: 90% C.L. allowed region in the oscillation parameter space (Δm^2, $\sin^2 2\theta$) from the atmospheric neutrino experiment Soudan-2, MACRO and Super-Kamiokande.

2.4 Long-Baseline Experiments

The phenomenon of neutrino oscillations observed in the atmospheric neutrino experiments requires further study to precisely determine the mixing parameters Δm^2_{23} and θ_{23}. There are two long baseline accelerator experiments with prospect for results in the near term: K2K in Japan and MINOS in USA.

The KEK to Kamioka long-baseline neutrino oscillation experiment is the first accelerator based project to explore neutrino oscillation in the same Δm^2 region as atmospheric neutrinos. The K2K experiment uses an accelerator-produced ν_μ beam with a mean energy of 1.3 GeV directed to the Super-Kamiokande detector 250 km away. A near detector is located at a distance of 300 m from the target. The main goal is the observation of a charged-current event deficit in the far detector with respect to the near detector to confirm the atmospheric neutrino anomaly and further constrain the parameters space for neutrino oscillations.

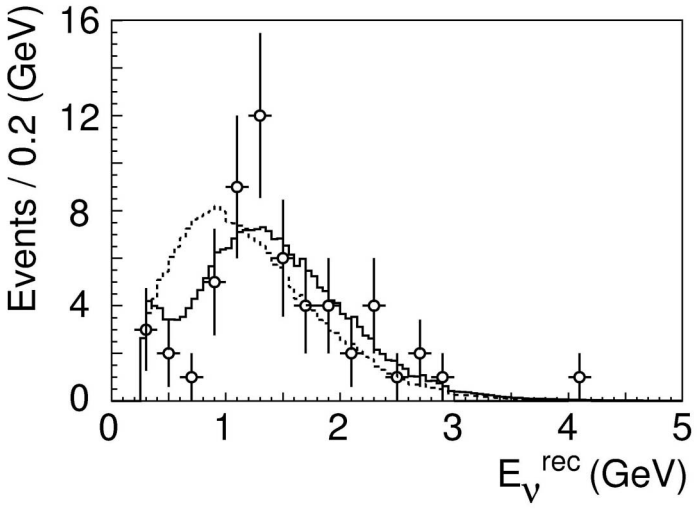

Fig. 2.11: K2K. Distortion of the neutrino energy spectrum observed at Super-Kamiokande (data points), with the best fit spectrum (solid line). The dashed line is the expected spectrum without oscillations.

In 2004 K2K published the evidence for the energy-dependent disappearance of ν_μ, which are presumed to have oscillated to ν_τ [31]. They observe a distortion of the neutrino energy spectrum and a deficit in the total number of events. The observed spectrum reveals the type of distortion expected from oscillations, the best fit E_ν distribution is shown with the data in Fig. 2.11. The observed number of events and energy spectrum of neutrinos at SK are consistent with neutrino oscillation and the allowed regions of the oscillation parameters from the K2K experiment are consistent with the atmospheric measurements.

The NUMI/MINOS experiment uses the Main Injector proton beam at Fermilab to produce a ν_μ beam in the energy range 3 GeV $< E_\nu <$ 18 GeV directed at a large detector located in the Soudan mine at a distance of 730 km [32]. The lowest energy neutrino beam will be optimal for studying the region of $\Delta m^2 \sim 2.0 \times 10^{-3}$ eV^2. The basic measurements are similar to those performed at K2K, but the much

better statistics offer increased sensitivity, including significant measurements of the NC/CC ratio and of potential electron neutrino appearance. The first physics run with a low-energy beam is scheduled for 2005.

The two projects are complementary in the sense that the K2K experiment has started to confirm the atmospheric neutrino results quantitatively, and the NUMI/MINOS project will yield a more precise measurements of the oscillation parameters and strong indications of the oscillation mode. The European long-baseline project CNGS from CERN to Gran Sasso Laboratory, fully described in the next chapter, will definitely settle the question of whether the primary oscillation mode involves the τ neutrino.

A fourth program at the Japan Hadron Facility (JHF), sending a very high intensity neutrino to Super-Kamiokande from a distance of 290 km is currently being proposed. On an ever longer term, a beam from a so-called neutrino factory [33] (neutrino from a high-energy muon storage ring) could open up the possibility of the measurements of CP violation in the leptonic sector.

2.5 Other reactor experiments

CHOOZ was a long-baseline reactor ν_e disappearance experiment [34] which did not observe any disappearance of electron anti-neutrinos at a distance of about 1 km from the source. In spite of such negative result, the Chooz experiment is important because it shows that the oscillation of electron neutrinos at the atmospheric scale of Δm^2 are small or zero.

The Chooz detector consisted in 5 tons of liquid scintillator in which anti-neutrinos were revealed through the inverse β-decay reaction:

$$\overline{\nu_e} + p \rightarrow n + e^+ \tag{2.2}$$

with a threshold $E_{th} = 1.8$ MeV. The neutrino energy is measured through the positron energy: $E = E_{e^+} - 1.8$ MeV.

The ratio of observed and expected number of events in the CHOOZ experiment

is

$$\frac{N^{Chooz}_{observed}}{N^{Chooz}_{expected}} = 1.01 \pm 0.04 \tag{2.3}$$

showing no indication on any electron antineutrino disappearance. The absence of a strong $\overline{\nu}_e \rightarrow \overline{\nu}_\mu$ oscillation effect further constrains the parameter space allowed for atmospheric $\nu_\mu \rightarrow \nu_e$ oscillation.

The results of the Chooz experiment have been confirmed, with lower accuracy, by the Palo Verde experiment [34].

2.6 Direct mass measurements of neutrino masses

Conceptually the simplest way to explore the neutrino mass is to determine its effects on the momenta and energies of charged particles emitted in weak decays. Over the past decades there has been progress in probing neutrino mass through direct measurements of decay kinematic.

Techniques for measuring the mass of the electron neutrino involve the search for a distortion in the shape of the β-spectrum in the endpoint region. Tritium β-decay is commonly used for this measurements because of its low endpoint energy and simple nuclear and atomic structure. The current best limits of $m_{\nu_e} \leq 2.2$ eV^2 at 90% C.L. come from the Mainz and Troitsk neutrino mass experiments [35]. A new experiment, KATRIN, with an expected sensitivity of 0.2 eV at 90% C.L. is currently under installation in Germany [36].

Direct limit on both the muon and tau neutrino masses are based on kinematic measurements using semileptonic, weak particle decays. The observables in these measurements are either invariant mass or the decay particle momentum. As these measurements rely on knowing the particle mass and momentum the sensitivity of these neutrino mass measurements is limited. The direct experimental limits on neutrino mass as reported by the Particle Data Group [37] are summarized in the Tab. 2.1.

Direct kinematic methods have not yet measured a non-zero neutrino mass. At

Neutrino Mass	Mass Limit	Decay Mode	Experiment
m_{ν_e}	< 2.2 eV	$^3H \rightarrow^3 He + e^- + \nu_e$	Mainz [35]
m_{ν_μ}	< 190 keV	$\pi^+ \rightarrow \mu^+ + \nu_\mu$	PSI [38]
m_{ν_τ}	< 18.2 MeV	$\tau^- \rightarrow 2\pi^-\pi + \nu_\tau$	ALEPH [39]
		$\tau^- \rightarrow 3\pi^-2\pi + \nu_\tau$	

Tab. 2.1: Direct experimental limits on neutrino mass measurements.

present there is no direct indication from these experiments for new physics beyond the Standard Model and other searches for the signature of massive neutrinos are needed.

2.7 Neutrinoless double-β decay

Another unique signature of massive neutrinos is neutrinoless double-β decay, a lepton-number-violating process also know as $0\nu\beta\beta$. The process $(A, Z) \rightarrow (A, Z + 2) + 2e^-$ can be mediated by an exchange of a light Majorana particle. The existence of $0\nu\beta\beta$ requires the existence of Majorana neutrino mass, and the Neutrinoless double-beta decay is the only experimental approach known that distinguishes between Majorana and Dirac masses.

The observable $0\nu\beta\beta$-decay rate is proportional to the effective Majorana mass squared $|m_{\beta\beta}|^2$ with

$$m_{\beta\beta} = \left| \sum_i m_{\nu_i} U_{ei}^2 \right| \tag{2.4}$$

The best current limits on $m_{\beta\beta}$ come from Heidelberg-Moskow experiment which uses 11 kg of enriched ^{76}Ge with an isotopic abundance of 86% with an upper limit on the effective neutrino mass [40]:

$$m_{\beta\beta} \leq 0.35\,\text{eV (90\% C.L.)}$$

A recent analysis of data from this experiment by Klapdor-Kleingrothaus et al. lead to the announcement of the discovery of neutrinoless double-beta decay

corresponding to a mass of 0.4 eV with a 4.2 σ significance [41]. These claims have not yet been confirmed.

A few double-β decay experiments which should reach a sensitivity of $m_{\beta\beta}$ of 0.1 eV or below are under way or have been proposed. Common to all experiments is their relatively large scale, with about 1 ton total mass of material of high isotopic abundance, and their very stringent demands on background suppression. These experiments are exploring all possible ways to lower the background, which is limited by the neutrinoless double-β decay mode and therefore requires a good energy resolution.

2.8 Cosmological constraints

In the early universe, when the temperature was $T > 1$ MeV, the high density of particles allowed weak interactions to occur prolifically leading to a substantial density of neutrinos. As the universe cooled to $T < 1$ MeV, these reactions became much slower than the expansion rate and the neutrinos decoupled from the remaining ionized plasma and radiation (photons). Much later ($\sim$ 100000 years), the universe cooled enough that atoms formed and the radiation decoupled from the matter. The cosmic microwave background (CMB) is the further cooled (through expansion) relic of this period, and contains information on the distribution of matter at that time in the history of the universe.

The presently observed distribution of matter (through high resolution galaxy surveys) and distribution of radiation (CMB) would both be affected by the presence of massive neutrinos in the early universe. Although the power spectra of the CMB and the density fluctuations are both sensitive to massive neutrinos, a combined analysis of both observables is especially effective in addressing the existence of massive neutrinos. Thus comparison of the power spectrum of CMB with the observed distribution of galaxies can provide information on the sum (over all flavors) of light neutrino masses. An analysis of the recent WMAP data [42] yields the result $\sum_f m_{\nu_f} < 0.7$ eV (95% C.L.).

2.9 Conclusions

The recent years have been extraordinarily fruitful for neutrino physics, yielding model-independent proofs of solar and atmospheric neutrino oscillations, which have been confirmed, respectively, by the long baseline reactor experiment KamLAND and the accelerator experiment K2K. Taking into account the negative result of the CHOOZ and Palo Verde long-baseline reactor experiments, all data from solar, KamLAND, atmospheric and K2K data have provided important information on neutrino mixing parameters in the framework of three neutrino mixing.

Even if the values of some parameters of three-neutrino mixing are determined with a precision that was unthinkable a few years ago, still several fundamental characteristics of neutrino remain unknown. Among them the most important are: the Dirac or Majorana nature of neutrinos, the absolute scale of neutrino masses, the existence of CP violation in the lepton sector, the number of light neutrinos and the electromagnetic properties of neutrino. Several existing experiment and future projects are aimed at the exploration of these characteristics, which are very important for the understanding of neutrino physics.

However, even if most of the experimental data combine together to produce a substantially organic and coherent scenario, a final and definite proof of the atmospheric ν oscillations is still missing. OPERA will attempt to address and resolve this point in few years of data taking.

Chapter 3

The OPERA Experiment

3.1 Introduction

The OPERA experiment [43] is a long baseline experiment designed to be the conclusive test of the $\nu_\mu \rightarrow \nu_\tau$ oscillation hypothesis by means of the direct observation of ν_τ in an initially pure ν_μ beam.

The OPERA apparatus, under construction at the Gran Sasso underground laboratory, will detect neutrinos coming from the CERN SPS (the CNGS, CERN Neutrino beam to Gran Sasso), 732 km downstream. The beam energy has been tuned to be well above the τ lepton production threshold, and in the oscillation parameter region indicated by the atmospheric neutrino experiments. In case of a positive signal, the observation of even a few ν_τ events will be significant, because of the very low expected background.

Thanks to the excellent electron identification capability, exploited for the reconstruction of the $\tau \rightarrow e$ decay, and to the small ν_e contamination in the CNGS beam, OPERA is also able to perform a $\nu_\mu \rightarrow \nu_e$ oscillation search.

OPERA is designed starting from the Emulsion Cloud Chamber (ECC) detector, a modular structure made of a sandwich of passive material plates with emulsion layers. By assembling a large quantity of such modules, it is possible to realise a $\sim$ 2000 ton fine-grained vertex detector optimised for the study of ν_τ appearance.

The target is complemented with magnetized iron spectrometers for muon charge and momentum measurements, and electronic detectors for event location inside the emulsion target (Target Tracker). Moreover, a veto detector system is required to flag events from neutrino interactions in the rocks surrounding the detector.

The basic element of the ECC is the *cell*, which is made of a 1 mm thick lead plate followed by a thin emulsion film. The ECC *brick* is obtained by piling-up 56 cells in a sandwich-like structure. Bricks are assembled to form *walls*; a wall and its related electronic tracker plane constitute a *module*. A sequence of modules with a downstream spectrometer constitutes a *supermodule*. The final detector consists of two supermodules, with a total target mass of $\sim$1.8 kt.

The detector installation started in 2003 and the first neutrino beam delivery is foreseen for May 2006.

3.2 The CNGS neutrino beam

The CNGS is a ν_μ beam produced with 400 GeV protons extracted from the SPS complex at CERN. A schematic overview of the CNGS neutrino beam is shown in Fig. 3.1.

SPS protons hit a graphite target made of a series of rods, for an overall target length of 2 m, producing secondary pions and kaons. The target rod diameter is 4 mm so that the proton beam is well contained within the target. The first coaxial lens, the horn, is placed 1.7 m downstream of the proton beam. The second one, the reflector, is located 43.4 m downstream of the focus.

Helium tubes are placed in the free spaces before and after the reflector in order to reduce the interaction probability for secondary hadrons, Fig 3.1.

Pion and kaons focused by the optics are then directed toward the decay tunnel where they decay producing the neutrino beam. Since the decay length of pions with energy of 40 GeV/c is 2.2 km, a long decay tunnel is envisaged. Given the angular distribution of the parent mesons, the longer the decay tunnel the larger must be its diameter. A tunnel of 2.45 m diameter and 1000 m length has been

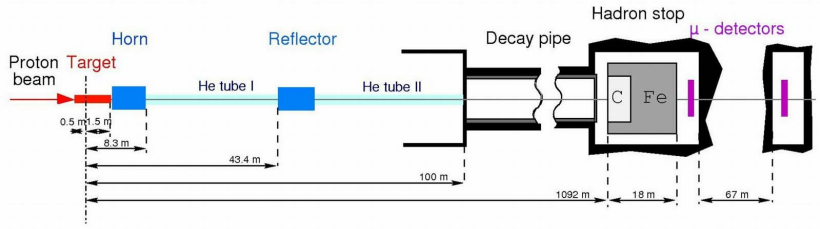

Fig. 3.1: Layout of the CNGS neutrino beam. The coordinate origin is the focus of the proton beam.

chosen for the CNGS. A massive iron hadron stopper is situated at the exit of the decay tunnel.

The signals induced by muons (from π, k meson decays) in two arrays of silicon detectors placed in the hadron stopper is used for the on line monitoring and the tuning of the beam (steering of the proton beam on target, horn and reflector alignment, etc.). The separation of the two arrays, 67 m of passive material equivalent to 25 m of iron, allows a rough measurement of the muon energy spectrum and of the beam angular distribution. When the neutrino beam reaches Gran Sasso, 732 km from CERN, its diameter is calculated to be of the order of two kilometres.

The intensity of the SPS proton beam is one of the main features needed to achieve the physics goal of the OPERA experiment. In a mode of operation where the SPS is shared with LHC, 4.5×10^{19} protons on target (pot) can be delivered in one year with a 200 days run. The CNGS beam features are summarized in Tab. 3.1 and 3.2.

The possibility of an increase of the neutrino beam intensity at moderate cost is being studied by the CNGS design group [45] and other groups working on the PS and SPS machines [46]. The SPS and its injectors have a crucial role for the LHC accelerator and considerable efforts and investment are going into the upgrade of these accelerators to meet the requirements of LHC. Most of the efforts are also directly beneficial to CNGS: for example, it is expected that the maximum intensity

ν_μ (m^2/pot)	7.78×10^{-9}
ν_μ CC events/pot/kton	5.85×10^{-17}
ν_e/ν_μ	0.6%
$\overline{\nu_\mu}/\nu_\mu$	2.1%
$\overline{\nu_e}/\nu_\mu$	0.2%

Tab. 3.1: Nominal performances of the CNGS reference beam.

Δm^2	ν_τ CC interactions/kton/year
$1 \times 10^{-3} eV^2$	2.5
$2.5 \times 10^{-3} eV^2$	15
$3 \times 10^{-3} eV^2$	22.5
$5 \times 10^{-3} eV^2$	60.5

Tab. 3.2: Number of ν_τ charged-current interactions at Gran Sasso per kton and per year (shared mode) for different values of Δm^2 (for $\sin^2(2\theta) = 1$). These event numbers do not take detector efficiencies into account.

in the SPS will be 7×10^{13} rather than 4.5×10^{13} pot/cycle. Moreover it has recently pointed out that an increase in the proton beam intensity can be reached by reducing the beam losses between two sequential pre-accelerators. These improvements could, at a moderate cost, increase the proton flux by as much as a factor 1.5.

The CNGS energy spectrum has been optimized for ν_τ appearance and the prompt ν_τ contamination is negligible. The expected ν_e contamination is relatively small compared to the dominant ν_μ component (Tab. 3.1) and allows to search for the sub-dominant oscillation $\nu_\mu \rightarrow \nu_e$ seeking an excess of ν_e charged-current (CC) events.

3.3 Detector structure and working principle

The OPERA detector is located in the Hall C of the Gran Sasso underground laboratory. It consists of two identical parts called *Supermodules* (SM), each of them contains a target part and a muon spectrometer.

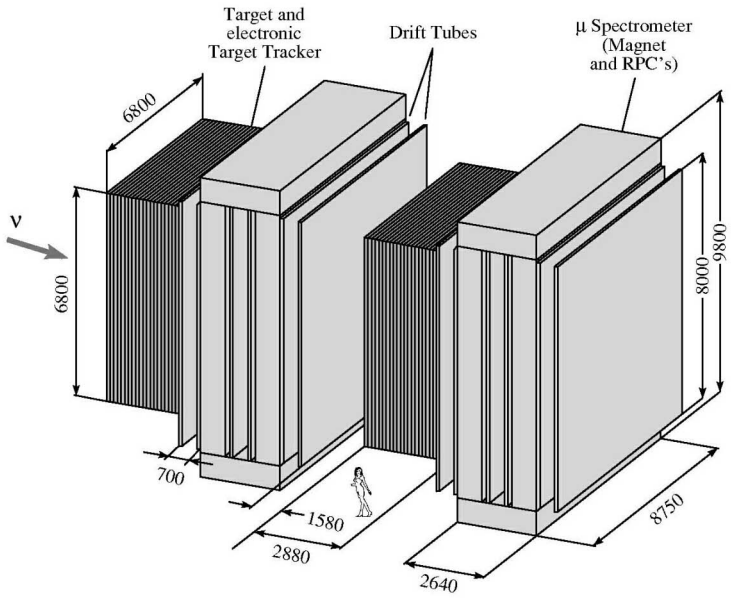

Fig. 3.2: Schematic view of the OPERA detector.

The target part is composed of 31 walls (62 in total) and each wall contains a layer called *brick wall* and a layer called *Target Tracker (TT) wall*. The brick wall contains 3328 bricks for a total of 206336 bricks in the whole apparatus. The brick support structure is designed to insert or extract bricks from the sides of the walls, by using an automated manipulator. The TT wall consist of horizontal and vertical scintillator strips read out by WLS fibres couples to a single 64 channel multi-anode photomultiplier tubes.

The main part of the muon spectrometer is a dipolar magnet, providing a field B $\sim$1.6 Tesla transverse to the neutrino beam axis. Between the magnet iron slabs are inserted 22 layers of resistive plate chambers (RPC), while three layers of Drift Tubes are placed in front, in the middle and behind the magnet. The front part of the

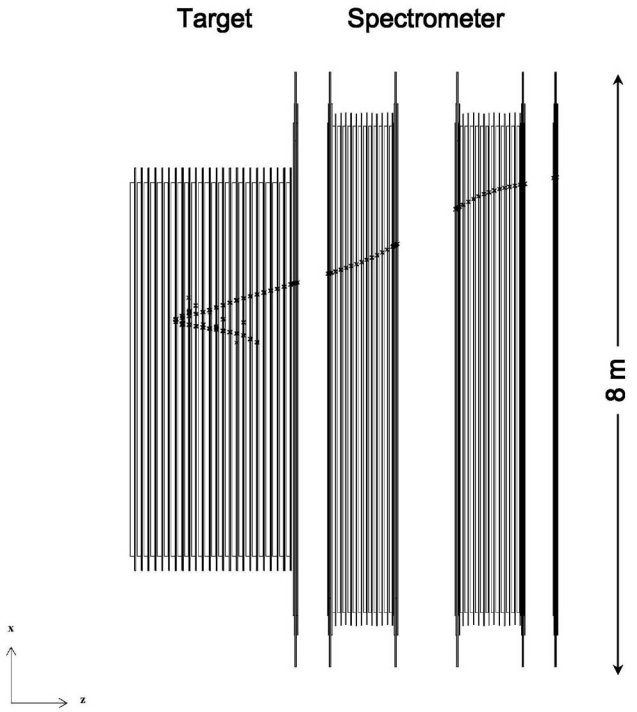

Fig. 3.3: Schematic view of one module with a simulated ν_μ CC event. The muon is identified by the Target Trackers and by the muon spectrometer Inner and Precision Trackers.

detector and the outer region of the spectrometer will also be equipped with RPCs to be used as veto to essentially reject muons produced by neutrino interactions in the rock surrounding the LNGS experimental hall. A schematic view of the OPERA detector is shown in Fig. 3.2 and a x-z view of one Supermodule is shown in Fig. 3.3.

The basic emulsion detector unit, called ECC brick, is obtained by stacking 56 lead plates and 57 emulsion films. The film is made up of two emulsion layers 45 μm thick on either side of a 210 μm plastic base. An additional emulsion sheet, called Changeable Sheet(CS), is independently packed and placed downstream of each brick. The CS can be detached from the rest of the brick for analysis. It will

be used to first locate the tracks produced in neutrino interactions which have to be followed in the rest of the brick.

Once a neutrino interacts in the target section, the TT planes will indicate the brick where the interaction has happened. The candidate brick is removed by the brick manipulator system and the corresponding CS is detached and developed. The film is then scanned by automatic microscopes to search for tracks originating from the neutrino interaction. If none is found, the rest of the brick is left untouched for reuse and a suitable nearby brick is removed. When a confirmation of neutrino events is observed in the CS, the brick is exposed to cosmic rays to collect muon alignment tracks before development. After development, the emulsions are sent to automatic scanning microscopes in order to find the neutrino vertex and the decay kink in the vertex region.

3.3.1 Emulsion target

Fig. 3.4 shows a sketch of an ECC cell: a 1 mm lead plate followed by a pair of emulsion layers placed on both sides of a plastic base. A charged particle produces a track segment in each emulsion layer. The sensitivity of the OPERA emulsions is about 30-35 grains/100 μm and it is adequate for the reconstruction of track segments by means of automatic scanning devices.

Each brick has transverse dimensions of 10.2 $\times$ 12.9 cm^2 It consists of 56 cells with a total thickness of about 7.6 cm (10 X_0) and has a weight of 8.3 kg.

The dimensions of the bricks are determined by conflicting requirements: the mass of the bricks selected and removed for analysis should represent a small fraction of the total target mass; on the other hand, the brick transverse dimensions should be substantially larger than the uncertainties in the interaction vertex position predicted by the electronic trackers.

The brick thickness in units of radiation lengths is large enough to allow electron identification through their electromagnetic showering and momentum measurement by multiple coulomb scattering following tracks in consecutive cells. An efficient

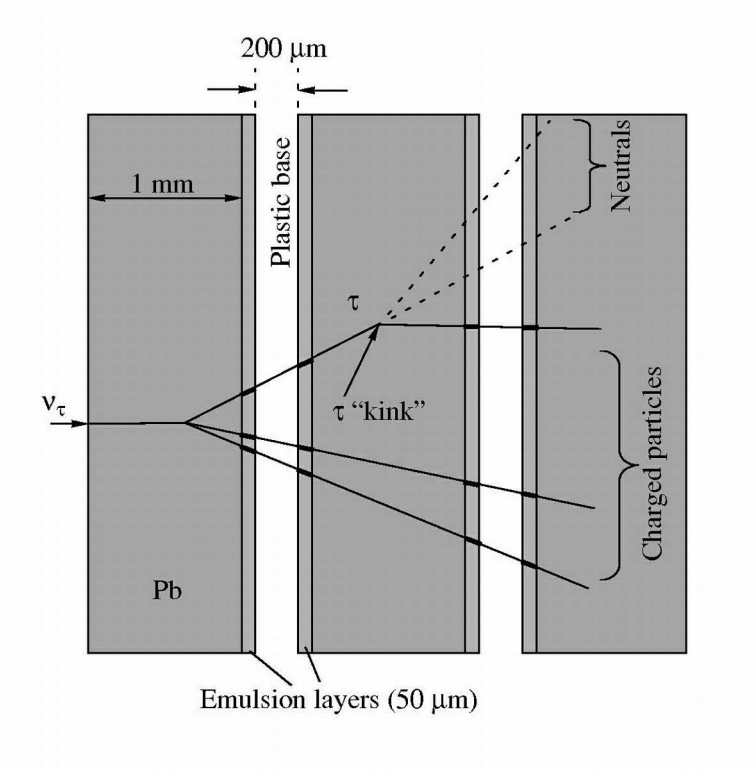

Fig. 3.4: Schematic structure of an ECC cell in the OPERA experiment. The τ decay kink is reconstructed in space by using four track segments in the emulsion films.

electron identification requires about $3 \div 4$ X_0 and the multiple scattering requires ~ 5 X_0. With a 10 X_0 brick thickness, for half of the events such measurements can be done within the same brick where the interaction took place, without the need to follow tracks into downstream bricks.

3.3.2 Target Tracker

Electronic detectors placed downstream of each brick wall are used to select the brick where the neutrino interaction took place and to indicate the region of the films to be scanned at the microscope. The changeable sheet is used to confirm the brick choice so a moderate spatial resolution can be tolerated, which allows to reduce the cost of the electronic trackers covering a large surface.

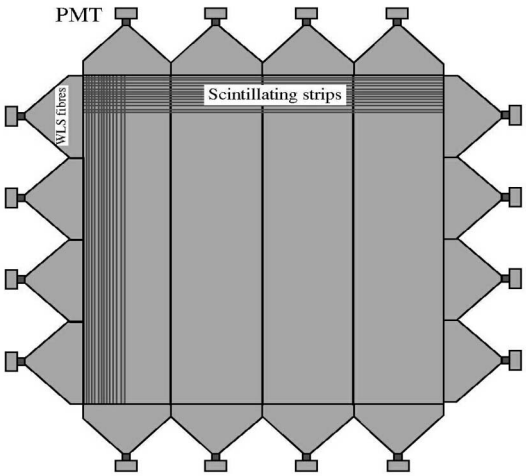

Fig. 3.5: Schematic view of the target tracker wall.

For this purpose, plastic scintillator strips read out by Wave Length Shifting (WLS) fibres have been chosen. They will be also used to sample the energy of hadronic showers and to contribute to the identification and reconstruction of penetrating tracks.

Each brick wall is followed by two electronic tracker planes (with strips oriented along the X and Y axis, respectively). The planes are squares of ∼6.7 m edge-to-edge and contain 256 scintillator strips. Each group of 64 strips constitutes an independent unit, read out on each side by a 64-pixel photo-detector, such that 8 photo-detectors are required for each tracker plane. No multiplexing scheme is foreseen. Fig. 3.5 shows a schematic view of a target tracker wall.

Scintillator strips are 2.6 cm wide and 1 cm thick. Simulations have shown that a transverse segmentation below this value does not significantly improve the physics performance, in particular the brick finding efficiency. Their energy resolution is what is expected from a calorimetric sampling ($\Delta E/E \sim 0.65/\sqrt{E(GeV)} + 0.16$). During the run, muons generated in the interaction of CNGS neutrinos in the cavern rock ("rock muons"), cosmics ray muons, radioactive sources and light injection

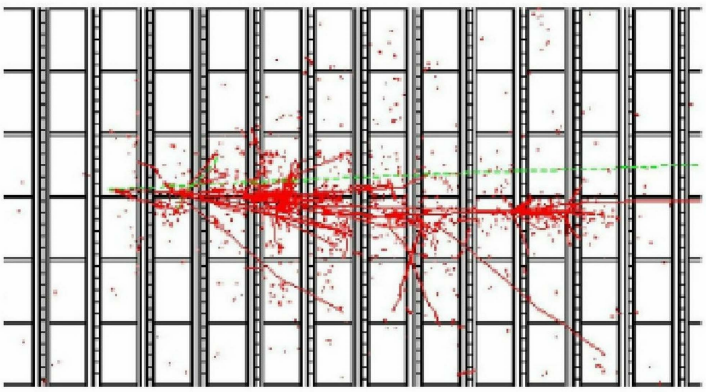

Fig. 3.6: Display of a simulated $\tau \rightarrow \mu$ event in the OPERA target. The beam comes from the left of the figure. The primary vertex occurs in the third brick wall. Each wall of bricks is followed by a TT plane. These planes are oriented along the X and Y directions, perpendicular to the beam. The muon track corresponds to the longest track escaping on the right of the figure.

systems will be used to calibrate the system.

The selection of the brick containing the neutrino interaction vertex is performed by combining different algorithms based on the observed transverse and longitudinal event profiles as well as on the presence of individual reconstructed tracks. As an illustration, Fig. 3.6 shows the longitudinal profile of a simulated ν_τ event with a muonic decay in a projected view.

3.3.3 Muon spectrometers

The main goals of the spectrometers are the muon momentum and charge measurements. The magnets contribute to the kinematics reconstruction of the event performed by the ECC and the scintillators and suppress the background coming from charm production through the identification of secondary antimuons.

The OPERA spectrometers consist of active detectors (RPC, XPC and Drift Tubes) and a dipolar magnet made of two iron walls interleaved by pairs of high resolution trackers. Each wall is made of 12 iron plates 5 cm thick. The iron is

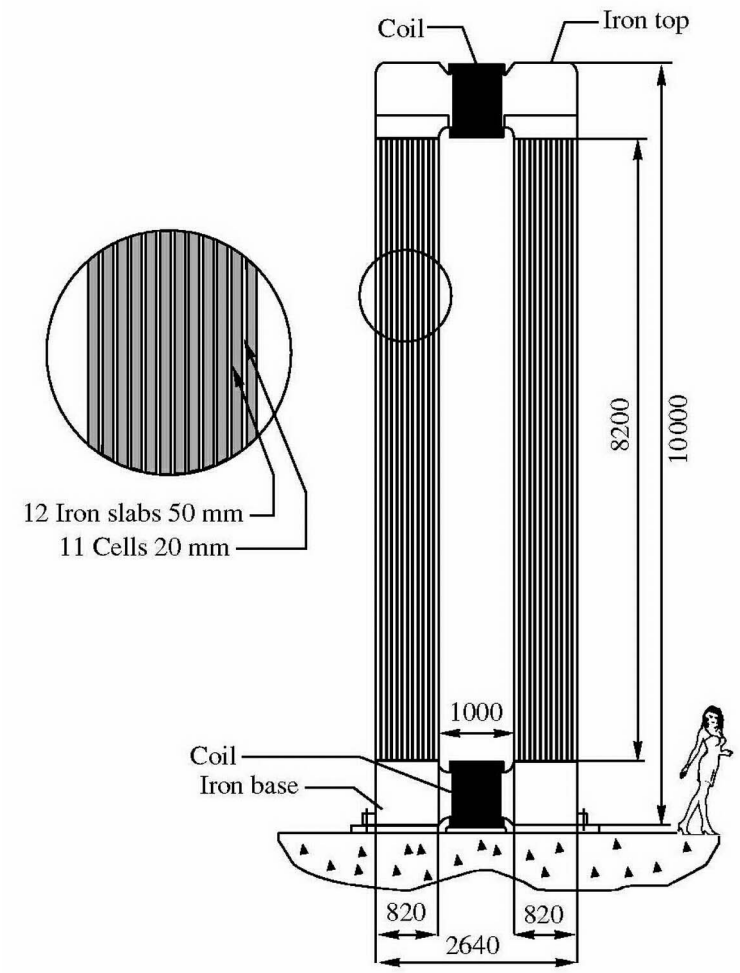

Fig. 3.7: Schematic view of the OPERA dipolar magnet.

magnetized by a current of about 1600 A circulating in the top and bottom copper coils. The magnetic flux density in the tracking region is 1.55 T with vertical field lines of opposite directions in the two magnet walls. The transverse useful dimensions of the magnet are 8.75 m (horizontal) and 8 m (vertical) providing adequate geometrical acceptance also for muons originating in the upstream target volume. Fig. 3.7 presents a lateral view of the OPERA magnet.

The high resolution trackers, denoted as Precision Trackers, consist of vertical drift tube planes with an intrinsic resolution of 0.3 mm in the bending direction.

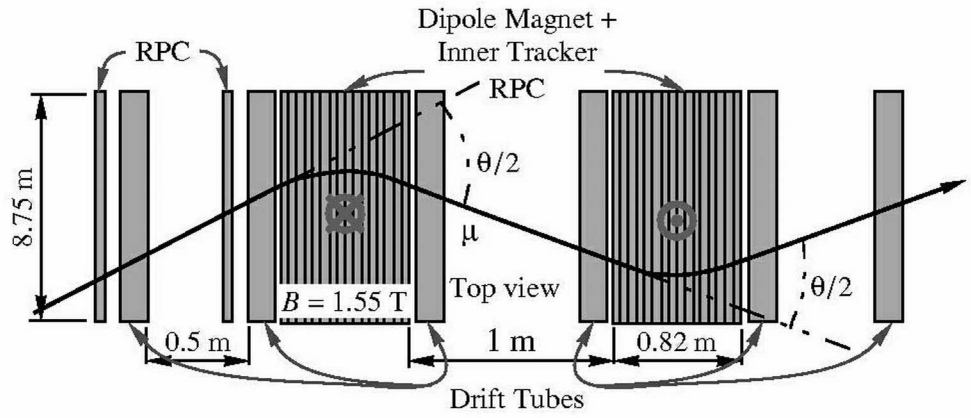

Fig. 3.8: Top view of one OPERA spectrometer.

Allowing for some misalignment, an overall resolution on each measured coordinate of 0.5 mm has been assumed. The two tracker planes housed between the two magnet walls provide an angular measurement of the muon track with a 100 cm lever arm. The lever arm for the external trackers is larger than 50 cm. This design leads to a momentum resolution of better than 30% in the relevant kinematical region.

The so-called Inner Trackers are inserted between the magnet iron plates. They are made of RPC detectors. On each face of the chambers, the induced pulses are collected by 3 cm wide pickup copper strips in the horizontal and vertical directions. The Inner Trackers allow a coarse tracking inside the magnet to identify muons and to ease up track matching between the Precision Trackers. They also provide a measurement of the tail of the hadronic energy leaking from the target and of the range of muons which stop in the iron. Fig. 3.8 illustrates the spectrometer tracking strategy.

3.4 Physics performances: $\nu_\mu \rightarrow \nu_\tau$ search

3.4.1 Signal detection efficiency

The signal of the occurrence of $\nu_\mu \rightarrow \nu_\tau$ oscillations is the charged current interaction of ν_τ's in the detector target ($\nu_\tau N \rightarrow \tau^- X$). The reaction is identified by the detection of the τ lepton. The τ decay channels investigated by OPERA are the electron, muon and hadron channels:

$$\begin{array}{lcl} \tau^- & \rightarrow & e^- \nu_\tau \overline{\nu}_e \\ \tau^- & \rightarrow & \mu^- \nu_\tau \overline{\nu}_\mu \\ \tau^- & \rightarrow & (h^- h^+) h^- \nu_\tau (n\pi^0) \end{array}$$

Measurements of the branching ratio (BR) of the three single-prong decay modes give 17.8%, 17.7% and 49.5% for the electronic, muonic and hadronic channel, respectively. For the typical τ energies expected with the CNGS beam one obtains the decay length distribution shown in Fig. 3.9, with an average decay length of ~ 450 μm.

The τ decays inside the ECCs are classified in two categories: *long* and *short* decays. Short decays correspond to the case where the τ decays in the same lead plate where the neutrino interaction occurred. The τ candidates are selected on the basis of the impact parameter (IP) of the τ daughter track with respect to the interaction vertex (IP $>$ 5-20 μm). This is applied only for the electron and muon channels, since in the hadronic channel the background coming from hadron re-interactions dominates. In the long τ decays, the decay occurs in the first or second downstream lead plate. τ candidates are selected on the basis of the detection of a reasonably large kink angle between the τ and the daughter track ($\theta_{kink} > 20$ mrad). The distribution of the τ decay kink for the electronic channel is shown in Fig. 3.10.

The analysis of the $\tau \rightarrow e$ channel benefits from the dense brick structure given by the cell design, which allows the electron identification through its showering in the downstream cells. More quantitative information about this item will be provided in the following chapters.

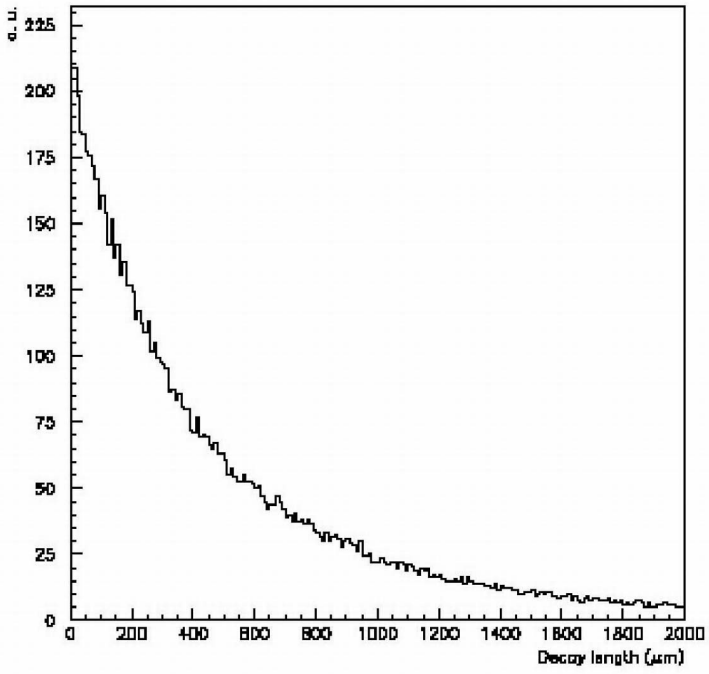

Fig. 3.9: τ decay length distribution, obtained assuming the CNGS energy spectrum and oscillation parameters coming from atmospheric neutrino experiments.

For the muonic decay mode the presence of the penetrating (often isolated) muon track crossing the whole detector structure allows an easier vertex finding. The potential background from large angle scattering of muons produced in ν_μCC interactions can be reduced to a tolerable level by applying cuts on the kink angle and on the muon transverse momentum at the decay vertex.

Hadronic decay modes have the largest branching ratio but are affected by background due to hadron interactions. One of the primary hadrons, in fact, can interact in the first lead plates and it may simulate the decay of the τ. Strong kinematical cuts will be used to reduce this background.

An important tool for background reduction is the determination of the transverse momentum of the daughter particle with respect to the direction of the τ track

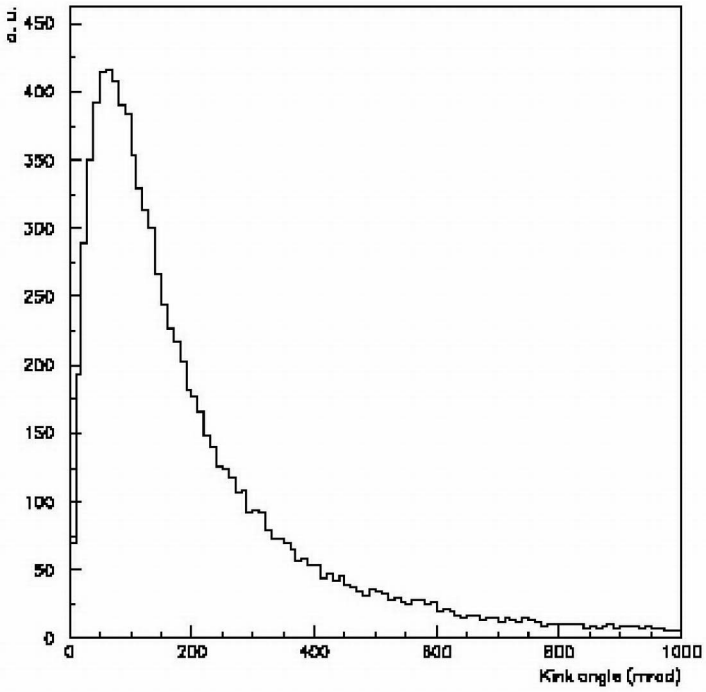

Fig. 3.10: τ kink angle distribution for the $\tau \rightarrow e$ decay mode.

candidate. For $\tau \rightarrow e$ decays the ECC technique is well suited to identify electrons and to determine their energy by measuring the density of track segments associated to their showering in the brick. For charged hadrons and muons, the momentum is deduced from the measurement of the multiple scattering in the lead plates. The muon momentum is also measured by the electronic detectors in a large fraction of cases.

The τ detection efficiency is estimated by evaluating the efficiency related to the various steps of data reconstruction:

- Trigger and brick finding
- Vertex finding
- Decay detection

- Kinematical analysis

The overall detection efficiency (including branching ratios) is reported in Tab. 3.3. Improvements on the τ detection efficiency are currently in progress. In particular, a more refined analysis is being planned and the multi-prong τ decay channel is under study.

	DIS long	QE long	DIS short	Overall
$\tau \rightarrow e$	2.7 %	2.3 %	1.3 %	3.4 %
$\tau \rightarrow \mu$	2.4 %	2.5 %	0.7 %	2.8 %
$\tau \rightarrow h$	2.8 %	3.5 %	-	2.9 %
Total	8.0 %	8.3 %	1.3 %	**9.1** %

Tab. 3.3: τ detection efficiencies (including branching ratios) for the OPERA experiment. Overall efficiencies are weighted sums on DIS and QE events.

3.4.2 Expected background

The background evaluation has been performed by means of a full simulation which includes the beam properties, the physics processes and the detector structure. All the backgrounds are given assuming the nominal CNGS intensity. Background sources are:

- prompt ν_τ production in the primary proton target and in the beam dump;
- one-prong decay of charmed particles;
- background from π^0 and prompt electrons;
- large angle muon scattering;
- hadronic reinteractions.

The contribution on the above sources to the total background depends on the actual decay channel.

Prompt ν_τ originate from the decay of τ's produced in the CNGS target by the decay of D_s mesons. The rate of ν_τ production from the interaction of 450 GeV/c protons in a Be target and in the downstream beam dump has been evaluated in [47, 48] for the CERN Wide Band Beam. These results have been scaled down according to the features of the CNGS beam and the distance of the experiment from the source. Following the method of [47], we expect $\mathcal{O}(10^{-6}) \times N_{CC}$ ν_τ interactions, where N_{CC} is the total number of ν_μ CC events collected. If one also takes into account the detection efficiency and the fact that the experiment will integrate $\mathcal{O}(10^4)$ events, the contribution to the background is completely negligible.

Charmed particles are produced in CC and NC neutrino interactions through the reactions:

$$\nu_\mu N \rightarrow c\,\mu X \tag{3.1}$$

$$\nu_\mu N \rightarrow c\bar{c}\,\mu X \tag{3.2}$$

$$\nu_\mu N \rightarrow c\bar{c}\,\nu_\mu X \tag{3.3}$$

Charged mesons have masses and lifetimes similar to those of the τ lepton. The above processes may thus constitute a background to the oscillation signal if one fails to detect the primary muon in the reaction 3.1, the charm partner in the reaction 3.3 of both (charm and muon) in 3.2. The most relevant source is given by single charm production, i.e. the first reaction. In order to evaluate the expected charm background, the uncertainties on the charm production cross section and decay branching ratios have been taken into account. The precision on the background evaluation benefits from the charm studies recently performed by the CHORUS experiment [49]. The evaluated overall background from charm is 0.38 events in 5 years.

In addition to charm production, other sources must be considered as possible background for $\tau \rightarrow e$ long decay: kink-like events from scattering of primary electrons produced in ν_e CC interactions and pion charge exchange process ($\pi^- p \rightarrow \pi^0 n$) in ν_μ NC interactions. The background from prompt electrons is estimated to be smaller than $1 \times 10^{-6} \times N_{CC}$ and the background from the pion charge exchange process is $\sim 0.2 \times 10^{-6} \times N_{CC}$.

Muons produced in ν_μ CC events and undergoing a scattering in the lead plate following the vertex plate could mimic a muonic τ decay. In order to have an experimental determination of this background a dedicated measurement of large angle scattering of 9 GeV muons in 2 mm of lead plates has been performed. The measured rate for scattering from 2 mm lead with $p_T > 250$ MeV is $(0.6^{+0.7}_{-0.6}) \times 10^{-5}$. This has to be compared with the predicted rate of 0.2×10^{-5} from an analytical calculation. Conservatively, the background rate in 5 years of OPERA running, is 1×10^{-5}.

The last source of background, important for all the decay channels, is due to the reinteraction of hadrons produced in ν_μ NC and in ν_μ CC interactions without any visible activity at the interaction vertex. Hadronic reinteractions constitutes a backgrounds for the hadronic channel if they occur in ν_μ NC events or in ν_μ CC events with the muon not identified. The expected background rate from hadronic reinteractions in the hadronic channel is about 4×10^{-6}. Hadron reinteractions constitute also an important source of background for the muonic τ decay channel. Indeed in ν_μ NC events an hadron may be misidentified as a muon or a genuine μ identified in the electronic detector is mismatched to a hadron track in the emulsions. The expected background rate from hadronic reinteractions in the hadronic channel is about 7×10^{-6}. Finally, hadronic reinteractions could also be a source of background for the electronic decay channel. This happens when in a ν_μ NC interaction (or in a ν_μCC interaction with the muon undetected) a hadron from the primary vertex, after having suffered a large scattering in the first or second downstream lead plate, is mis-identified as an electron. An estimate of the probability for this background has been given only using Monte Carlo data. Its experimental measurement is one of the main putposes of this thesis and will be discussed in the following.

The total background from the sources discussed, assuming the nominal beam intensity, is estimated to be $\sim$0.7 events. Improvement in the background reduction is in progress, in particular, recent achievements in the pattern and track reconstruction algorithms allowed a higher muon identification efficiency and a reduction of the probability to mismatch a genuine μ identified in the electronic detector with a hadron track in the emulsions. Other background reduction could come from a

re-evaluation of large angle muon scattering, hadronic re-interaction probabilities and improvements on the hadron-muon identification probability. Consequently the total background should be reduced by about 30%.

3.4.3 Sensitivity to $\nu_\mu \rightarrow \nu_\tau$ oscillations

Tab. 3.4 summarizes the OPERA performances after 5 years of running with the CNGS (4.5×10^{19} pot/year). The number of expected signal events from $\nu_\mu \rightarrow \nu_\tau$ oscillations is given as a function of the studied channel for three different values of Δm^2 at full mixing. A significance of 4σ is achieved after 5 years for $\Delta m^2 > 2.5 \times 10^{-3}$ eV^2.

The sensitivity of the OPERA experiment to $\nu_\mu \rightarrow \nu_\tau$ oscillation is shown in Fig. 3.11. The region allowed by the past atmospheric neutrino experiments is also shown: the OPERA sensitivity completely covers the allowed region.

3.5 Search for $\nu_\mu \rightarrow \nu_e$ appearance

In addition to the dominant $\nu_\mu \rightarrow \nu_\tau$ oscillation, it is possible that a sub-leading transition involving ν_e occurs as well. Having excellent electron identification capabilities, we have estimated the sensitivity in searching for $\nu_\mu \rightarrow \nu_e$ appearance with the CNGS beam.

channel	Signal for Δm^2 (eV^2)			ϵBr	Background
	1.6×10^{-3}	2.5×10^{-3}	4.0×10^{-3}		
$\tau \rightarrow e$	1.6	3.9	9.9	3.4 %	0.21
$\tau \rightarrow \mu$	1.3	3.2	8.2	2.8 %	0.22
$\tau \rightarrow h$	1.4	3.2	8.2	2.9 %	0.28
Total	4.3	10.3	26.3	9.1 %	0.71

Tab. 3.4: Summary of the expected numbers of τ events in 5 years for different Δm^2 with the expected background and detection efficiencies per decay channel for OPERA. Assuming the nominal CNGS beam intensity.

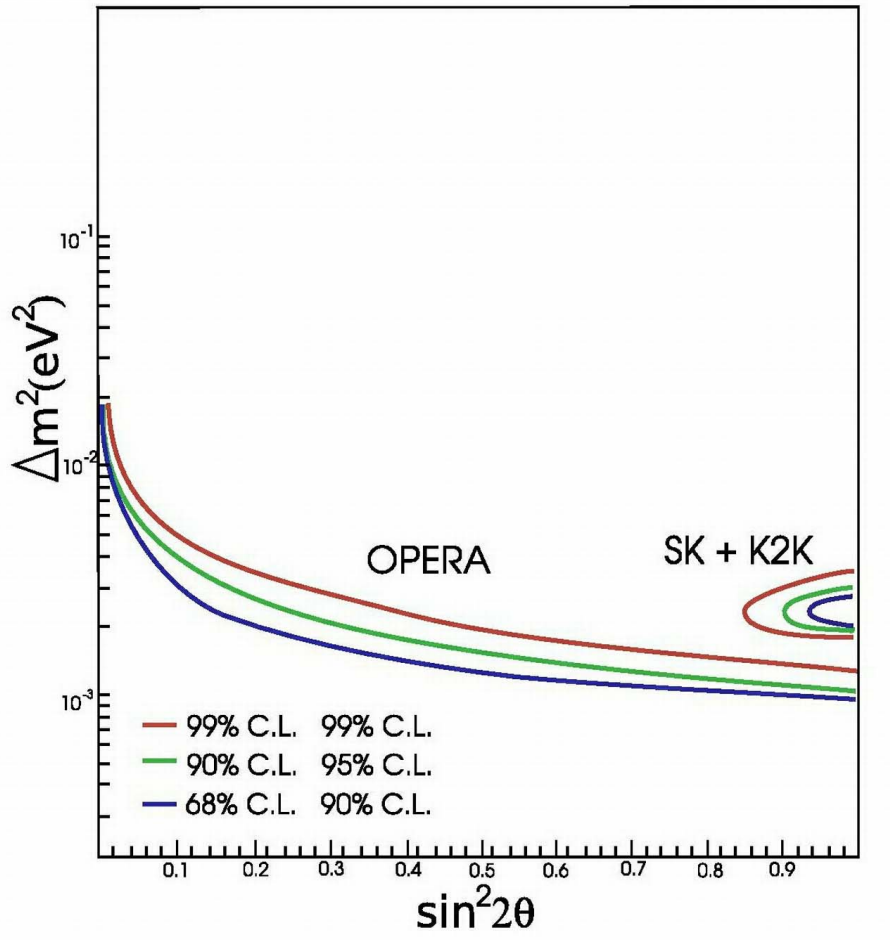

Fig. 3.11: The OPERA sensitivity to $\nu_\mu \rightarrow \nu_\tau$ oscillations. The parameter region allowed by SuperKamiokande and K2K combined is also shown.

The analysis is based on a search for an excess of ν_e CC events at low neutrino energies. The main background comes from the electron neutrino contamination present in the beam.

The OPERA $\nu_\mu \rightarrow \nu_e$ dedicated analysis seeks for neutrino interactions with a candidate electron from the primary vertex with an energy larger than 1 GeV and a visible event energy smaller than 20 GeV. These cuts reduce backgrounds coming from soft gamma conversion in lead and from genuine interactions of ν_e intrinsic

beam contamination. Moreover, a cut on the number of grains associated with the track of the candidate electron is also applied. Finally a cut on missing p_T of the event is applied ($p_T < 1.5$ GeV) to further reduce NC contaminations and suppress $\tau \rightarrow e$ background. For this analysis, hadron to electron mis-identification must be kept as low as possible, since ν_μ NC or ν_μ CC with the muon unidentified could mimic the searched signal.

If we assume that both $\nu_\mu \rightarrow \nu_\tau$ and $\nu_\mu \rightarrow \nu_e$ oscillations occur simultaneously with oscillation parameters $\Delta m^2_{23} = 2.5 \times 10^{-3}$ eV^2, $\theta_{23} = 45°$ and $\theta_{13} \in [3° \div 9°]$, the expected number of signal and background events in OPERA are given in Tab. 3.5. The rates are normalized to 5 years data taking and assuming the nominal intensity of the CNGS beam.

θ_{13}	$\sin^2 2\theta_{13}$	$\nu_e CC$ signal	$\tau \rightarrow e$	$\nu_\mu CC \rightarrow \nu_\mu NC$	$\nu_\mu NC$	$\nu_e CC$ beam
9°	0.095	9.3	4.5	1.0	5.2	18
8°	0.076	7.4	4.5	1.0	5.2	18
7°	0.058	5.8	4.6	1.0	5.2	18
5°	0.030	3.0	4.6	1.0	5.2	18
3°	0.011	1.2	4.7	1.0	5.2	18

Tab. 3.5: Expected number of signal and background events for OPERA assuming 5 years data taking with the nominal CNGS beam and oscillation parameters $\Delta m^2_{23} = 2.5 \times 10^{-3}$ eV^2, $\theta_{23} = 45°$ and $\theta_{13} \in [3° \div 9°]$. [50]

An increase of sensitivity for $\nu_\mu \rightarrow \nu_e$ oscillation can be obtained by fitting the kinematical distributions of the selected events. By fitting simultaneously the E_{vis}, E_e, p_T^{miss} distributions, we obtained the exclusion plot at 90% C.L. shown in Fig. 3.12 under the assumption $\theta_{23} = 45°$.

The sensitivity of the combined experiments running with the present high energy CNGS beam is comparable to the one achievable with a dedicated low energy configuration running below the kinematical threshold for τ production and is obtained as a by-product of the search for ν_τ appearance.

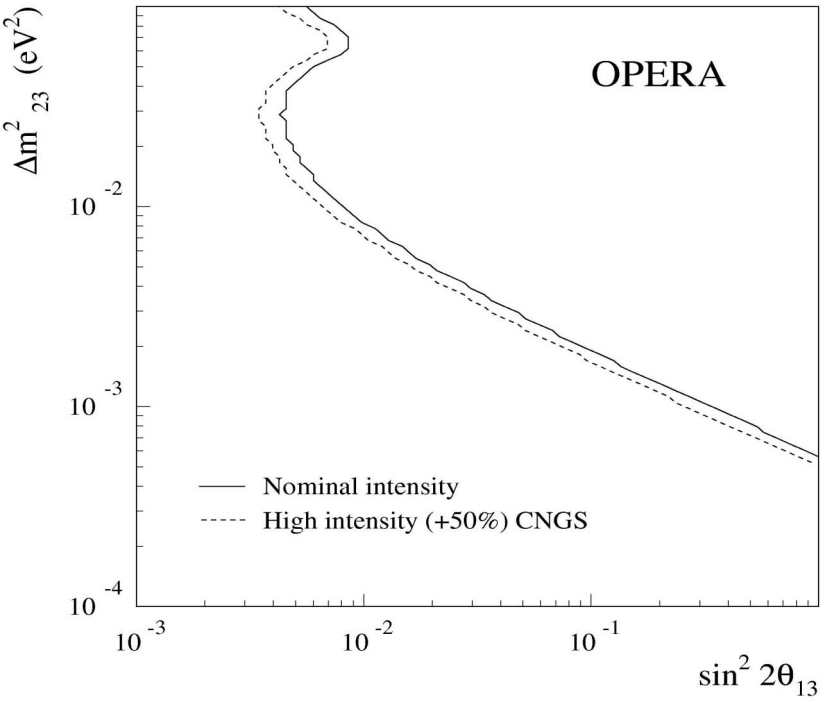

Fig. 3.12: OPERA sensitivity to the parameter θ_{13} at 90% C.L. in a three family mixing scenario, in presence of $\nu_\mu \rightarrow \nu_\tau$ with $\theta_{23} = 45°$. The sensitivity with the higher intensity beam ($\times 1.5$) is also given (dotted line).

Chapter 4

Nuclear emulsion properties

4.1 Introduction

The use of photographic emulsions to study nuclear particles began in 1896, when H. Becquerel discovered radioactivity by observing the blackening of photographic plates accidentally in contact with uranium salts. Some years later individual tracks of α-particles and protons were seen in emulsions. The first example of interaction in emulsion were reported in 1937 by Blau and Wambacker from the analysis of emulsion plates exposed to cosmic rays [51].

The most fundamental contribution of the emulsion technique to particle physics has been the discovery of the pion in 1947 by observing the $\pi \rightarrow \mu \rightarrow e$ decay chain in nuclear emulsions exposed to cosmic rays [52] . During the 50's and 60's emulsions were used for cosmic ray experiments, electromagnetic shower energy measurements and momentum measurements and several other particles were discovered.

Nuclear emulsions were successfully used in neutrino experiments like WA17 at CERN for charmed particles searches in neutrino charged current interactions [53], E531 at Fermilab for the measurement of charmed particle lifetimes in neutrino interactions [54], and WA75 at CERN searching for beauty particle production induced by a 350 GeV/c π^- beam [55]. Furthermore, the use of nuclear emulsion allowed the observation of τ neutrinos by the DONUT collaboration [56].

Nuclear emulsion still remain the detection technique with the best known three-dimensional spatial resolution, less than 1 μm, and zero intrinsic dead time. The development of automatised scanning systems during the last two decades has made possible the use of nuclear emulsions as a target in massive experiments.

4.2 Basic properties of emulsions

Nuclear emulsions are made of micro-crystals of silver halides (usually bromides AgBr) suspended in a gelatin composed by organic materials. The linear dimension of the crystals range from 0.1 μm to 1 μm. The size of the microcrystals in the OPERA emulsions is $\sim$ 0.2 μm and is well controlled by the current industrial technologies developed for photographic films. The passage of charged particles can become visible through a chemical amplification of the atomic-scale perturbations induced by energy losses of ionizing particles.

Nuclear emulsions are similar to photographic emulsions, but with several peculiar features: silver halide crystals are very uniform in size and sensitivity; the silver to gelatin ratio is much higher than in a conventional emulsion; furthermore, the film thickness is larger.

4.2.1 The latent image formation

A characteristics of silver halides is that, if they are opportunely excited by light or ionising radiation, the energy provided to the crystals produces a *latent image* which is almost stable in time.

A developing agent reduces the AgBr to metallic Ag more rapidly in the irradiated crystal than in the others. The absorption of a light quantum causes the ionization of a bromine ion, which is thus transformed into a bromine atom. The ejection of an electron leads to a region of positive charge in the lattice which is referred to as a *positive hole*. The ejected electron is not free: it can be regarded as associated with the silver lattice and it can move inside it neutralizing in turn one of the silver ions. The effect of the absorption of the quantum is therefore to

transform two ions into two atoms.

Both electrons and positive holes can diffuse inside the crystal: the holes are trapped at lattice imperfections on the outer surface while electrons are trapped by impurities used for sensibilization.

It is important for latent image formation that a significant proportion of electrons and positive holes are trapped separately, otherwise they could recombine and regenerate halide ions. The silver halide crystal contains free (interstitial) silver ions, which can move through the lattice. When an interstitial silver ion encounters a trapped electron, the charges are neutralised and an atom of metallic silver is formed. In this way, the absorption of energy in a exited crystal of silver halide leads to a concentration of a few silver atoms into an aggregate which can act as a development centre, i. e. a latent image.

The formation and preservation of the *latent image* depends on external conditions such as: temperature, humidity, pressure. As temperature and humidity increase, the sensitivity decreases and the latent image is less stable (*fading*). The fading can be artificially induced in order to erase the image of unwanted tracks accumulated before the exposition (*refresh*). Moreover, in particular conditions, it is possible to refresh emulsion without spoiling their sensitivity.

4.2.2 Development and fixation

Photographic development is the process by which the latent image contained in an emulsion is made visible by the reduction of silver ions in the silver halide crystal to metallic silver. The reducing solution, *the developer*, is chosen with the aim of reducing completely those crystals containing a latent image centre, while leaving unchanged those not containing a centre. The development time used for processing should be sufficient for those crystals with a latent image centre to be reduced completely, but not so long that unexposed crystals are developed. In practice, a certain number of crystals will be developed even though they do not contain a development centre. These grains, when developed, constitute what is known as *fog* or background.

Developing agents may be divided into two main groups, depending on the source of silver ions for reduction. In practice, most developers give a combination of the two sorts of development.

The first group is known as physical developing agents: in these, silver ions are provided from the solution in the form of a soluble complex. They are deposited on the latent image centre and are reduced to metallic silver. This produces spherical grains, the precise shape of which is affected by pH.

The second group is the chemical developing agents. In chemical development, silver ions are provided from the silver halide crystal containing the latent image centre. The action of a chemical developer produces a mass of filaments bearing little resemblance to the original crystal. If silver halide solvents such as sulphite are present in a chemical developer, an opportunity exists for some physical development to occur. In this case, the filaments in the processed plate will be shorter and thicker.

Chemical development, like many other chemical reactions, is dependent on temperature. In general, development occurs more rapidly at higher temperatures - below 10°C development virtually stops. For this reason it is important to keep the processing temperature constant during development, otherwise it will not be possible to assess the correct development time.

The choice between a physical developer and a chemical developer will largely depend on the grain structure required in the processed image.

After the development a fixation procedure must be held, in order to remove all the residual silver halide. This, if otherwise left in the emulsion, would slowly induce the browning and degrading of the image. The fixing agents most widely used are sodium or ammonium thiosulphate, which form thiosulphate complex with the silver halide. Silver thiosulphate is soluble in water and so may be removed from the emulsion by washing.

It is important to use a fixer which has not been exhausted when processing nuclear emulsions, otherwise some silver halide will remain in the emulsion. To ensure that it is all removed a fixing time should be used which is twice the time it takes for the emulsion to clear.

After fixation, emulsions must be washed very thoroughly to remove all the silver thiosulphate complexes: if any remains, they will eventually break down, forming silver sulphide which is brown and will obscure the image.

After the development, all the crystals containing a latent image centre are reduced to metallic silver. The other crystals are removed by fixing, and the result is a series of dark silver grains of about of 0.6 μm size, which can by observed using optic microscopes. The paths of an ionizing particle is visible as a sequence of these grains.

4.3 OPERA emulsion films

The total area of emulsion films in the OPERA detector is $\sim$ 150000 m^2. This corresponds to 18 m^3 of dried emulsion gel.[1] The emulsions used for the past experiments, were poured by hand following standard procedures developed in many years of experience. The same procedure applied to OPERA would be prohibitively time consuming. To overcome this problem, an R&D project has been carried out by Nagoya University and the Fuji Film company to establish the process of automatic coating of nuclear emulsion films. After several tests, it is confirmed that the OPERA emulsion film can be produced by commercial photographic film production lines. The required amount of films needed for the experiment will be produced within two years. Fig. 4.1 shows the cross sectional view of the newly developed machine-coated emulsion film.

As opposed to hand-made films, the thickness can be precisely controlled as in the case of commercial colour films. The measure of the film emulsion layer thickness after development shows a distribution with $sigma \sim 1.3$ μm.

As shown in Fig. 4.1, each film has a protective gelatin layer of 1 μm thickness over the sensitive layers. This prevents the occurrence of black or grey patterns on the emulsion surface. These patterns, frequently emerging in the case of hand-

[1] For comparison, the amount of emulsion handled for CHORUS is equivalent to a surface of 500 m^2 and to a 0.4 m^3 total volume of dried emulsion.

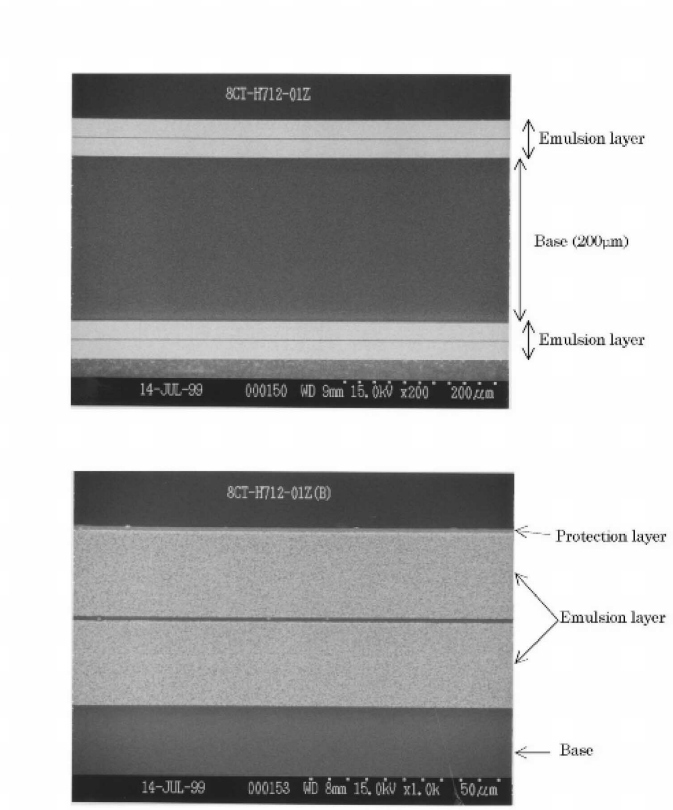

Fig. 4.1: Top: photograph of the cross section of a machine-coated emulsion film taken by an electron microscope. Diluted emulsion layers of 42 μm thickness are coated on both sides of a 200 μm thick triacetate base. Bottom: enlarged view of the top emulsion layer. A thin ($\sim$ 1 μm) protective film (gelatin) is placed over the emulsion layer at the same time of coating.

poured plates, are due to silver chemically deposited during the development. The removal of these stains had been the most time-consuming task in the emulsion pre-processing for the experiments performed so far. By means of the protective coating, surface cleaning is not needed anymore and the pre-processing procedure becomes compatible with the daily handling of thousands of emulsion films, as in the case of OPERA.

In addition, the presence of this protective layer allows direct contact with the

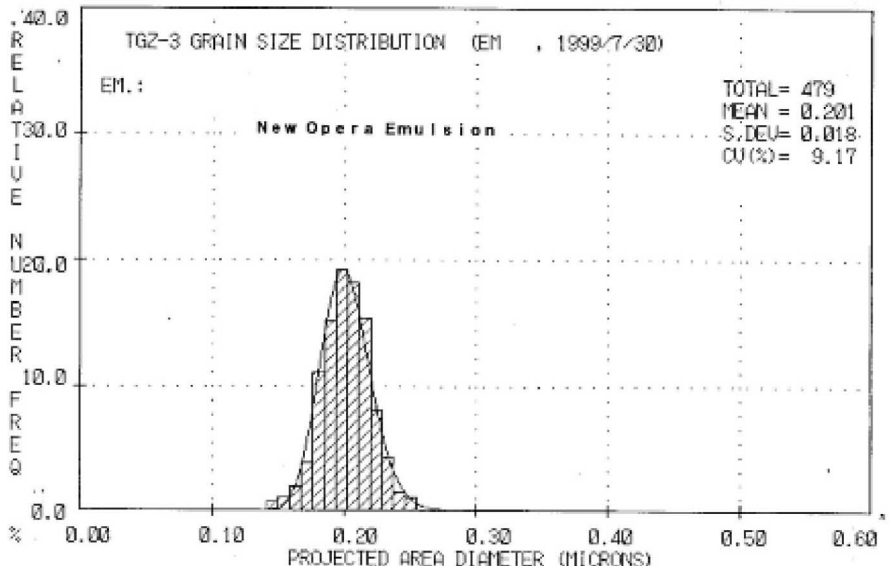

Fig. 4.2: Crystal diameter distribution of the Fuji emulsion layers. The distribution is rather uniform around 0.20 μm.

lead plates. Without this protection, one would have to insert thin insulator sheets in order to avoid chemical reactions between the lead plates and the silver halides contained in the emulsion.

For automatic coating some dilution of the gel is required. Under normal conditions, the grain density, defined as the number of grains per 100 μm along the particle trajectory, decreases almost linearly with the dilution factor although part of the sensitivity loss may be regained in the development phase. This problem has been solved by increasing the sensitivity of each crystal using the technology of crystal growth developed for standard photographic films.

As shown in Fig. 4.2, the crystal diameter distribution in the emulsion layer is rather uniform around 0.20 μm. The currently achieved grain density of the machine-coated emulsion films is 30 grains/100 μm even in the case of a factor of two dilution.

The so-called emulsion fog is due to accidentally developed grains randomly

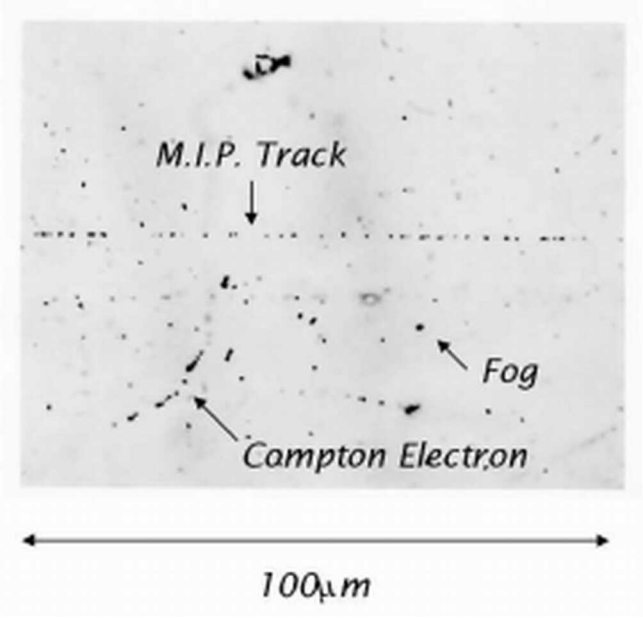

Fig. 4.3: Photograph of a minimum ionising particle (mip) recorded in an emulsion layer. The grain density is defined as the number of grains per 100 μm track; the fog density as the number of fog grains per 1000 μm^3.

distributed in the emulsion volume (Fig. 4.3). They constitute a background which has to be kept at the level of ≤ 5 fog grains /1000 μm^3. This can be achieved by applying a moderate development to the emulsion films, still keeping a sufficient sensitivity of ~ 30 grains/100 μm, as shown in Fig. 4.4.

The intrinsic position resolution of the emulsion films can also be investigated by measuring the position residuals of the centre of each grain with respect to a fitted straight line. The result is shown in Fig. 4.5. The measured resolution of $\sigma \sim 0.06$ μm can be compared with the expected value of 0.058 μm ~ 0.2 μm$/\sqrt{12}$, where 0.2 μm is the diameter of the original crystal. This result implies that the crystal uniformly grows under development up to a grain with diameter of ~ 0.6 μm.

The physics properties of emulsions are the following: density $\rho = 2.40$ g/cm^3, average atomic number $< A >= 18.2$, average atomic charge $< Z >= 8.9$, radiation length $X_0 = 5.5$ cm, $(dE/dx)_{mip} = 1.55$ MeV/g/cm^2 or 37 keV/100 μm, nuclear collision length $\lambda_T = 33$ cm and nuclear interaction length $\lambda_I = 51$ cm.

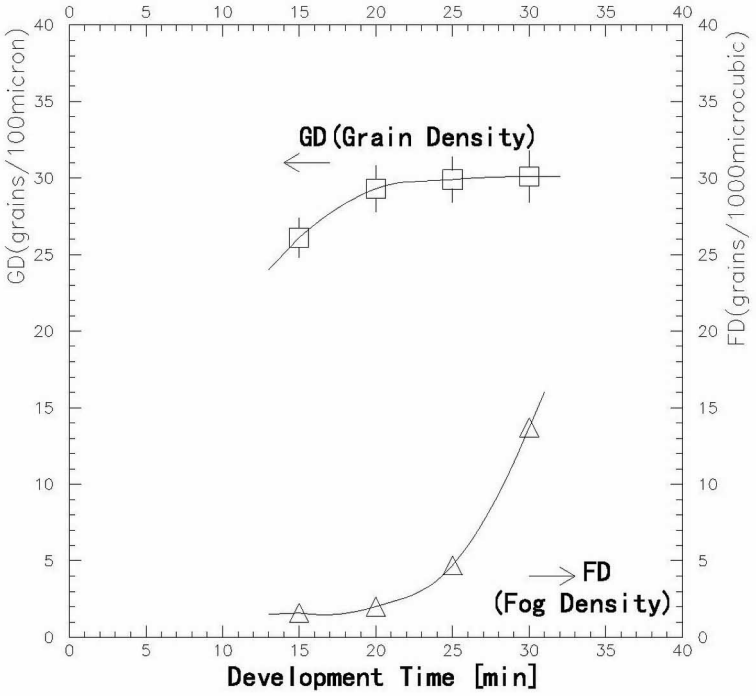

Fig. 4.4: Time dependence of the developed grain density and fog density. Conditions are: amidol developer at 20°C. A development time from 20 to 25 minutes gives satisfactory results.

4.3.1 Production and refreshing

OPERA emulsions are produced in Japan by Fuji Photo Film Company. After an R&D activity jointly conducted with Nagoya University the process of automatic machine coating of nuclear emulsion films was established. Emulsions are thus produced with the production line for commercial photographic films. The total amount of emulsion sheets needed for the experiment is about 12 millions. The production started on April 2003 and 4.3 millions have already been produced. Due to their continuous sensitivity, the emulsion plates collect latent track images, mainly from

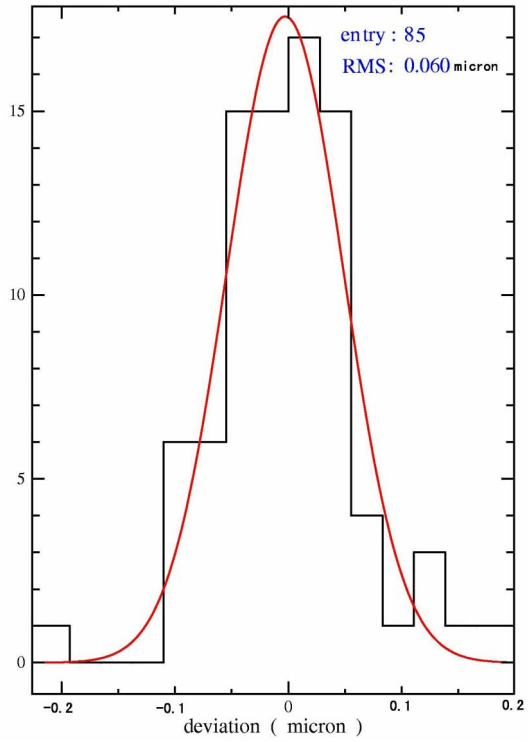

Fig. 4.5: Position residuals of the grain center with respect to a fitting straight line.

cosmic-rays and ambient radioactivity. In order to erase them, the Nagoya group tested an accelerated fading procedure. This is obtained by placing emulsion sheets at moderate temperature and high humidity for a few days. This procedure, which cancels about 96% of the latent tracks, is known as *refreshing*.

After production, the OPERA emulsions are stored in the Tono mine, in Japan, where a refreshing facility has been set up. Emulsions are stored for three days at 30°C and 98% relative humidity. The characteristics of the refreshed samples are reported in Tab. 4.1. After the refreshing procedure, the emulsion sensitivity is a bit lower (33 grains/100 μm) while the surviving tracks have only 13 grains/100 μm and this value produce the desired refreshing efficiency.

More then one million of nuclear emulsion have already been refreshed in the Tono mine. After refreshing, the emulsions are packed and then shipped to the

	Before refreshing	After refreshing
Sensitivity	36 grains/100 μm	33 grains/100 μm
Fog density	2.5 grains/1000 μm^3	3.5 grains/1000 μm^3

Tab. 4.1: Sensitivity and fog grain density for the OPERA emulsions, as measured before and after the refreshing procedure.

Gran Sasso laboratory.

4.3.2 Distortions

Distortion is a phenomenon which shifts the position of the recorded trajectories in the emulsion layer because of stresses accumulated in the gelatin layer. In hand-made emulsion plates, shifts of several μm are frequently observed, caused by a not uniform drying at the plate production.

The simplest form of general distortion is a uniform shear: straight tracks remain rectilinear but their direction and length change by an amount which depends on the magnitude and direction of the shear.

A more serious source of error is due to differential shear of the emulsion in which both the magnitude and direction of the shear change with depth. Such distortion changes the tracks of an energetic particle from a line into a curve.

In the case of emulsions mounted on a glass or plastic base, as for OPERA emulsion plates, the points on tracks are assumed to be unaltered by the processing [57]. The distortion affects the efficiency in connecting the two tracks measured in the two emulsion layers of a film. If connected, *base-tracks* are constructed connecting the two end points so that base-tracks have positions and angles not affected by distortion.

Distortions can vary from one region of the emulsion sheet to another, but in well-processing conditions they do not change rapidly in passing over distances of the order of a centimetre. Fig. 4.6 shows the typical distortion pattern in the central part of an emulsion film. The distortion effect is very much suppressed in industrial films, down to ~ 0.4 μm. This result is due to the uniform drying process at production

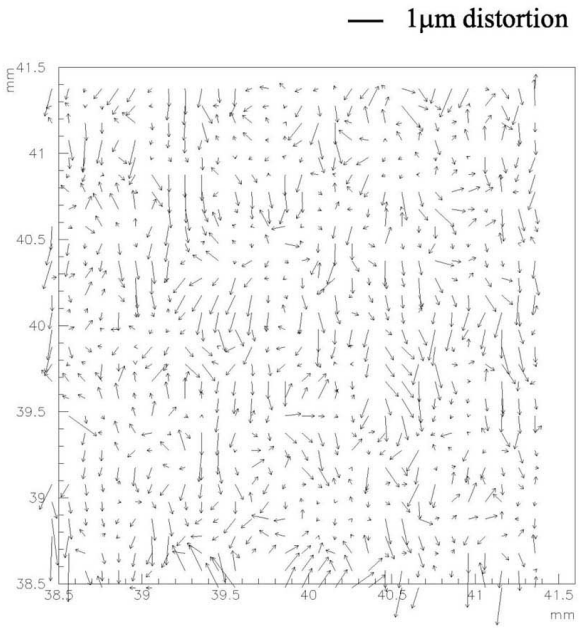

Fig. 4.6: Measurement of the emulsion distortion at the centre of an emulsion film (from the OPERA proposal). The scanning area is ≈ 3 mm x 3 mm. The vectors indicate the distortion direction. The absolute value of the distortion is indicated by the length of the arrow.

and also to the careful development treatment specially devised for OPERA.

Usually the distortion becomes larger near the edge of the film. In the case of OPERA emulsion films, the distortion is lower than ~ 1 μm up to 1 mm from the film edge. Only at about 100 μm from the edge the film is damaged, due to black stripes caused by the pressure applied at the film cutting.

4.3.3 The shrinkage factor

After processing, an emulsion will occupy less volume than before unless some material is added to replace the silver halide dissolved by the fixer. The most conspicuous evidence of this effect is a reduction of the thickness of the emulsion layer.

For any quantitative measurements of track density, ranges, and angles in the emulsion, it is important to measure the precise original thickness.

The *shrinkage factor* is the ratio of the thickness of emulsion at the time of exposure divided by its thickness after the developing process.

Both gelatin and glycerine are hygroscopic so that the actual equilibrium thickness (and also the index of refraction) depends on the ambient humidity. A normal processed emulsion changes its thickness with the ambient humidity in a way that is given roughly, when the humidity is near 60%, by:

$$\frac{\Delta t}{t} \cong \frac{RH^2}{3 \cdot 10^4} \tag{4.1}$$

where t is the nominal thickness, Δt is the increase from the dry thickness and RH is the relative humidity in per cent.

4.3.4 Fading and aging

The fading and aging features of the OPERA industrial emulsion films have been investigated. Fading is the loss of the latent image occurring prior to development. Aging is the degradation of the emulsion sensitivity during the exposure.

Fading is not a severe problem for the OPERA experiment, since we plan to extract the selected brick and develop the emulsions within one week after the event occurred. Within about one month, possible extra bricks required for further analysis (candidate events) are extracted and developed. Moreover, one can take advantage of the existence of some fading, which contributes to erase unwanted cosmic ray tracks accumulated during film production and transportation before the run, as described in the next Section. This feature is beneficial to suppress the degradation of the electron identification efficiency and obtain an adequate energy resolution for cascade showers. In principle, the fading time constant depends on the environmental temperature, humidity and on the oxygen density. One example of these properties is shown in Fig. 4.7. According to the film producer, fading properties are well under control.

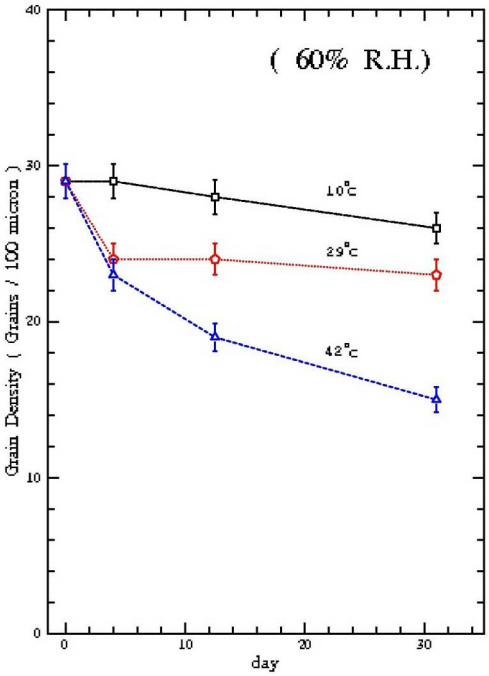

Fig. 4.7: Examples of fading properties of the OPERA emulsion film. Each film is packed at 60% and 20°C. After a beam exposure, the samples have been stored at different temperatures. At 10°C the time needed to reduce the grain density to 25 grains/100 μm is estimated to be 1.5 to 2 months.

In order to check the features of the Fuji emulsions, tests on sensitivity has been performed by exposing all plates of emulsions to an electron beam and by developing them soon after. The results are that even the oldest plates still show enough sensitivity, i.e. $\geq$ 25 grains/100 μm. The situation is even better for OPERA, since the natural temperature of the Gran Sasso hall is appreciably lower. Therefore, the OPERA emulsion sensitivity will be preserved over their (maximum) 7 years lifetime (i.e. 2 years for production and 5 years for exposure).

Chapter 5

The automatic scanning system

5.1 Introduction

The features of nuclear emulsions as a detector have been known since a long time. For several decades since their appearance in physics research, their use has been exclusively connected with scanning and analysis by human eyes. However, in the last years, the process of nuclear emulsion scanning has considerably changed because of the birth of automatic scanning systems.

The automation of emulsion scanning has been pioneered by the group of Nagoya University (Japan) and the first complete application of an automatic system, called *Track Selector* TS, was used for the DONUT and CHORUS emulsion analysis [58, 59].

The Track Selector was designed to detect tracks with predicted angles in the field of view of a CCD camera. The track detection algorithm is simple: 16 tomographic images of (e.g.) 100 μm thick emulsion layers are taken and digitised. Each image is shifted horizontally respect to the first layer, so that the predicted tracks become perpendicular to the emulsion surface. Tracks are identified by superimposing the sixteen shifted digitised images. The basic TS tracking principle was used in its improved version *New Track Selector* and *Ultra Track Selector* taking advantage of the implementation of several image processors working in parallel. The maximum

scanning speed is about 2 cm^2/h.

The OPERA experiment requires an improvement of about a factor of ten in speed, i.e. a speed of about 20 cm^2/h. To achieve this goal, two different *R&D* programs are carried out.

The Nagoya University group aims to a further improvement of the UTS system (the so-called Super-UTS). The key features of the S-UTS are the high speed camera with 3 kHz frame rate and a piezo-controlled displacement of the objective-lens, synchronized to a continuous stage motion in order to avoid "go-stop" of the microscope stage while taking images. The system uses Fast Programmable Gate Arrays (FPGAs), fast memory and a grabber board connected to the CCD camera (512×512 pixel).

European groups followed a different approach, initiated by the Salerno group with the SySal system for the CHORUS experiment [60]. With this approach, called *multi-track system*, all tracks in each field of view are reconstructed regardless of their slope.

Strategy of this project is the use of the *state-of-art* commercial hardware components. The software used for data taking and track reconstruction is conceived in a modular structure, which provides the flexibility needed to upgrade the system following the technological progress.

The Bologna group joined the European Scanning project for the OPERA experiment in all the *R&D* phases and the first prototype was assembled and set-up in 2002 [61] with a scanning speed of about 1 cm^2/h. The last version of the system, upgraded both in hardware and software, has been set-up in 2004 and can reach the required scanning speed of 20 cm^2/h.

5.2 The readout system

Conceptually, a microscope for automatic emulsion scanning consists of a computer driven mechanical stage, an appropriate optical system, a photodetector -typically a CCD or CMOS camera- and its associated readout as shown in Fig. 5.1.

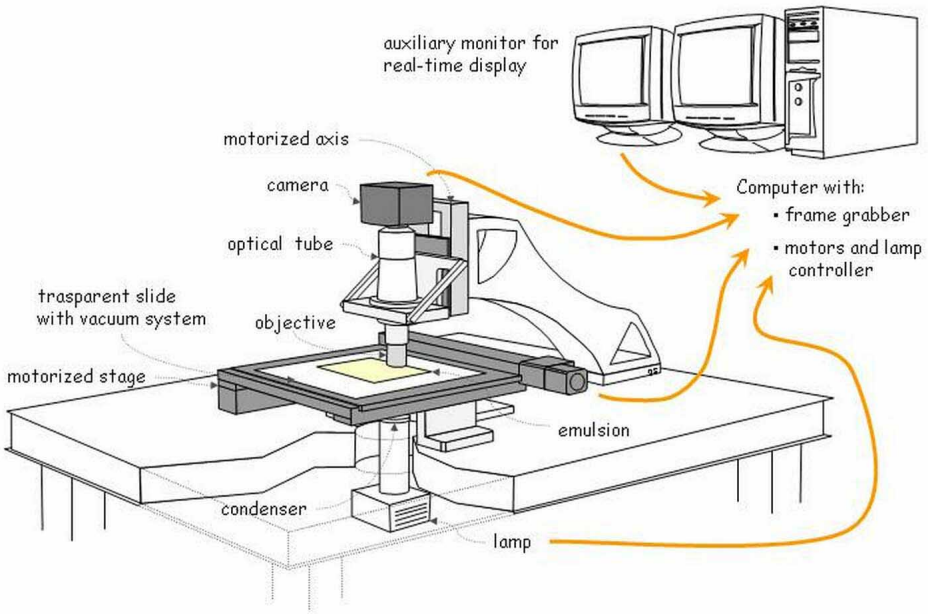

Fig. 5.1: Layout of a typical automatic scanning system for nuclear emulsions.

During the acquisition, the emulsion is scanned view by view and the images are sent to the frame grabber hosted in a computer, which also controls the light intensity and the stage displacements. In particular the readout is performed by moving the best focus plane of the objective inside the emulsion with constant speed and, for each field of view, a series of successive vertical images is taken by the camera (Fig. 5.2).

The scanning system design had to take into account the request of a high scanning speed and position and angular accuracies adequate for event analysis. The system was conceived with the following features:

- high-performance mechanics with sub-micron position accuracy and very small settling-time;
- optics with a large field of view, sub-micron resolution and a suitable working distance;

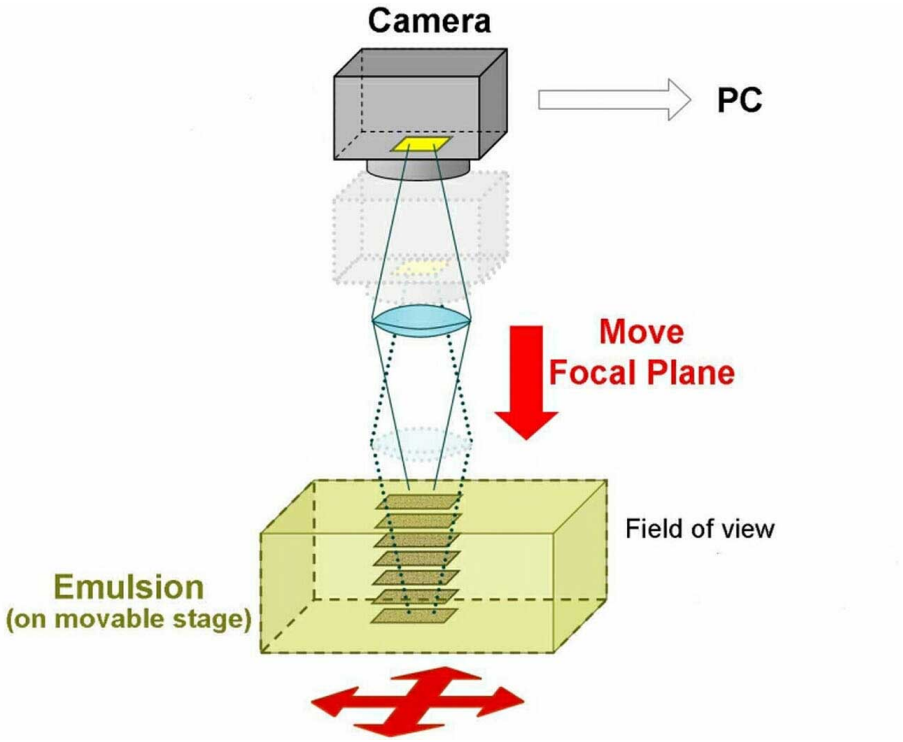

Fig. 5.2: The readout: for each field of view several tomographic images of the emulsion are taken by moving the focal plane.

- camera with mega-pixel resolution and high frame rate;
- powerful image processors.

One of the automatic scanning systems in the Bologna laboratory is shown in Fig. 5.3.

Since precision optical measurements depend on reliable position stability, the motor driven scanning table and a granite arm are fixed to a high quality table, which provides a virtually rigid and vibration-free working surface that holds the components in a fixed relative position. The light system is located below the microscope table. Vertical displacements are obtained by a motor driven stage, which is fixed to the granite arm. The optics and the digital camera for image grabbing are mounted on the vertical stage. The emulsion support is provided with a vacuum system to keep the sheet steady during the data taking.

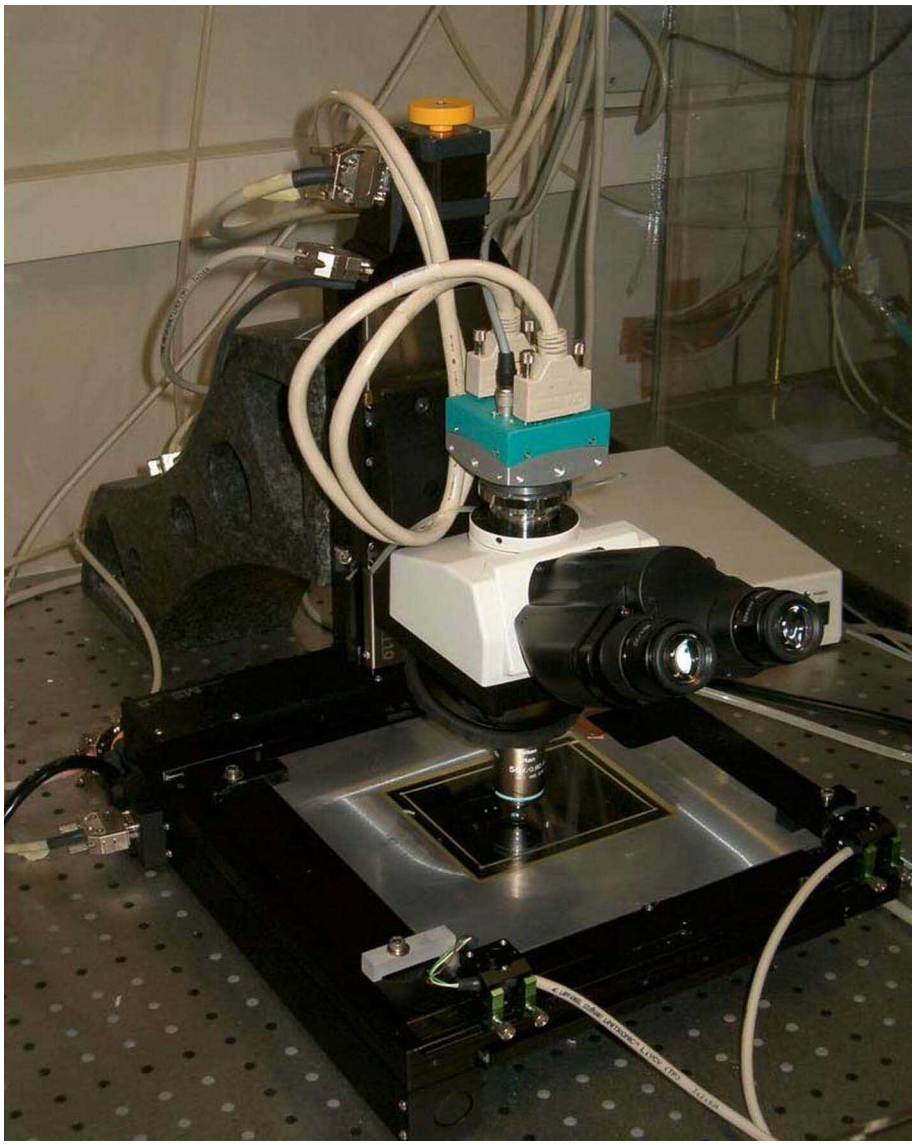

Fig. 5.3: The European Scanning System in the Bologna laboratory.

5.2.1 Mechanical stages

The scanning table and the vertical stage have been developed in collaboration with the Micos company[1]. They are commercial products modified according to the OPERA specifications.

The stages are equipped with NanoStep RFK Series 5-Phase Microstepping stepping motors produced by the Japanese company Vexta. Stepping motors are excellent for precise position control. The stage controller is a FlexMotion board provided by National Instruments and is inserted into the host PC.

A Micos MS-8 scan table with a 20.5×20.5 cm^2 range on horizontal directions is mounted on the tabletop. The stage horizontal coordinates are read out by two linear encoders with an accuracy of 0.1 μm. The limit switches are integrated in the scan table. The displacement of the horizontal stage is one of the crucial points to obtain a suitable scanning speed. Speed and acceleration have to be chosen in order to minimize the time needed to change the field of view.

The vertical linear stage is provided by the Micos company (model LS-110). It is equipped with an integrated linear encoder with an accuracy of 0.1 μm. The limit switches are integrated in the stage but the lower one was modified and substituted by an optical one based on a photodiode in order to have a better precision and to prevent the objective to touch and scratch the emulsion. It can be tuned depending on the emulsion thickness, on the dimension of the objective and on the glass plate.

5.2.2 The optical system

The main components of the optical system are the objective and the trinocular tube, both from the Nikon company. The optics is based on a Nikon infinity optical system: the objective is designed so that light emerging from the rear aperture is focused to infinity. A second lens hosted in the trinocular, known as tube lens, forms the image at its focal plane.

As already described in the previous chapter, Fujii emulsion sheets have emulsion

[1]MICOS ITALIA GmbH, via S. Protaso, 39 I-20010 Bareggio MI

layers on both sides of a 210 μm thick transparent plastic base. In order to see the back side of the emulsion, the objective is requested to have a *Working Distance* (WD) larger than 300 μm and the *Numerical Aperture* (NA) as large as possible.

Since spherical aberrations increase as the cube of NA, the variation of the intermediate medium between objective and focal plane should be small. For this reason an *oil-immersion objective* is the best solution because typical immersion oils have a refractive index of 1.51, similar to the emulsion (~ 1.51) and plastic base (~ 1.48) refractive indices. Hence light rays pass through an optically homogeneous medium.

The objective of the European Scanning System is produced by Nikon[2] and its characteristics match the OPERA requests.

The camera is the MC1310 from the Mikrotron[3] company. It is an high-speed megapixel CMOS camera with Full Camera Link interface[4]. Unlike high resolution CCDs, modern CMOS sensors offer high resolution and extremely high data rates.

The CMOS sensor has 1280×1024 pixels, each pixel size if 12 μm (giving a sensor area of 1.5×1.2 cm^2). The camera is able to work up to a rate of 500 frames per second (fps) at full resolution, which implies a maximum data rate of 660 MB/s. The Scanning System uses a camera configuration at 376 fps, which is satisfactory for the requested scanning speed.

The images are grabbed in a 256 level grey scale (the light acquired by one pixel is converted in a 8-bit digital signal) and sent to the frame grabber in the host PC. A typical emulsion image, as it appears in the monitor, is shown in Fig. 5.4.

The frame grabber and the image processor are integrated in the same board: the Matrox Odyssey Xpro, the most recent vision processor produced by the Canadian Matrox company. The Odyssey board is specifically designed for fast transfers and on-board processing. It bears a Motorola G4 PowerPC microprocessor and 1 GB DDR SDRAM memory. The internal bandwidth can manage over 4 GB per second,

[2]Nikon CFI Plan Achromat 50x oil, NA 0.90, WD 0.4 mm.
[3]Mikrotron GmbH Landshuter Str.20-22 D-85716 Unterschleissheim Germany.
[4]Camera Link is a new communication protocol for high speed digital cameras.

Fig. 5.4: A typical emulsion image grabbed with the CMOS camera. The image dimension is 360 μm $\times$ 280 μm with 1280 $\times$ 1024 pixels.

while the external I/O bandwidth up to 1 GB per second.

5.2.3 The light system

The light system, developed by Nikon-Italy, is placed below the scanning table. The light from the lamp-house is directed into the microscope base through a collector lens, and then through a glass diffuser, before being focused on the aperture diaphragm of the sub-stage condenser. The use of the diffuser gives the advantage of a more homogeneous beam of light entering the condenser and therefore the intensity of light cone produced.

In the so-called Koeler illumination setup, an image of the light source is focused at the condenser aperture diaphragm to produce parallel (and unfocused) light through the plane of the specimen. The condenser gathers light and concentrates it into a cone of light that illuminates the specimen with uniform intensity over the entire field of view. A wide cone of illumination is required for optimum resolution of the specimen. The condenser light must be properly adjusted to opti-

mize the intensity and angle of the light entering the objective front lens. The size of the condenser aperture diaphragm can be used to control the numerical aperture of the light cone that illuminates the sample. A field diaphragm controls the quantity of light entering the sub-stage condenser.

5.3 The on-line acquisition software

The online DAQ software for the emulsion automatic scanning and track segments reconstruction was developed using the object-oriented C++ language. It is based on a modular structure where each object carries out a well defined task. Each object has a corresponding parameter window for configuration setting. In Fig. 5.5 the program control panel and the parameter window of the main object are shown.

The list of all modules with their functionality is given in Tab. 5.1.

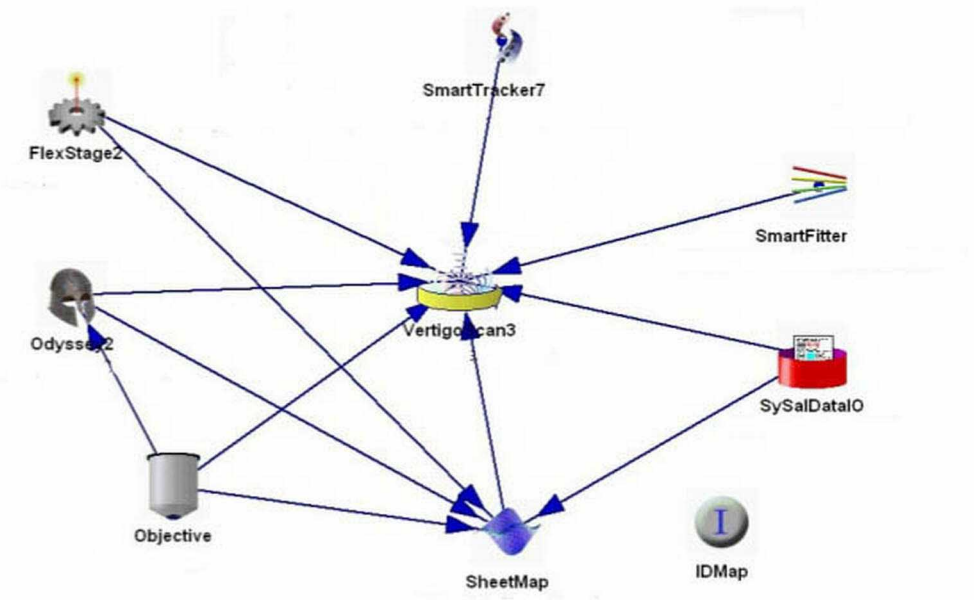

Fig. 5.5: The control panel of the online acquisition system, where the objects are represented.

Name of the module	Functionality
Objective	stores the information related to the used objective and performs the pixel to micron conversion
Odyssey2	drives the Odyssey board
FlexStage3	is interfaced to the stage controllers and set the movements modalities
SmartTracker7	is responsible for track pattern recognition, recognizing sequences of geometrically aligned clusters.
SmartFitter	performs the tracks fit.
DataIO	handles data Input/Output.
SheetMap2	transforms coordinates and vectors from the current stage reference frame to the emulsion local reference system defined by a grid of fiducial marks printed on the emulsions).
VertigoScan3	is the steering module, which uses all the other objects to control the scanning.

Tab. 5.1: List of the modules composing the on-line acquisition software.

The scanning output is a collection of raw data files (in binary format) which are saved in the file server. An Oracle database, where the output of data taking will be stored, is under development.

5.3.1 Image processing and clustering

Images are digitised and converted to a grey scale of 256 levels (where 0 is black and 255 is white). Digital images are analysed for *clusters* recognition. Some of these clusters are track grains in the emulsion layers, most are fog grains. Sometime few clusters are camera dark spots due to the presence of dust on the camera sensor. The flat field subtraction is an on-line image process studied to remove them in order to prevent the reconstruction of vertical fake tracks. The operation consists in the subtraction of one image grabbed outside of the emulsion from all the other images grabbed inside.

The second step is the image convolution with a filter, aiming at the enhancement of the contrast between focused and unfocused grains. The kernel of the filter is a

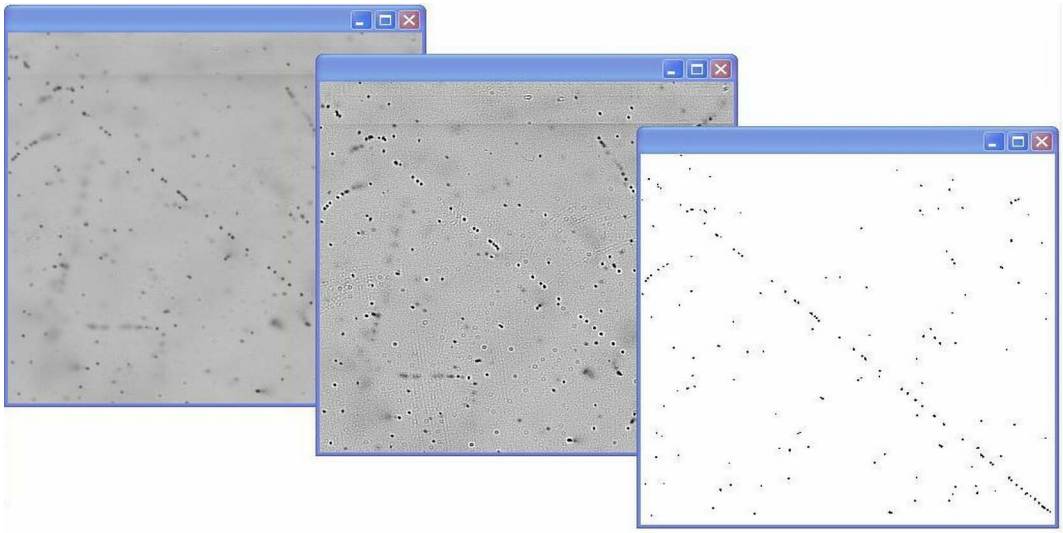

Fig. 5.6: Image processing: grabbed image, convolution and threshold.

6×6 matrix :

$$K = \begin{array}{|c|c|c|c|c|c|} \hline 1 & 1 & 1 & 1 & 1 & 1 \\ \hline 1 & 2 & 3 & 3 & 2 & 1 \\ \hline 1 & 3 & -13 & -13 & 3 & 1 \\ \hline 1 & 3 & -13 & -13 & 3 & 1 \\ \hline 1 & 2 & 3 & 3 & 2 & 1 \\ \hline 1 & 1 & 1 & 1 & 1 & 1 \\ \hline \end{array}$$

Convolution is a local operation: the output value of the pixel at a specific coordinate is a weighted sum of the input values of the neighbourhood pixels, the weights are given by the filter kernel. The convolution extends the original 255-values grey level scale to a wider one, making flat the shape of the background.

After the convolution a well-chosen threshold is applied and the data are binarised: pixels with values that exceeds the threshold are classified as *black*, the remaining ones as *white*. The chosen kernel and threshold define the vertical resolution of the apparatus. In the Fig. 5.6 the results of the three processes are shown.

In order to have a homogeneous clusters distribution inside the grabbed frames, an equalization procedure is performed. It consists in defining several cells, scanning an emulsion surface and counting the total number of detected clusters in each cell

with different applied thresholds. In order to have a constant number of clusters in each cell, a threshold map has to be used instead of a unique threshold value. The uniformity of the map reflects the uniformity of the illumination of the field of view and of the camera sensor response.

The last step of image processing is the clustering. The image is scanned row by row and the algorithm looks for black sequences inside each row. After a row has been scanned, the sequences are compared with all the sequence in the previous row and adjacent sequences are merged into a cluster. If two or more clusters come in contact, they are also merged. A cut on the cluster area helps to discard background due to the noise in the camera signal.

Finally, the cluster centre of gravity is calculated and position, area and shape are stored in the output file.

5.3.2 Tracking

Before track reconstruction, a cut on cluster areas is applied (area > 4 pixel) in order to eliminate background clusters. The remaining clusters are grain candidates.

The tracking consists of two main algorithms: track recognition and track fitting. In the first phase, the algorithm recognizes an array of grains as a track with geometrical alignments, the track fitting algorithm performs a linear fit of the position of the clusters and evaluates track slopes. Intercepts are given on the surface between emulsion and base.

The track recognition algorithm is the most important part of the tracking because this is the main source of inefficiency in tracks measurements. The first operation is the search for a *track start-up* on some *trigger layers*. In order to reduce the CPU time, the field of view is divided in cells, whose linear dimension is about 25 μm, and the start-up is searched only inside the same cells. The sequence of layers defined as a "trigger" is formed by two distant layers and a list of central layers (up to eight). For a given cell and a given sequence, all the clusters in the first two layers are connected with a line and other aligned clusters are searched in one of the

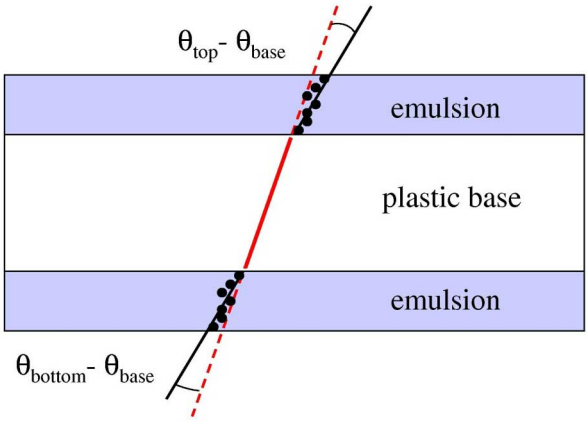

Fig. 5.7: Two micro-tracks connected through the base. The base-track is defined by joining the micro-track points closest to the plastic base.

inner layers within some tolerances. If at least one other cluster is found, a trigger is produced.

In order to limit the processing time, the algorithm fixed a maximum number of trials, so it becomes crucial to optimize them. When a start-up is found, the tracks are followed in all the other layers. Also the neighbouring cells are considered for track following, in order to increase the angular acceptance.

Once all clusters have been found, a bidimensional linear fit is performed and spurious clusters are removed from the tracks. If the number of grains that form the track is greater than a minimum number (e.g. six), the track is saved in the output file.

5.3.3 Data quality

The two segments of a track that pass through an emulsion sheet are reconstructed independently on the two sides of the emulsion layers and are called *micro-tracks*. In order to evaluate the micro-track angular resolution, the track along the base has to be reconstructed (*base-track*).

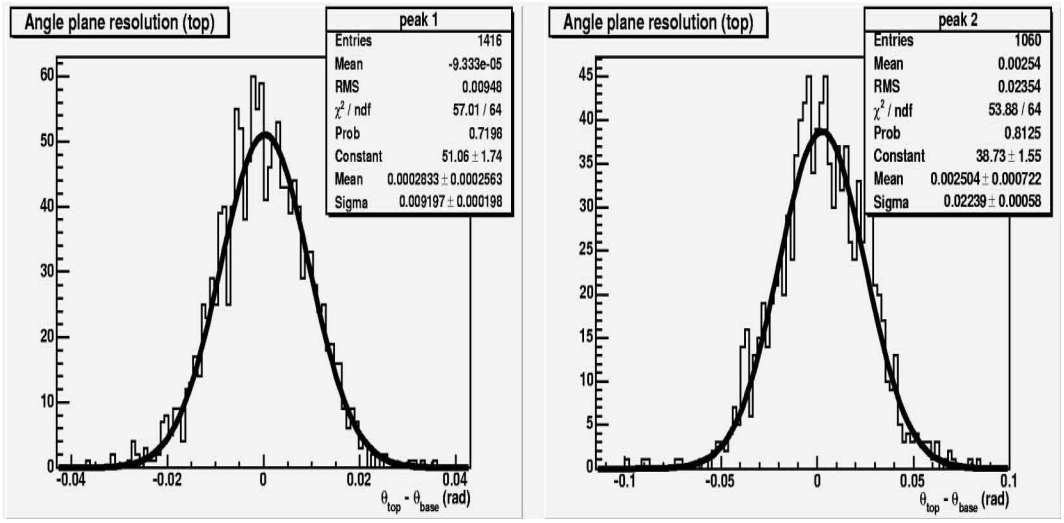

Fig. 5.8: The angular resolution of micro-tracks measured in the top side and connected on the bottom side of the emulsion film. It is evaluated by comparing with base-track angles (Fig. 5.7). Left: micro-track resolution at 0 mrad. Right: micro-track resolution at 400 mrad.

The base-track is defined by joining the micro-track points closest to the plastic base (Fig. 5.7). Since these points lie in regions unaffected by distortion effects, the base-track has an angular resolution approximately one order of magnitude better than the micro-tracks. Thus the angular difference between micro-tracks and base-track will provide an estimate of the micro-track angular resolution. Fig. 5.8 shows the resolutions for angles $\theta = 0$ and $\theta = 0.4$ rad. The micro-track angular resolutions are respectively 9 mrad and 22 mrad. With a good approximation, for both X and Y projections, the angular resolution can be expressed by the empirical equation:

$$\sigma(\theta) = \sigma(0)(1 + 4\theta) \tag{5.1}$$

where $\sigma(0)$ is the angular resolution for $\theta = 0$.

5.4 The off-line track processing

For each emulsion layer the positions and angles of the detected tracks are recorded as micro-tracks and are connected off-line to form base-tracks, whose positions and angles are not affected by distortion. After collecting these base-tracks in a series of emulsion films, all the films are aligned and track reconstruction (i.e. connecting between films) is performed.

The off-line reconstruction tool used for the following analysis is FEDRA (Framework for Emulsion Data Reconstruction and Analysis), an object-oriented tool based on C++ language developed in Root framework [62].

5.4.1 Base-track reconstruction

The base-track reconstruction is performed by projecting micro-track pairs across the plastic base and searching for an agreement within given slope and position tolerances. For each couple of micro-tracks that satisfy position and angular cuts, a χ^2 is calculated as

$$\chi^2 = \frac{1}{4}\left[\frac{(\theta_{xt}-\theta_{xB})^2}{\sigma_x} + \frac{(\theta_{xb}-\theta_{xB})^2}{\sigma_x} + \frac{(\theta_{yt}-\theta_{yB})^2}{\sigma_y} + \frac{(\theta_{yb}-\theta_{yB})^2}{\sigma_y}\right] \tag{5.2}$$

where $\theta_{xt(b)}$ and $\theta_{yt(b)}$ are the projections of the top (t) and bottom (b) micro-track angles in the $z-x$ plane and $z-y$ plane, θ_{xB} and θ_{yB} are the same projections for the base-tracks (B) and σ_x and σ_y are the micro-tracks angular resolutions, as defined in Sect. (5.3.3).

If a micro-track in the top side of the emulsion layer is linked with more than one micro-track in the bottom side, the base-track with the smaller χ^2 is selected.

5.4.2 Emulsion plate intercalibration

The emulsion plate intercalibration is done by subdividing the scanned area in several cells and performing, for each cell, a pattern recognition between base-tracks

of two consecutive emulsion films. One of the two pattern is fixed and the other is shifted several times, the translation which have the maximum number of track coincidences is chosen.

After this procedure, the algorithm connects base-tracks of the two plates, and with this sample of tracks the affine transformation if calculated as:

$$\begin{pmatrix} x' \\ y' \end{pmatrix} = \begin{pmatrix} a_{11} & a_{12} \\ a_{21} & a_{22} \end{pmatrix} \begin{pmatrix} x \\ y \end{pmatrix} + \begin{pmatrix} b_1 \\ b_2 \end{pmatrix} \tag{5.3}$$

The alignment is better performed on a local basis, by using base-tracks in a limited surface of the emulsion films. In this way it is possible to eliminate the effect of global deformation of the films.

In order to achieve a precise alignment between two consecutive plates, it is crucial to have a sufficient number of penetrating tracks. The required track density for alignment is about 1-2 tracks/mm^2,

The cosmic ray and the neutrino fluxes to which the experiment is exposed are very low and the induced track density in the emulsion is not high enough for the alignment within a few μm. Nevertheless, this is an essential requirement for the momentum measurement in an ECC brick. One needs, therefore, to expose the selected bricks to high momentum cosmic rays as reference tracks for the precise film alignment. For this purpose, a dedicated pit has been excavated at the external site of the LNGS, suitably shielded by an iron cover for the suppression of the electromagnetic component of cosmic rays [63].

Once all plates are aligned, the track reconstruction algorithm follows all the measured base-tracks of an emulsion film to the upstream and downstream ones. A number of connected base-tracks, not necessarily adjacent) forms a *volume-track*.

5.5 Performances of the Bologna scanning system

From 2002, when the first prototype was installed in the Bologna Laboratory, a large effort was made to improve the stability of the system, to understand possible

sources of inefficiencies and to increase the purity in order to fit the requirements of the experiment.

The system reached its final configuration in summer 2004 and became suitable for physics measurements.

In this section I will present the performances of the Bologna system in its final configuration, in terms of angular resolutions, efficiency and purity. This result was obtained from the track reconstruction in seven consecutive emulsions (without lead in between) exposed at the CERN-PS.

5.5.1 Test beam exposure

The test beam exposure was performed in June 2004 at the CERN PS-T7 beam line. We used a 10 GeV pion beam defocused on a total surface of about $\sim 10 \times 10$ cm^2 with a small electron contamination ($\sim 1\%$) and a small muon contamination (about 10% or less). We exposed 1 brick with 64 emulsions (without lead) at high intensity (2 particles/mm^2/angle position).

The brick was tilted by 14 different angles (7 angles on one projection times 2 angles on the other one) in order to study the angular dependence of the system performance. The 7 angles on X projection are 0. 100. -200. 300. -400. 500. -600. (mrad) the 2 angles on Y projection are 0. 200. (mrad) Tab. 5.2 reports the number of events for each angles as measured with electronic detectors during the exposures.

5.5.2 Track analysis

Since the beam was uniformly distributed on the emulsion surface, for each angular exposure, a wide-angle scanning of about 5 cm^2 was performed at the centre of each emulsion plates. In Fig. 5.9 the angular distribution of the base-tracks reconstructed in the upstream plate is shown.

Using the base-tracks χ^2 defined in Eq. 5.2 and the number of clusters associated to the linked micro-tracks, two populations emerge from the sample (Fig. 5.10). A quality cut is defined to reject base-tracks with large χ^2 and small number of

θ_x (mrad)	θ_y (mrad)	Scintillator counters
0	0	20073
100	0	20885
300	0	21323
500	0	20954
-200	0	21296
-400	0	21565
-600	0	21473
0	200	21335
100	200	21208
300	200	21134
500	200	21466
-200	200	21398
-400	200	21431
-600	200	21358

Tab. 5.2: Scintillator triggers during the exposures.

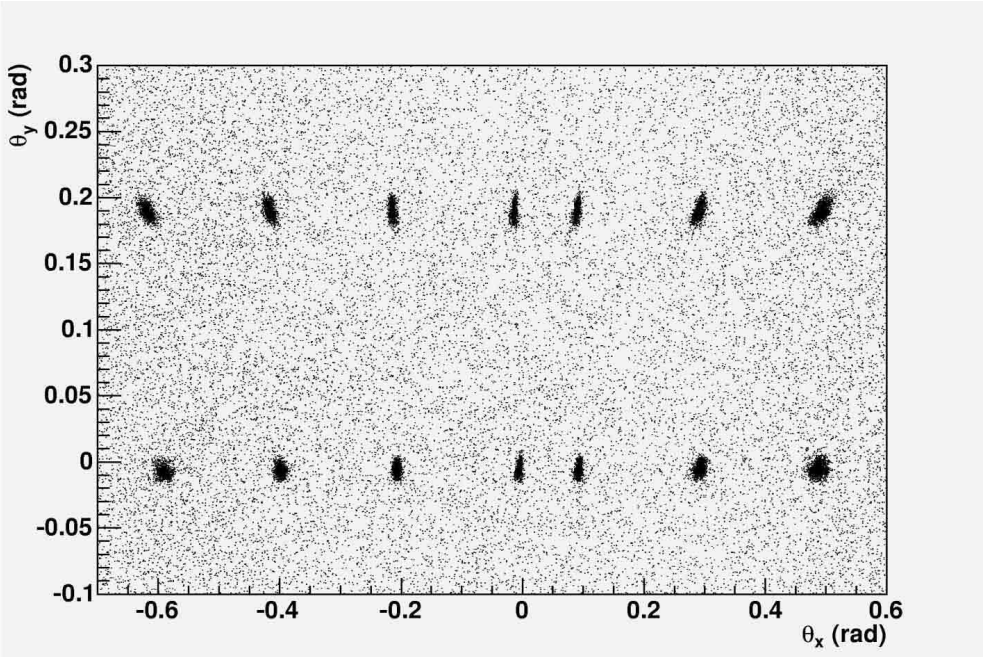

Fig. 5.9: Base-tracks angle distribution in the two projections $y - z$ and $x - z$ as reconstructed in the upstream plate of the stack.

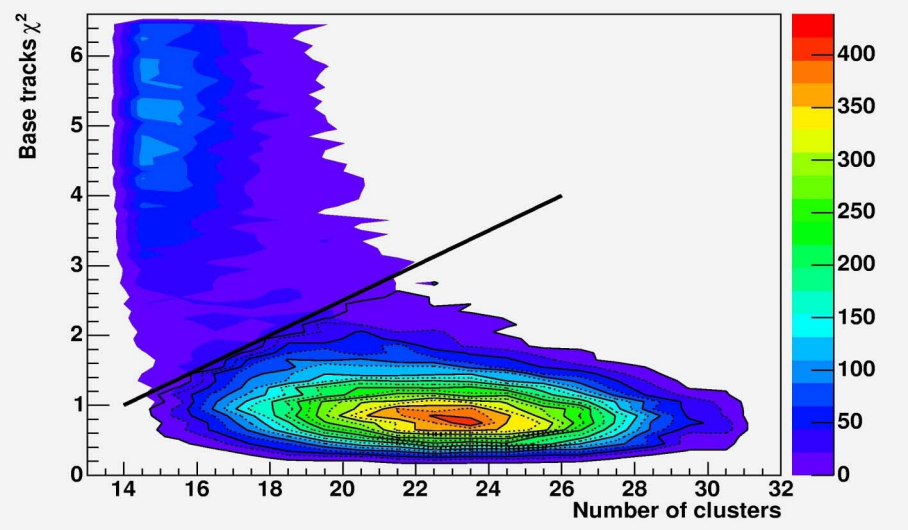

Fig. 5.10: Base-tracks χ^2 distribution as a function of the total number of the clusters that form the two linked micro-tracks. The quality cut line is also shown; base-tracks above the line are rejected.

associated clusters (*fake* tracks):

$$\chi^2 \leq 0.25 \cdot PH - 2.5 \tag{5.4}$$

Where PH id the total number of clusters associated to the base-tracks.

This cut was applied to all the base-tracks of the scanned plates, and volume tracks have been reconstructed.

By considering only tracks measured in all the plates, base-tracks angular and position residuals have been calculated with respect to the fitted volume tracks. These residuals are dependent on measured angles and range from 1.6 to 7 mrad (Fig. 5.11). The corresponding position resolution ranges from 0.9 to 2.5 μm (Fig. 5.12). Note that position residuals is composed of both measurement and alignment errors unlike the angular residuals. Considering that the distance between two consecutive plates is 300 μm, the position residuals from the angular errors is $\sigma_{pos} = \sigma_{angle} \times 300$. In this way it is possible to evaluate the alignment precision which is about 0.4 μm.

However, this is not the ultimate performance. As discussed in Sect. 4.3, in

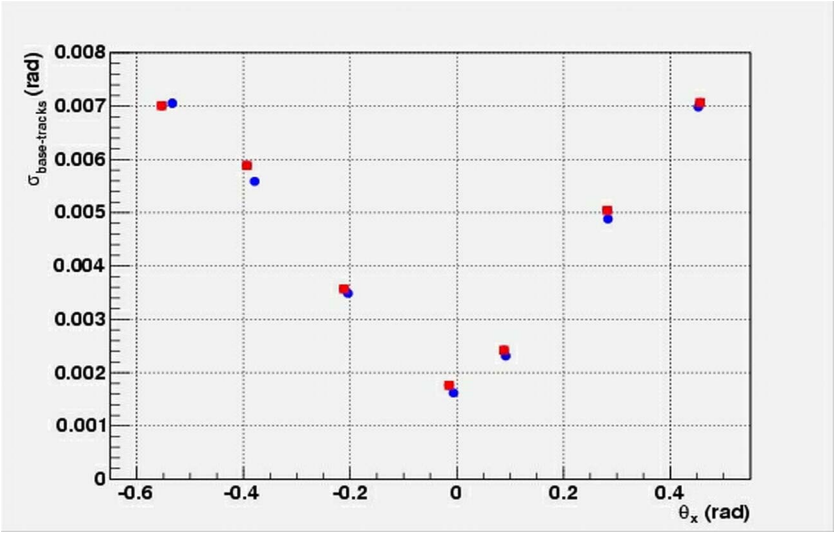

Fig. 5.11: The angular resolution of base-tracks as a function of θ_x. It is evaluated by comparing base-track angles with respect to the volume-track angles. The blue circles correspond to the $\theta_y \sim 200$ mrad and red squares to a measured $\theta_y \sim 0$ mrad

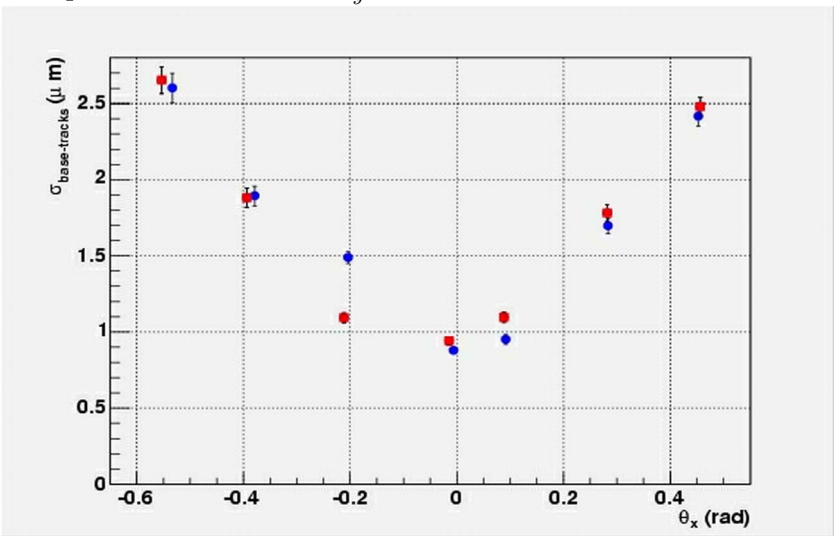

Fig. 5.12: The position resolution of base-tracks. Note that position residuals are composed of both measurement and alignment errors unlike the angular residuals. The alignment error is at the level of 0.4 μm.

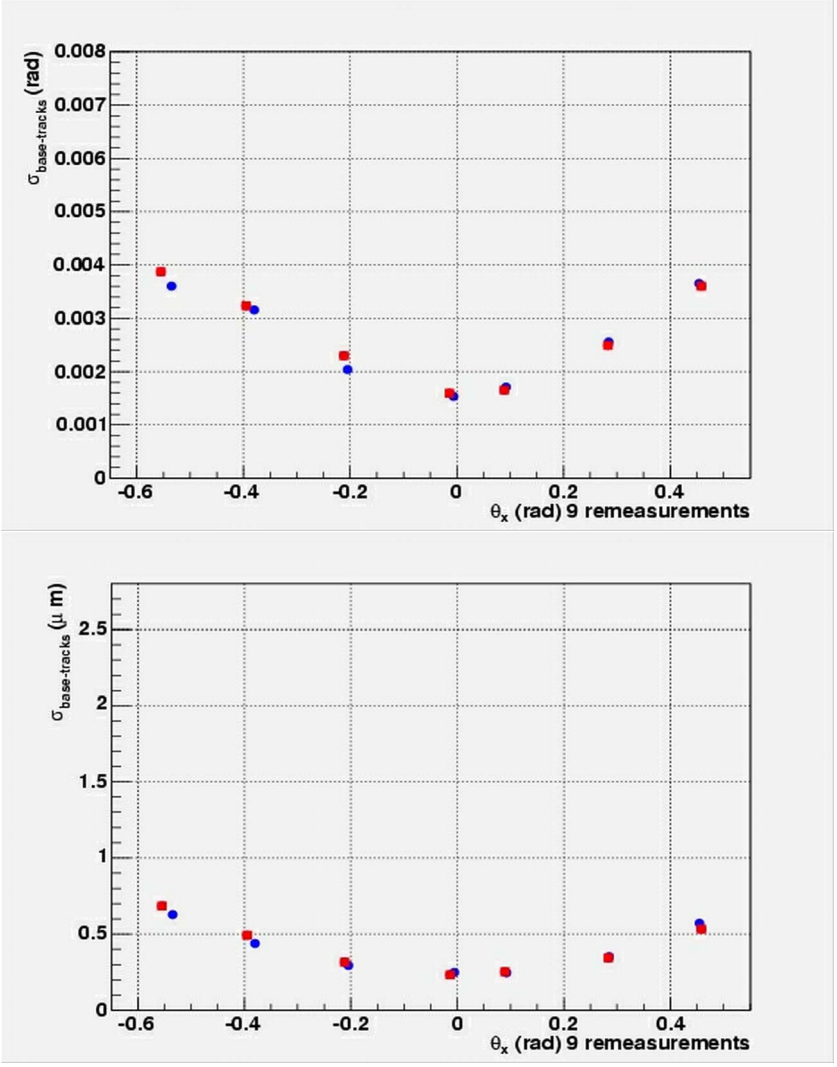

Fig. 5.13: The angular (up) and position (down) resolutions of base-tracks obtained by computing the mean angle from nine independent measurements of an emulsion film.

OPERA emulsion films, a *mip* produces about 32 grains/100 μm along its trajectory. The intrinsic resolution limit using these grains is 0.06 μm. The large difference with the achieved resolution is due to the digitisation accuracy in the camera readout, in the stage coordinate measurements and in the vertical resolution.

High accuracy measurements, aiming to measure special events or to perform the final selection of τ decays, can be performed by means of dedicated high accuracy microscope stages and/or by multiple position measurements, to achieve the intrinsic resolution of the emulsion film. An example illustrating the improvement obtained by multiple position measurements is given by scanning the same area of one emulsion sheet several times independently. By averaging over nine measurements, the angle and position errors are calculated as the residual of one measurement with respect to the mean value. Results are given in Fig 5.13.

5.5.3 Efficiency and background estimate

During exposure emulsion sheets accumulate significant quantities of background due to cosmic rays and environmental radioactivity. While some tracks can be removed off-line with the quality cut, many cosmic ray tracks can be mistakenly identified as beam-related tracks.

In order to minimize the number of base-tracks not related to the pion beam, efficiencies have been evaluated taking into account volume-tracks with at least six (not necessary adjacent) base-tracks and with a reconstructed angle within 3 sigma of the beam directions. The base-track finding efficiency is then defined:

$$\epsilon_{tracking} = \frac{\text{Number of measured base-tracks}}{\text{Number of base-tracks searched for}} \tag{5.5}$$

where the number of base-tracks searched for is given by the number of the volume-track sample times the number of scanned plates.

The base-track tracking efficiency have been calculated separately for each beam direction with respect to the optical axis; the result is shown in Fig. 5.14. The mean efficiency is greater than 90% and corresponds to a micro-track finding efficiency of about 95%. The shape of this curve is due to the number of clusters associated to base-tracks. As it is shown in Fig. 5.15, the number of clusters have a minimum between 200 and 300 mrad and, from $\theta > 300$ mrad, increase with the slope *theta*. Base-tracks with a slope close to zero have more clusters due to the reinforcement

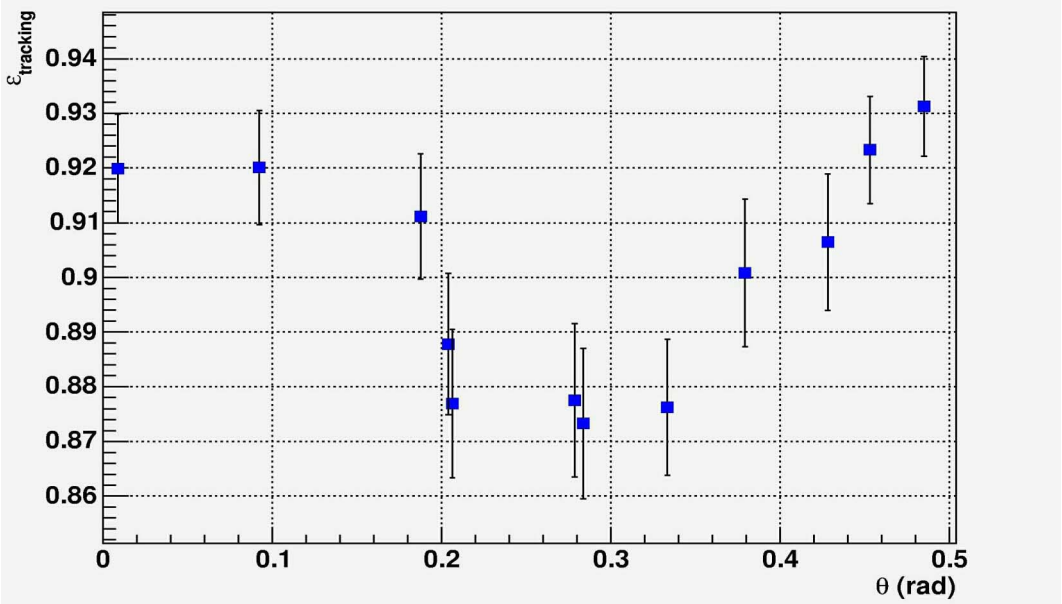

Fig. 5.14: Base-track finding efficiency as a function of the reconstructed volume angle θ.

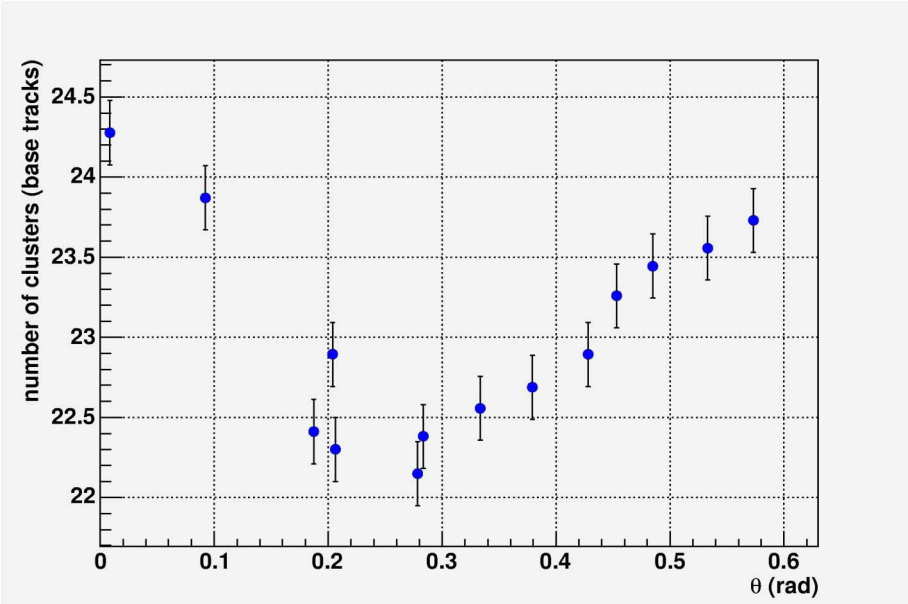

Fig. 5.15: Average number of clusters in a base-track as a function of its measured angle.

of grains with their shadows.

The background measurement was made using a non exposed emulsion plate from the same batch production as the others, refreshed and developed at the same time. The scanning was done with the same on-line parameters, and the same quality cut were applied (Fig. 5.16). The number of base-tracks not related to the beam is about $400/\text{cm}^2/\,|\theta| < 0.4$ rad.

While most of them are cosmic ray tracks, some tracks can be random coincidences of two micro-tracks generated by aligned fog grains. In order to separate cosmic ray background from instrumental background, we manually inspected 405 base-tracks (measured in 1 cm^2 with $|\theta| < 0.4$ rad). Defining *fake* track, a base-track with one of both micro-tracks generated by aligned fog, only 2 base-tracks have been classified as fake. The instrumental background is then $2/\text{cm}^2/\,|\theta| < 0.4$ rad.

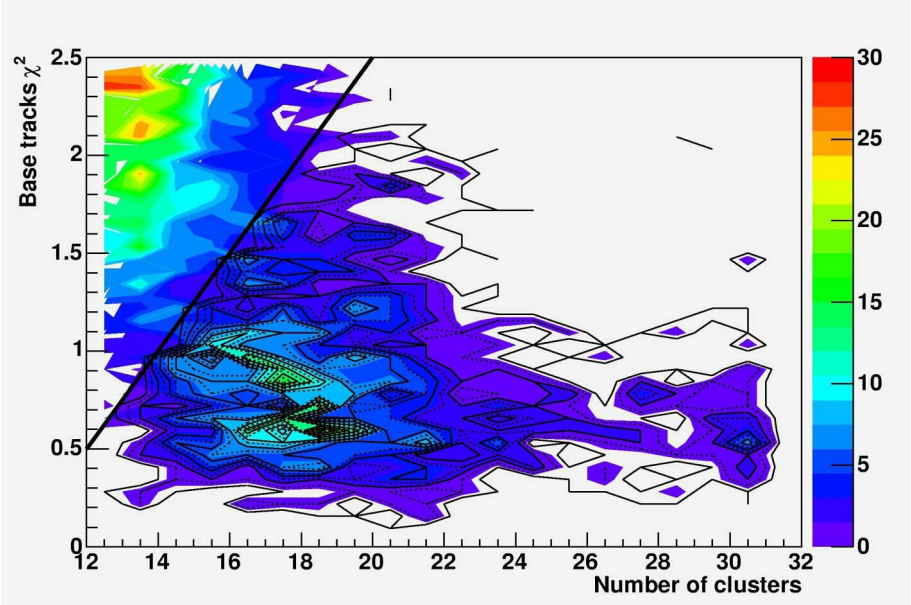

Fig. 5.16: The χ^2 distribution as a function of clusters for base-tracks measured in a non-exposed emulsion plate. The quality cut, as defined in Eq. 5.4, is indicated by the line.

5.6 Conclusions

The goal of 20 cm^2/h scanning speed was achieved with a track reconstruction efficiency of 96% for micro-tracks with $\theta < 200$ mrad and more than 94% for micro-tracks with $\theta > 200$ mrad. The instrumental background is about 2 base-tracks per cm^2. This result fulfil the requests of the experiment for the emulsion general scan.

The achieved base-track angular resolution and the sub-micrometric plate-to-plate alignment allow the analysis of pion-electron identification based, as fully described in the next chapter, on the multiple Coulomb scattering of charged particles in ECC bricks.

Chapter 6

Pion-electron identification in the OPERA ECC bricks

6.1 Introduction

The experimental program of the OPERA experiment requires a good pion/electron separation capability. In particular, it is important to reduce as much as possible the wrong identification of other particles with electrons. Charged hadrons, mainly pions, may be misidentified as electrons since they can undergo charge exchange processes and mimic the development of an e.m. shower. The overall performances of the experiment rely on the exact values of these identification probabilities which, up to now, have been estimated with Monte Carlo simulations or with analyses strongly based on simulations.

The main cases suffering from a wrong electron-pion identification are reported. In the case of pions mis-identified as electrons:

- **Loss of efficiency for tau decays.** In a ν_τCC interaction, if a hadron in the primary vertex is misidentified as an electron, the whole event is promptly classified as a ν_eCC interaction and discarded, even if a kink topology is detected (Fig.6.1). This source of inefficiency affects all tau decay channels.
- **Background for $\tau \rightarrow e$ channel.** If in a ν_μ NC interaction or in a ν_μ

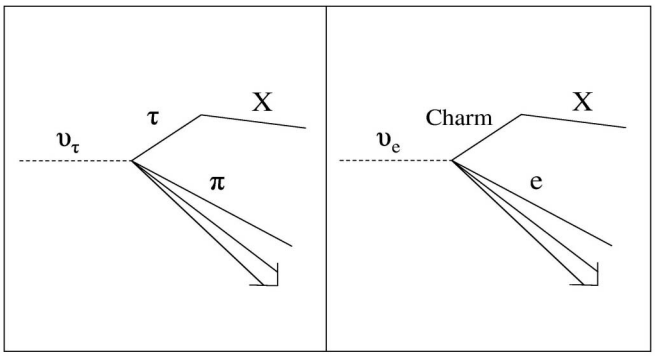

Fig. 6.1: Inefficiency of τ decays. Left: a τ decays in one of the three channels (electronic, muonic or hadronic). Right: wrong interpretation if the pion is mis-identified as an electron. The arrow in the plot represents all other charged tracks escaping from the vertex.

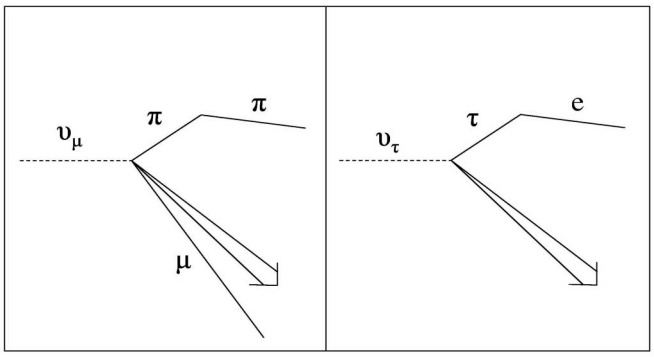

Fig. 6.2: Background for ν_τ detection. Left: in a ν_μNC interaction or in a ν_μCC interaction with the muon unidentified, a pion suffers a large angle scattering. Right: wrong reconstruction if the pion is mis-identified as an electron.

CC interaction with the muon escaping unidentified, one pion suffers a large angle hadronic interaction and it is misidentified as an electron, the event is recognised as a $\tau \rightarrow e$ decay (Fig. 6.2). These events cannot be easily removed with the usual p_t cut since, if the track is identified as an electron, this cut is set at $p_t > 100$ MeV/c, to be compared with $p_t > 600$ MeV/c for hadrons.

- **Background for $\nu_\mu \rightarrow \nu_e$ channel.** If in a ν_μ NC interaction or in a ν_μ

CC interaction with the muon escaping unidentified, one of the pions at the primary vertex is misidentified as an electron, the event is recognised as a ν_e CC interaction.

In the case of electrons mis-identified as pions:

- **Loss of efficiency for the $\tau \to e$ channel.** If the electron daughter of the tau is mis-identified as a pion, and $p_t < 600$ MeV/c, the event is rejected.
- **Loss of efficiency for the $\nu_\mu \to \nu_e$ oscillation channel.** If the electron in the primary vertex is mis-identified as a pion, the event is rejected.

A good electron-pion separation can be achieved by studying the different behaviour of these particles in passing through an OPERA brick. At the energies of our interest ($1 \div 10$ GeV) an electron loses energy essentially through bremsstrahlung processes; charged pions, on the other hand, mainly undergo ionization losses. The energy is practically constant for pions while it is strongly decreasing for electrons in traversing the brick. As will be shown in the following, this property will be used to construct a χ^2-based separator for these two categories.

An experimental study of electron-pion identification using ECCs was performed in 2001 with a test at an electron-enriched π^- beam. The electron identification efficiency was estimated to be about 90% [64]. The key point of this analysis was the measured e/π ratio of the beam, performed by a Cherenkov counter installed upstream of the ECC target. The final efficiencies were obtained unfolding the measured ones using a Monte Carlo simulation of pure electron and pion beams.

The main goal of the work presented in this thesis is to provide a measurement of pion-electron identification efficiency with an algorithm based on MCS in cleaner experimental conditions. This goal has been achieved performing pion exposures with a negligible electron contamination. The test was made in June 2003 at the CERN PS-T7 beam line with a pion beam of 2, 4 and 6 GeV/c and was complemented with a pure electron exposure at the DESY Lab., in the same energy range [2].

The same ECC bricks have been analysed with an algorithm based on a neural network in order to identify electrons on the basis of the shower analysis. Results are described in Ref. [2].

6.2 Passage of particles through an OPERA ECC brick

In general, two main features characterize the passage of charged particles through matter: a degradation of the particle energy and a deflection of the particle from its incident direction. These effects are primarily the result of two processes:

- inelastic collisions with the atomic electrons of the material;
- elastic scattering from nuclei.

These reactions occur many times per unit path length in matter and it is their cumulative result which accounts for the two principal effects observed. These, however, are by no means the only reactions which can occur. Other processes include:

- bremsstrahlung and pair production.
- emission of Cherenkov radiation,
- nuclear reactions,

6.2.1 Energy loss of heavy charged particles

Of the two electromagnetic processes, the inelastic collisions are almost solely responsible for the energy loss of heavy particles (i.e., heavier than the electron) in matter. In these collisions energy is transferred from the particle to the atom causing an ionization or excitation of the latter. The amount transferred in each collision is generally a very small fraction of the particle total kinetic energy; however, in

normally dense matter, the number of collisions per unit path length is so large, that a substantial cumulative energy loss is observed even in relatively thin layers of material.

Elastic scattering from nuclei also occurs frequently although not as often as electron collisions. In general very little energy is transferred in these collisions since the masses of the nuclei of most materials are usually large compared to the incident particle mass.

The specific energy loss of heavy charged particles, caused by collisions of the impinging particle with atomic electrons, is given by the Bethe-Bloch formula:

$$-\frac{dE}{dx} = 2\pi N_a r_e^2 m_e c^2 \rho \frac{Z}{A}\frac{z^2}{\beta^2}\left[\ln\left(\frac{2m_e\gamma^2 v^2 W_{max}}{I^2}\right) - 2\beta^2\right] \tag{6.1}$$

where N_a is Avogadro's number, r_e is the classical electron radius, ρ is the mass density of the medium, I is the mean excitation energy and W_{max} is the maximum kinetic energy which can be imparted to a free electron in a single collision. An example of the energy dependence of dE/dx is shown in Fig. 6.3 where the function has been computed for pions on some materials, including lead.

The energy loss of hadrons, after passing through a material of thickness x, is

$$E(x) = E_0(1 - \frac{dE}{dx}x) \tag{6.2}$$

If the initial momentum is between 1 to 10 GeV, the average energy can be consider almost constant.

6.2.2 Energy loss of electrons and positrons

Like heavy charged particles, electrons and positrons also suffer a collisional energy loss when passing through matter. However, because of their small mass, an additional energy mechanism comes into play: the emission of electromagnetic radiation arising from scattering in the electric field of a nucleus (*bremsstrahlung*). This process is negligible at energies of a few MeV or less, however, as the energy

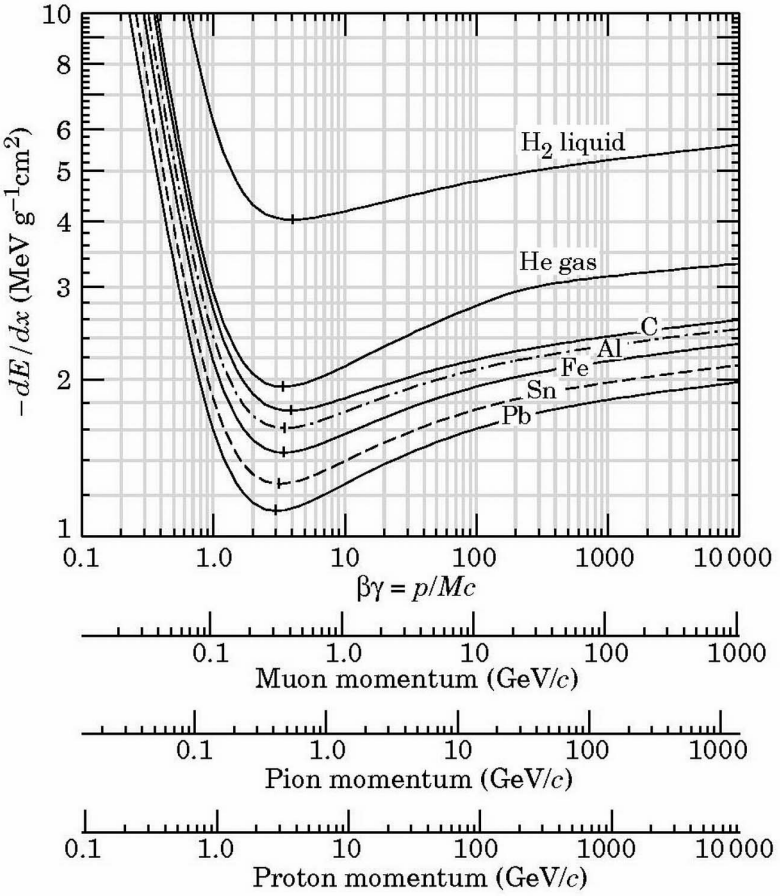

Fig. 6.3: Specific energy loss due to ionization in liquid (bubble chamber) hydrogen, gaseous helium, carbon, aluminium, tin, and lead.

increases, the energy loss by bremsstrahlung is greater than the collision-ionization loss , as it can be seen in the Fig. 6.4 where the energy loss is computed on copper.

The energy loss due to radiation is:

$$-\left(\frac{dE}{dx}\right)_{rad} = NE_0\Phi_{rad} \tag{6.3}$$

with N = number of atoms/cm^3, E_0 = initial energy and

$$\Phi_{rad} = 4Z^2 r_e^2 \alpha \left[\ln\left(183Z^{-1/3}\right) + \frac{1}{18} - f(Z)\right] \tag{6.4}$$

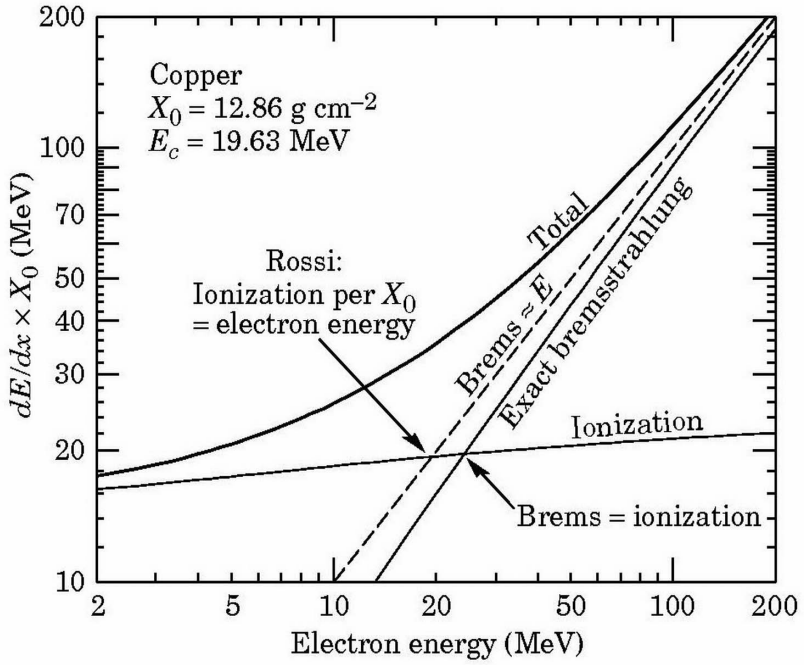

Fig. 6.4: Radiation and collision energy loss for electrons in copper as a function of the electron energy. Two definitions of critical energy are given.

Considering the high energy limit where collision loss can be ignored relative to radiation loss, Φ_{rad} is independent of E, so that

$$E = E_0 \exp\left(-\frac{x}{X_0}\right) \tag{6.5}$$

where x is the distance travelled and $L_0 = 1/N\Phi_{rad}$ is the *radiation length.*

For compounds and mixtures, the radiation lengths may be computed by applying Bragg's rule.

$$\frac{1}{X_0} = \sum \frac{w_j}{X_{0j}} \tag{6.6}$$

where w_j and X_{0j} are the fraction by weight and the radiation length for the jth element.

6.3 Multiple Coulomb scattering at small angles

In addition to inelastic collisions with the atomic electrons, charged particles passing through matter also suffer repeated elastic Coulomb scatterings from nuclei and are deflected by many small-angle scatters. The Coulomb scattering distribution at small angles is well represented by the theory of Moliere [65].

If we ignore the small probability of large-angle single scattering, the probability distribution is approximately Gaussian in form,

$$P(\Theta)d\Omega \approx \frac{2\Theta}{\langle\Theta^2\rangle}\exp\left(\frac{-\Theta^2}{\langle\Theta^2\rangle}\right)d\Theta \tag{6.7}$$

The parameter $\langle\Theta^2\rangle$ represents the mean squared scattering angle. The squared root $\Theta_0 = \sqrt{\langle\Theta^2\rangle}$ is know as the RMS scattering angle and should be equal to the RMS scattering angle of the full multiple scattering angle distribution.

An estimate of Θ_0 is obtained by using an empirical formula [66] which is valid to within 5% for $Z > 20$ and for target thicknesses x between $10^{-3}X_0$ and $10X_0$,

$$\Theta_0 = \frac{13.6\text{MeV/c}}{\beta p}z\sqrt{\frac{x}{X_0}}\left[1 + 0.038\ln\left(\frac{x}{X_0}\right)\right] \tag{6.8}$$

with X_0 = radiation length of material; x = thickness of material; p = momentum of the particle; z = charge of particle (Θ_0 is in radians).

A useful quantity is the angular deflection projected onto a perpendicular plane containing the incident trajectory. The projected distribution is also approximately Gaussian and the mean squared projected scattering angle $\langle\Theta_x^2\rangle$ is related to the space scattering angle by

$$\left\langle\Theta_x^2\right\rangle = \left\langle\Theta^2\right\rangle/2 \tag{6.9}$$

Eq. 6.8 describes scattering from a single material, while the usual problem involves the multiple scattering of a particle traversing many different layers and mixtures. Since it is from a fit to a Moliere distribution, it is incorrect to add the individual θ_0 contributions in quadrature; the result is systematically too small. It is much more accurate to apply Eq. 6.8 once, after finding x and X_0 for the combined scattered.

Taking into account the radiation length of lead, of the plastic base and of the emulsion together with their fraction of weight in an ECC cell, the combined X_0 is equal to 5.81 mm.

6.4 The pion test beam at CERN

The test beam exposures have been performed in June 2003 at the CERN PS-T7 beam line. The CERN PS East Area beams are derived from the primary proton beam with momentum of 24 GeV/c, ejected from the PS. The primary beam is split in two branches which feed two production targets, sources of four secondary beams. The north target is the source of the three secondary beams T9, T10 and T11, the south target is the source of the T7 beam.

The four beams are designed in order to provide the users with non-separated secondary particles having a well defined momentum (with a resolution of the order of 1%). The polarity, momentum, and intensity may be adjusted inside a large range up to the nominal values. Each beam consists of two focusing stages:

- the first one (two quadrupoles and a bending magnet) performs the momentum analysis at a variable-aperture horizontal collimator (MCH01, "momentum slit"). A vertical collimator MCV01 may be used to adjust the beam intensity.

- the second one performs the momentum recombination (use of a "field lens") and refocuses the beam into the experimental area.

The final focus may be moved along the beam line by changing the currents in the last quadrupole doublet; steering dipoles are available in order to adjust the beam position (horizontal and vertical). Secondary beams have typical intensities of the order of 10^6 particles per spill of about 300 ms and per channel. The maximum design momentum for the T7 beam is 10 GeV/c and the theoretical momentum resolution is 0.7%.

6.4.1 Experimental set-up

The electronic setup for the beam monitoring is shown in Fig. 6.5. Centered with respect the beam line there are a Cerenkov counter, two scintillator counters (SC1 and SC2), two multi-wire chambers (MW1 and MW2) and a lead glass.

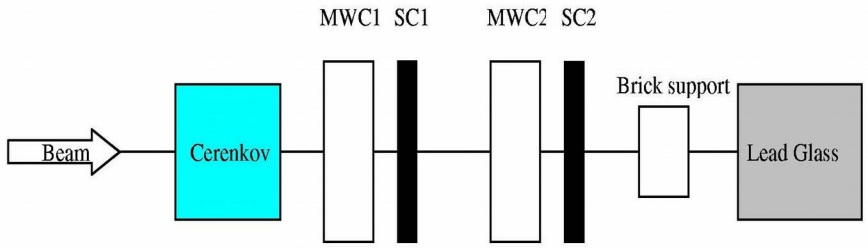

Fig. 6.5: The experimental set up of the beam line.

The two scintillation counters, with an active area of about 10×12 cm^2, are used in coincidence to provide the beam trigger signal. The two multi-wire chambers operate with a mixture of 50% Ar and 50% $C0_2$ and measure two perpendicular coordinates with a resolution of 300 microns. The chambers, mounted at a distance of 53 cm, have active areas of 12×12 cm^2 and have been used for beam monitoring. SC1, SC2, MW1 and MW2 and the ECC brick support have been mounted on a motorized table controlled remotely from the control room. By using the two multiwire chambers it was easy to centre the bricks with respect to the beam line. In Fig. 6.6 is shown the beam spot position measured with the multiwire chambers. The focused beam spot diameter was about 2 cm in the x and 1.5 cm in the y projections.

The Cherenkov counter installed on the PS-T7 area is a gas threshold counters filled with Helium. By changing the gas pressure, it is possible to change the threshold momentum for a given particle. In Fig. 6.7 the Helium threshold pressure is

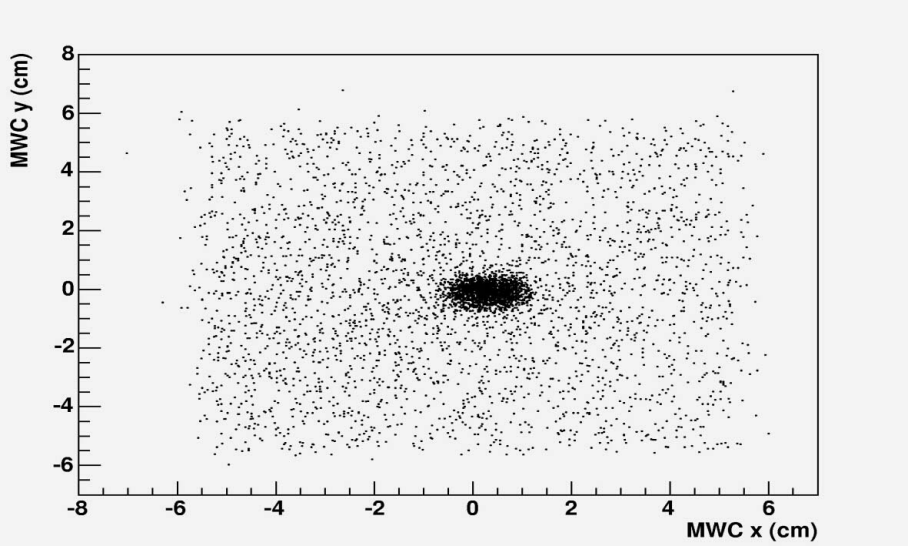

Fig. 6.6: The focused beam spot after the centring of all the electronic components.

shown as a function of pion and muon momentum. The lead glass have been used to monitor the electron contamination.

6.4.2 Electron and muon contamination

In order to perform an exposure with pion beams of 2, 4 and 6 GeV/c with negligible electron contamination, it was necessary to add a lead block (*pre-shower*) with a thickness of 2.5 cm ($\sim 4.5\ X_0$) before the ECC brick. The pre-shower was inserted after the last focusing magnet of the T7 beam line and before the Cherenkov counter (Fig. 6.8).

The electron contamination was monitored by using the combined information from the Cherenkov and the Lead Glass detectors. The Cherenkov pressure was set at 2 atm and, therefore, pions with momentum lower than 12 GeV/c are under threshold (see Fig. 6.7). In this way, the only particles above threshold could be electrons and/or high energy muons (halo muons). Those particles have been selected and further analysed with the Lead Glass detector used to separate electrons from muons.

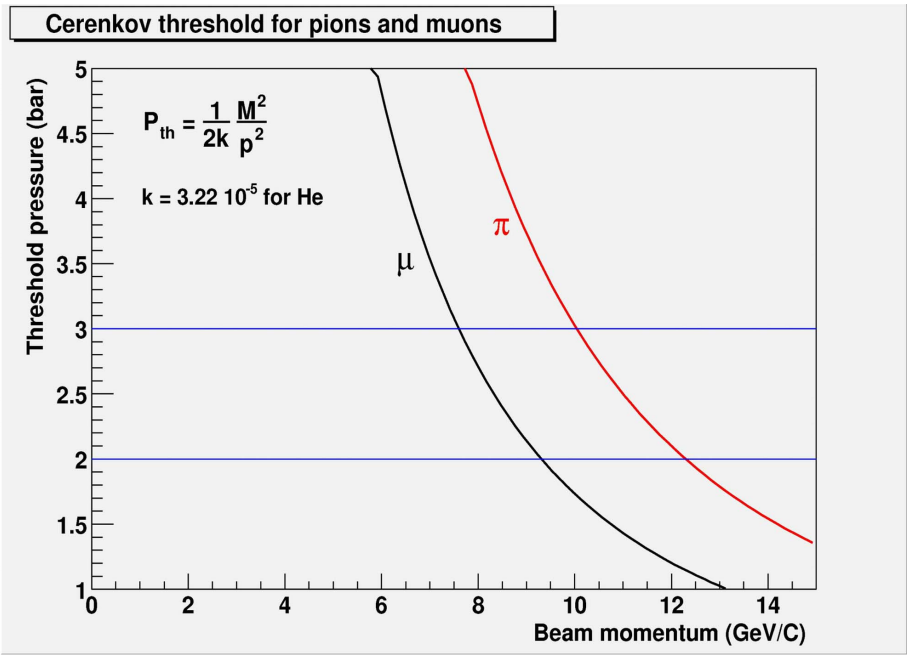

Fig. 6.7: Pressure threshold for the Cherenkov counter as a function of the momentum of a given particle. The curves for pions and muons were computed for the interested momentum range (electrons are, obviously, always above threshold).

Fig. 6.8: The pre-shower fixed in between the last focusing magnet and the Cherenkov counter during the exposures.

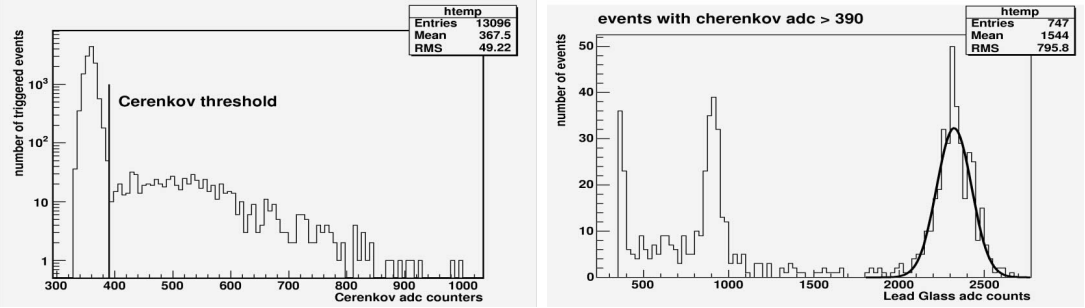

Fig. 6.9: Electron contamination before the pre-shower insertion. Left: Cerenkov ADC counts for all the triggered events. The under threshold signals are due to pions of 2 GeV/c, while the counts above threshold are muons and electrons. Right: Lead Glass ADC counts for events above threshold in the Cherenkov detector. The electron peak, at 2000-2500 lead glass ACD counts, is fitted to a gaussian distribution.

Fig. 6.9 (left panel) shows the Cherenkov ADC counts for the 2 GeV pion beam before the pre-shower insertion. Events above threshold (ADC counts > 390) have been analysed with the Lead Glass (Fig. 6.9, right panel). The electron signal clearly emerges (ADC counts > 1800) and the fitted gaussian peak provides a good estimate of the electron contamination (about 3%).

Inserting the pre-shower on the beam line, the electron contamination decreases to $\sim 0.6\%$, as shown in Fig. 6.10. For the 4 and 6 GeV pion beams, the electron contamination is less than 0.4%.

Also the muon contamination has to be evaluated, since the overall pion identification efficiency relies on the percentage of passing-through particles in the beam. A rough estimate of the muon contamination has been performed by comparing the number of triggers when the beam is on with the number of triggers when a 1.5 m brass beam stopper is inserted in the beam line (beam off). This gives a muon contamination of 4% at 2 GeV, 0.8% at 4 GeV and a negligible contamination at 6 GeV. However, it is clear that this method systematically underestimates the muon contamination since it neglects the muon enegy loss in the stopper. This is particularly important for the 2 GeV exposures since the muon energy loss through the stopper is 1.72 GeV and most muons are stopped. A better estimate has been

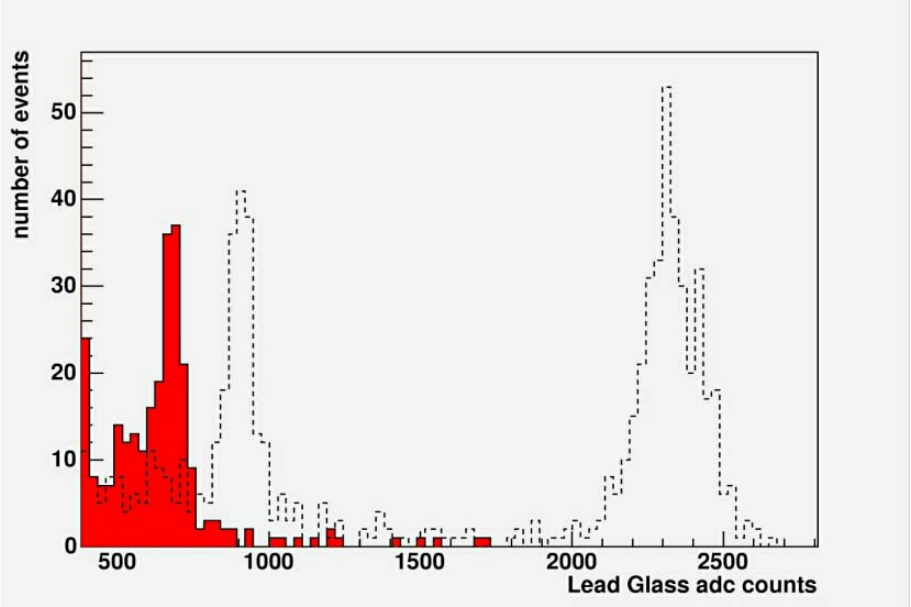

Fig. 6.10: Lead Glass ADC counts for 2 GeV pions after the pre-shower insertion (solid histogram). Inserting the pre-shower the electron signal is absent and the muon peak is shifted because of the muons energy loss in 2.5 cm of lead (pre-shower). For comparison the ADC counts without the pre-shower is also plotted (dashed histogram).

carried out by analysing passing through tracks in the ECC brick (see Sec. 6.7.1).

6.4.3 The beam

Adding the lead target, the beam is defocused without changing the currents in the last quadrupole doublet. The beam spot diameter was about 12 cm (Fig. 6.11) and the bricks could be uniformly exposed to the beam.

The beam was monitored at 2, 4 and 6 GeV/c with a collimator aperture of 7 mm in order to have a momentum resolution of about 1%.

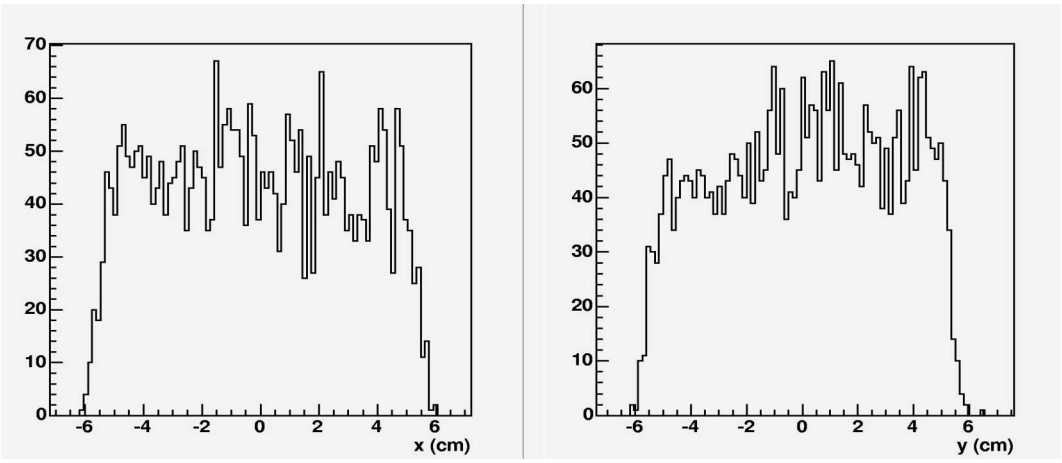

Fig. 6.11: Defocused beam spot, as measured by the most downstream multi-wire chamber.

6.4.4 Brick exposures

Three ECC bricks have been prepared with 56 emulsion sheets and 55 lead plates as an OPERA brick. All the emulsions have been refreshed for 3 days and the bricks exposed soon after the refreshing.

In order to have reasonable statistics, all the three bricks have been exposed with a density of about 2000 tracks/cm^2 with an incident angle of 50 mrad. Tab. 6.1 reports the number of triggered events for the three exposures.

Brick ID	momentum	Scintillation counters
1	4 GeV/c	65526
2	6 GeV/c	71420
3	2 GeV/c	68229

Tab. 6.1: Scintillator triggers during the three exposures.

6.5 ECC readout and first level reconstruction

The measurement of the ECC bricks was performed with the European Scanning System. Bricks exposed at 2 and 4 GeV were scanned in the Napoli Lab. and the

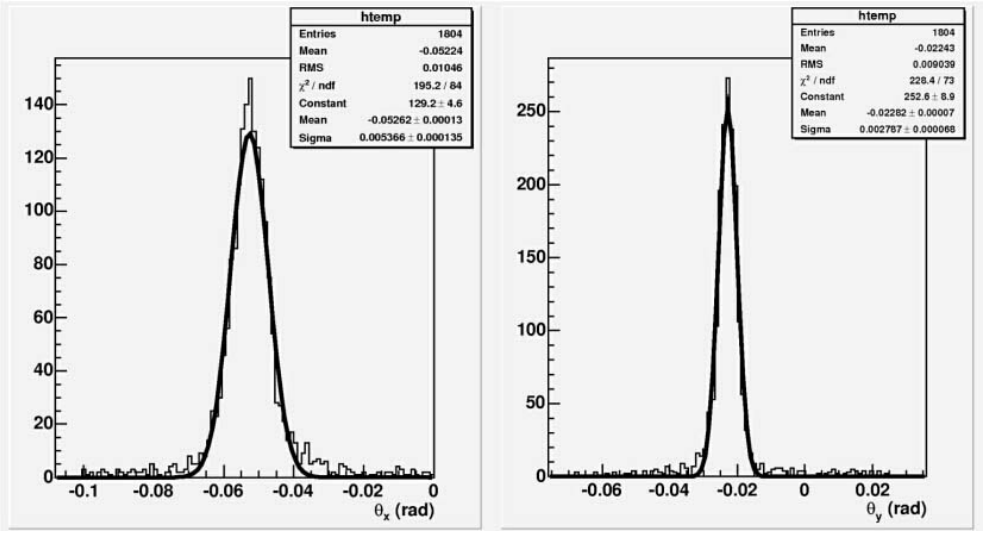

Fig. 6.12: Signal tracks angular distribution measured in the upstream emulsion plate. The x-projection is shown on the left, the y-projection on the right. The spread of the measured tracks is comparable with the spread of the pion beam (∼5 mrad in the x projection).

brick exposed at 6 GeV was scanned in Bologna. On the basis of the expected track density, we decided to scan 4 cm^2 at the centre of the emulsion films; 30 emulsion plates were scanned for the brick exposed to 2 GeV and 4 GeV; for the "6 GeV brick" we scanned all the 55 plates in order to have more information on possible systematic effects. In an OPERA brick, half of the interaction vertexes occur in the first part of the brick and the produced secondaries can be followed downstream for at least ∼30 plates (5 X_0); for the remaining events, it is envisaged to measure the first downstream brick.

Even if both scanning systems routinely work with a tracking efficiency (on mictro-tracks) larger than 96%, for the emulsion plates of these exposures we evaluated a lower efficiency, about 91%. This is mainly due to the low transparency and small thickness of the available emulsions, compared with the standard ones.

All the measured micro-tracks were connected across the base and the quality cut (Eq. 5.4) was applied for each reconstructed base-track. In Fig. 6.12 the base-track angular distributions in the most upstream plate are shown for the 2 GeV

brick. Signal tracks are distributed around the direction $\theta_x = -53$ mrad and $\theta_y = -23$ mrad. The spread of the measured tracks is comparable with the spread of the pion beam estimated with the electronic detectors and the absolute number of reconstructed base-tracks is comparable with the scintillator triggers reported in Tab. 6.1.

We analysed base-tracks with projected angles θ_x and θ_y smaller than 400 mrad: tracks with larger angles are not beam related and are therefore rejected. The number of background tracks (i.e. not beam related) is an important quantity for this analysis and has to be estimated. Since the background is expected to be symmetric with respect the θ_x and θ_y axis, we evaluated it as two times the number of base-tracks falling in the semi-plane not containing the signal peak. The number of estimated background is $\sim$8 tracks/mm^2 within 400 mrad acceptance and is approximately the same for all the bricks within the statistical errors.

The next step in the analysis requires an alignment among the emulsion plates. The bricks were not exposed to cosmic rays so we could only rely on beam tracks. Since we have only one beam direction, the alignment procedure failed to fine-tune the z direction and the plate-to-plate distance has been fixed to its nominal value (1300 μm).

At this point, FEDRA provides a "virtual" volume filled up with base-tracks *segments* in the aligned reference frame. Part of these segments must be linked together in order to reconstruct the signal tracks inside the volume (*volume tracks*). We developed a dedicated algorithm which starts to propagate segments from the first upstream plate. The procedure has been conceived having in mind the real OPERA case, where single tracks emerging from a neutrino vertex have to be reconstructed from the interaction point to the last plate of the ECC brick.

The algorithm is developed taking into account that:

- we have an *a priori* ignorance on the particle identity and momentum;
- we need a good efficiency in connecting segments;
- we have to keep casual matches of background tracks as low as possible.

At this level, a detailed Monte Carlo simulation is in order. The tailoring of the algorithm has been done by studying the behaviour of pions and electrons impinging on the bricks with different momentum.

6.6 Monte Carlo simulation

The simulation of the brick exposures has been done inside the OpRoot framework, the official software package of the OPERA experiment. We simulated pions of 2, 4 and 6 GeV and electrons of 1, 2, 3, 4 and 6 GeV. We used the GEANT3 [67] generator implemented inside OpRoot for the transport and interactions of particles and we stored all charged particle hits having a kinetic energy larger than 1 MeV. All the main processes have been taken into account: MCS, pair production, bremsstrahlung, pion quasi-elastic and inelastic scatterings, charge exchange processes, etc.

The basic information provided by GEANT3 is the micro-track, with a well defined slope and intercept with respect to the brick reference frame. The simulation chain loads these micro-tracks and, on the basis of user-defined parameters, apply a reconstruction efficiency, an angular and position smearing and simulates the number of clusters per micro-track. This "digitization" phase is performed inside the ORFEO framework [68].

The last step of the chain is the micro-track linking and base-track reconstruction. This package provides output files with exactly the same format of real data. From now on, real data and simulated events proceed in parallel, and are analyzed with the same software.

Neither cosmic rays nor environmental background tracks have been simulated. The effects of background on the analysis (and its suppression) has been evaluated *a posteriori* from the comparison of data and simulated volume tracks.

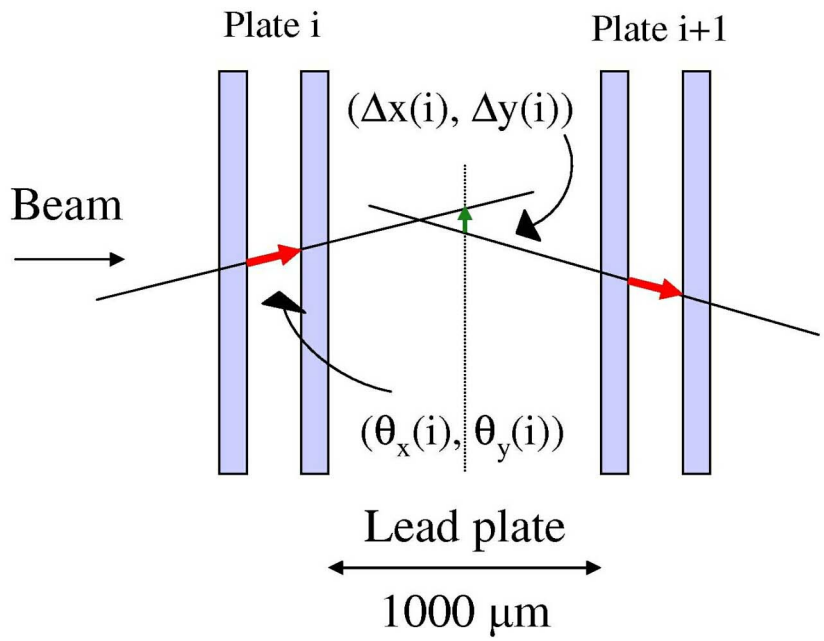

Fig. 6.13: Schematic view of the tracking algorithm.

6.7 Analysis

Base-tracks measured in the first upstream plate, having an angle within 5 standard deviations from the signal direction, were followed downstream with a dedicated algorithm that we are going to describe in detail.

First, the base-tracks on plate i and i+1 are extrapolated at the centre of the lead plate, and angular and position displacements are computed with the formulae

$$\Delta\theta(i) = \sqrt{\Delta\theta_x^2 + \Delta\theta_y^2}$$

$$\Delta r(i) = \sqrt{\Delta x^2 + \Delta y^2}$$

as shown in Fig. 6.13.

If a base-track is found in plate $(i+1)$ that satisfies the *first level* criteria:

$$\Delta\theta(i) \leq 33\,\text{mrad and } \Delta r(i) \leq 21\,\mu\text{m}$$

the track is connected to the next plate.

The angular tolerance allowed by the first level criteria corresponds to about five standard deviations in the expected scattering angle of a m.i.p. with momentum of 1 GeV/c and it takes into account also the measurement angular resolution (about 2 mrad). The corresponding position displacement is computed considering the lever arm of 1300/2 μm between two consecutive base-tracks.

If no track satisfying the first criteria for three[1] consecutive plates is found, *second level* criteria with three time larger tolerances than the first one are applied:

$$\Delta\theta(i) \leq 99\,\text{mrad and } \Delta r(i) \leq 63\,\mu\text{m}$$

If no tracks satisfying the second criteria are found, the track is classified as *stopped*; if more than one track is found, the track is classified as *shower*. For both cases, the propagation is stopped.

If only one track is found, Monte Carlo shows that it could be a large angle hadron scattering or the start of a shower. To correctly identify the two categories, we continue to propagate the secondary track with the first criteria until no more tracks are found. The second criteria are applied again and if at least one other track is found, the event is classified as shower, otherwise the event is analyzed according to its topology: if the scattering occurs in the first 20 plates and the length of the secondary track is smaller than 3 segments, the event is classified as shower, otherwise as a scattered pion.

At the end of the propagation four track classes can be defined:

- *passing-through*: tracks that are propagated through the whole data set only using the first level criteria;

[1]The maximum number of allowed holes along the volume-tracks is strongly dependent on the scanning efficiency on base-tracks. In our case three consecutive holes ensures a probability of fake-stopping particles lower than 0.1%.

- *shower*: tracks that generate a shower in the brick;
- *scattered*: tracks that suffer a large angle scattering;
- *stopped*: tracks that cannot be followed any longer, not with the first criteria, nor with the second.

6.7.1 Estimate of the muon contamination

As discussed in Sec. 6.4.2, the electron contamination in the pion beam is very low ($< 0.4\%$). The muon contamination, for the 2 GeV beam, have been roughly estimated at the level of $\sim$10%. The muon contamination can be better estimated by studying the profile of the track population along the brick. Given the pion interaction length in lead ($\sim$ 170 mm) we expect to observe a sizeable decrease in the number of base-tracks as a function of the crossed cells. We also expect a different behavior for muons, being practically punch-through particles. The muon contamination was evaluated by fitting the experimental distribution to the function

$$N_{data}(z) = N_{\pi}(0) f_{\pi}(z) + N_{\mu}(0) f_{\mu}(z)$$

where $N_{\pi}(0)$ and $N_{\mu}(0)$ are the number of incident pions and muons, respectively, treated as free parameters, and $f_{\pi(\mu)}(z)$ are functions determined with Monte Carlo.

Fig. 6.14 shows the result for the 2 GeV beam. The black points are the data fitted with the function described above. The muon contamination was evaluated to be 38%. The black histogram, superimposed to the data, is a mixture of 62% pions (red histogram) and 38% muons (green histogram). Note that the statistical errors of the fit reported in the box are overestimated, since no poin-to-point correlations have been taken into account. A proper treatment of the errors gives an uncertainty of the order of 1%. The muon contamination for the 6 GeV brick was evaluated using all the 55 plates. In this case the contamination is low (at the level of 6%) as shown in Fig. 6.15. The contamination of the 4 GeV brick is at the same level of the 6 GeV brick.

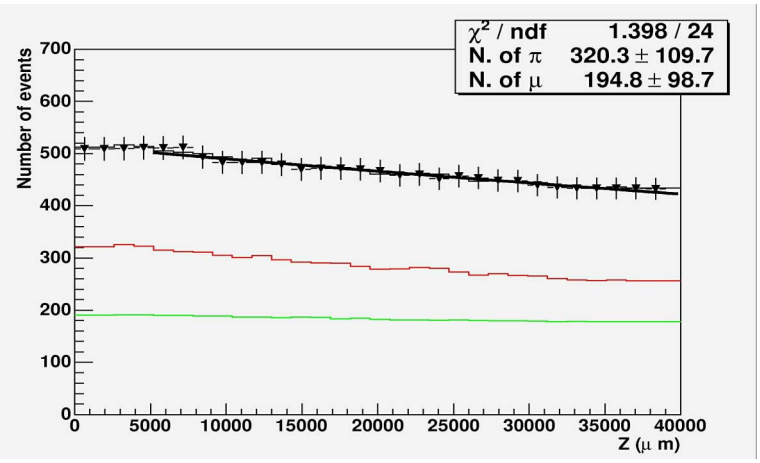

Fig. 6.14: Number of tracks as a function of the crossed plates for the brick exposed at 2 GeV/c pions. Black dots are the data while the black histogram is the sum of pion (red histogram) and muon (green histogram) contributions obtained by the fit.

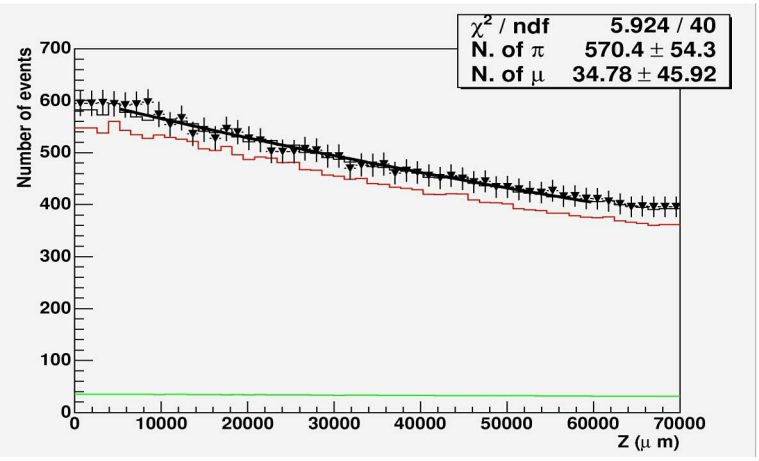

Fig. 6.15: The muon contamination in the 6 GeV/c pion beam. The contamination is very low and can be evaluated only by using the whole exposed brick.

6.7.2 Efficiency, angular resolution and momentum measurement

Fig. 6.16 shows the distribution of the number of segments (left) and the number of crossed ECC plates (right) for all propagated tracks, both for the experimental data and the Monte Carlo simulation. The muon contamination has been properly added in the simulated samples, as shown by the superimposed shadowed histograms. The excess of volume-tracks with small number of segments ($N_{seg} \lesssim 4$) in the experimental data is due to (not simulated) background casual matches.

The simulation takes into account the experimental efficiencies and angular resolution of base-tracks, evaluated as follows. Scanning efficiencies have been evaluated considering passing-through tracks with the prescription described in Sec. 5.5.3. The micro-track efficiency is about 91%, with plate-to-plate variations of the order of 5%. This low value is mainly due to the poor quality of the emulsion plates used in the exposures.

A safer way to estimate the angular resolution, purified from the MCS contribution, is to analyze the RMS of the angular difference distribution as a function of the number of crossed plates. Considering only passing-through tracks, we fitted the data point to the function

$$f(x) = \sqrt{(\sqrt{2}\delta\theta)^2 + (13.6/p)^2(x/5.81)\left[1 + 0.038\ln(x/5.81)\right]^2}$$

where the momentum p is expressed in MeV/c, the crossed ECC thickness x in mm and $\delta\theta$ in mrad. The resulting angular resolution on the single base-track is then $\delta\theta$. In Fig. 6.17 are presented the RMS curves for passing-through tracks of 2, 4 and 6 GeV/c bricks. The angular resolution ranges from 1.6 to 2.4 mrad.

Note that the momentum resulting from this fitting procedure is statistically equivalent to the average momentum of all the selected tracks. A track-by-track momentum estimate can be obtained with the method described in [69]. Fig. 6.18 (left panels) shows the measured $1/p$ distribution fitted to a gaussian with standard deviations of 31%, 26% and 19% for 2, 4 and 6 GeV/c pions. On the right panels,

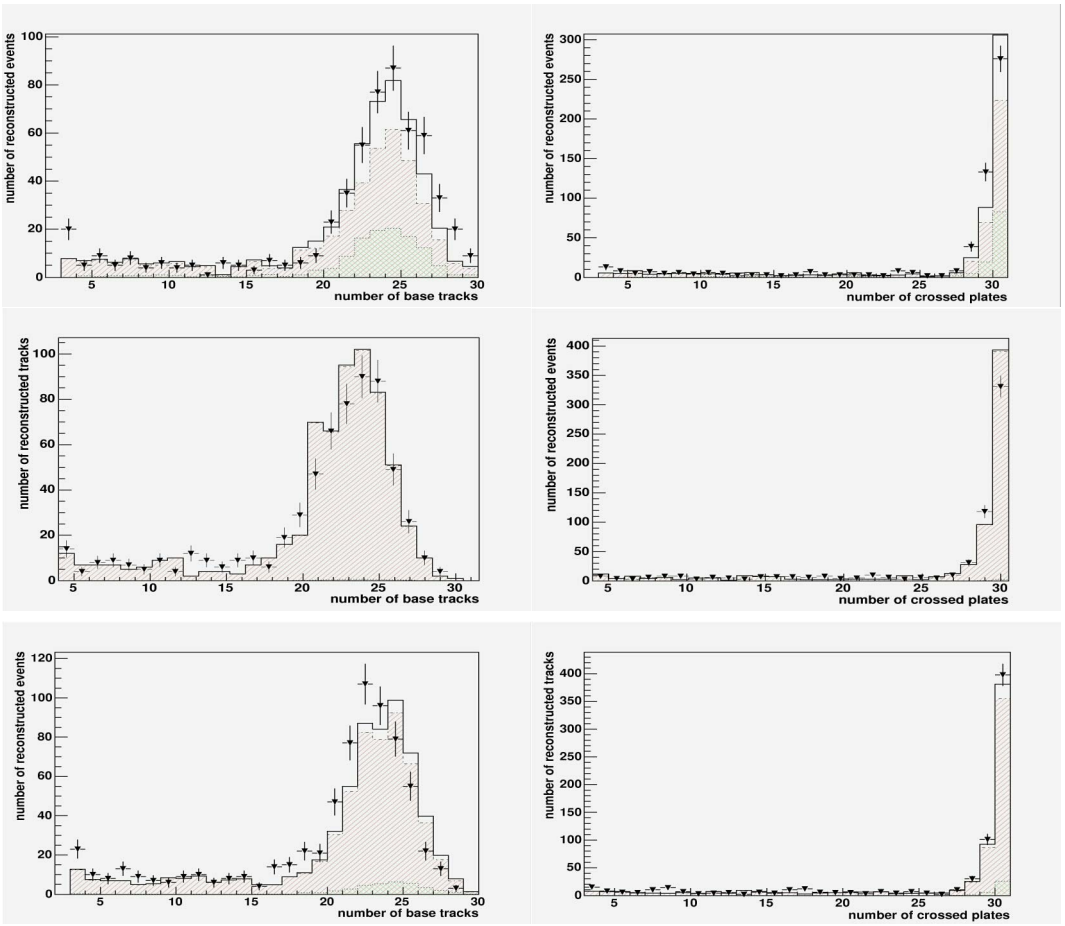

Fig. 6.16: Number of segments associated to a propagated track (left) and number of crossed plates (right) as obtained with the propagation algorithm for the 2 GeV/c brick (top), 4 GeV/c brick (centre) and 6 GeV/c brick (bottom). The first 30 scanned plates are used for all the data sets. Black dots are data, solid histograms are Monte Carlo simulations, a mixture of pions (right dashed) and muon (left dashed).

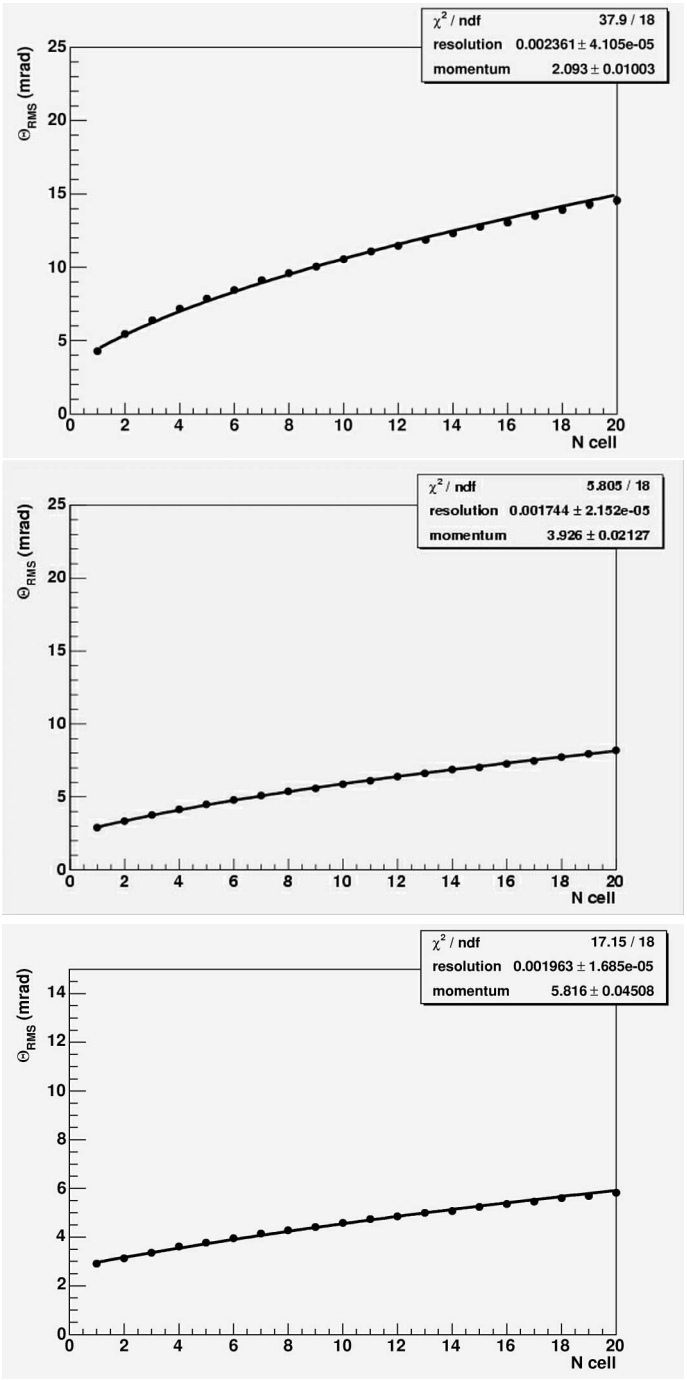

Fig. 6.17: RMS of the angular difference distributions as a function of the number of crossed ECC cells for passing through tracks. Top: 2 GeV/c brick, centre: 4 GeV/c brick, bottom: 6 GeV/c brick.

the p distributions are fitted to the function

$$f(x) = \frac{a_1 \exp\left[-\left((1/x) - (1/a_2)\right)^2 1/a_3^2\right]}{x^2}$$

where a_i (with i=1,2,3) are the parameters to be fitted. Note that for the 2 GeV/c and 4 GeV/c exposures 30 plates have been analysed while for the 6 GeV/c all the plates have been considered. Moreover, the 2 GeV/c brick contains a significant fraction of muons (38%) which spoils the momentum resolution from the expected one (∼21%).

6.7.3 Pion-electron identification algorithm

The average energy of an electron after passing through a material of thickness z decreases exponentially as described in Sec. 6.2, while for pions it is almost constant. Fig. 6.19 schematizes bremsstrahlung emissions of an electron passing through an ECC brick. Fig. 6.20 shows the different MCS behaviour for simulated pions (red squares) and electrons (blue triangles) as a function of crossed emulsion plates (in X_0 units). The events are simulated with an initial momentum of 2, 4 and 6 GeV/c (top, centre and bottom respectively).

Taking into account this characteristic, we defined a parametric χ^2 function as

$$\chi^2_{e,\pi} = \sum_{i=1}^{N-1} \frac{\left\{\left[\Delta\theta_x(i) - \Delta\Theta_{e,\pi}(i)\right]/\Delta\Theta_{e,\pi}(i)\right\}^2 + \left\{\left[\Delta\theta_y(i) - \Delta\Theta_{e,\pi}(i)\right]/\Delta\Theta_{e,\pi}(i)\right\}^2}{2(N-1)} \tag{6.10}$$

where N is the number of base-tracks associated to the track, $\Delta\theta_{x,y}(i)$ is the difference in angle between two consecutive (even if not necessarily adjacent) segments and

$$\Delta\Theta_{e,\pi} \equiv \sqrt{(\sqrt{2}\delta\theta)^2 + (13.6/p_{e,\pi}(z) \times \sqrt{d/X_0})^2} \tag{6.11}$$

is the expected scattering angle for momentum $p_{e,\pi}(z)$ and angular resolution $\delta\theta$.

For each selected track, the $\chi^2_{e,\pi}$ is calculated under the two hypotheses (electron and pion). Leaving the initial energy free to variate in the physical range, the two $\chi^2_{e,\pi}$ are minimized independently and $\Delta\chi^2 \equiv \chi^2_e - \chi^2_\pi$ is used as a separator for the two particles: $\Delta\chi^2 > 0$ are pion-like, $\Delta\chi^2 < 0$ are electron-like.

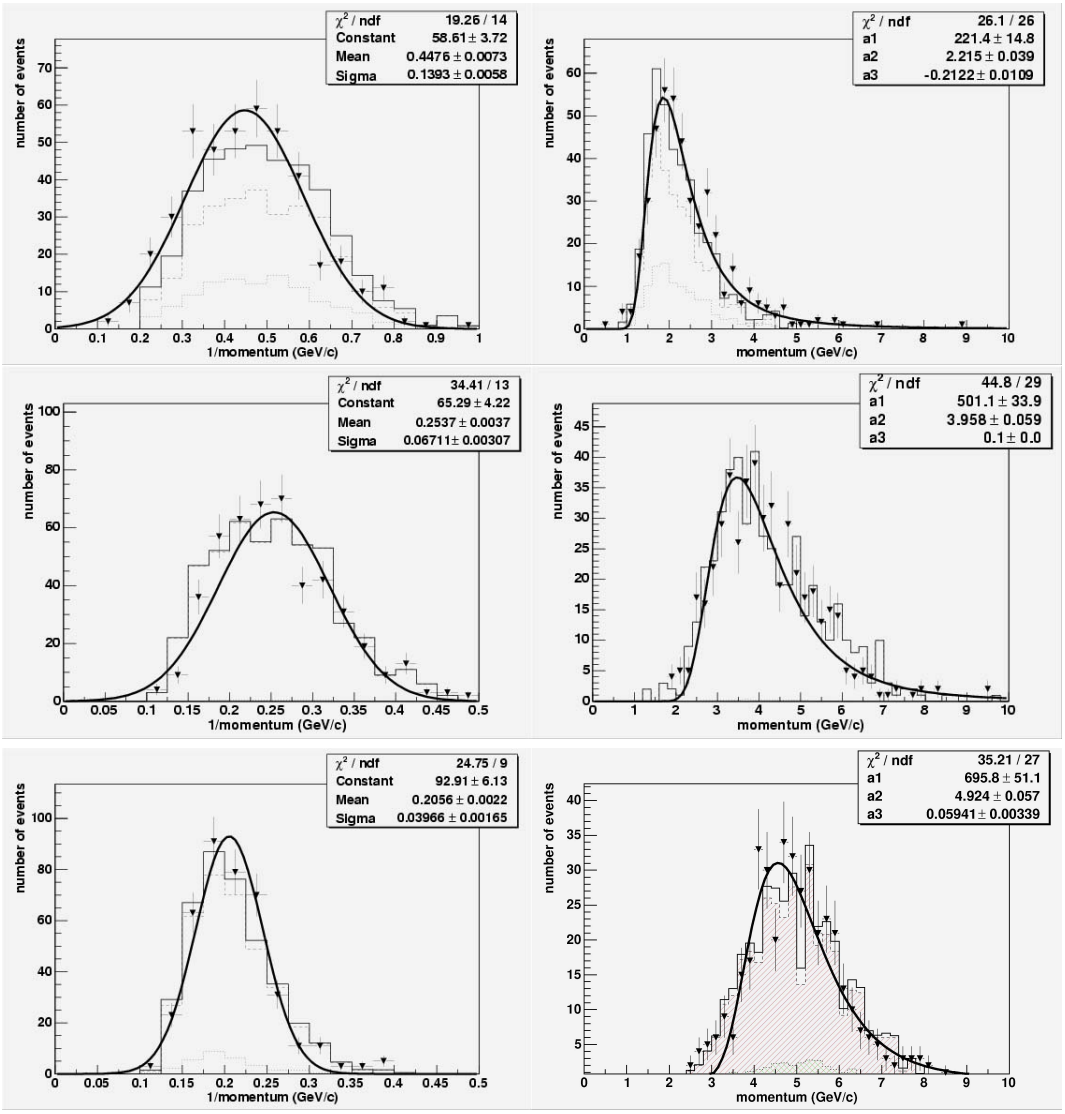

Fig. 6.18: Measured $1/p$ distribution (left) and momentum distribution (right) for passing-through tracks in the 2 GeV/c brick (top), 4 GeV/c brick (centre) and 6 GeV/c brick (bottom). Dots are pion data, histograms are Monte Carlo. The momentum for 6 GeV pions has been calculated using all the 55 ECC plates while for the other bricks only 30 ECC plates are used.

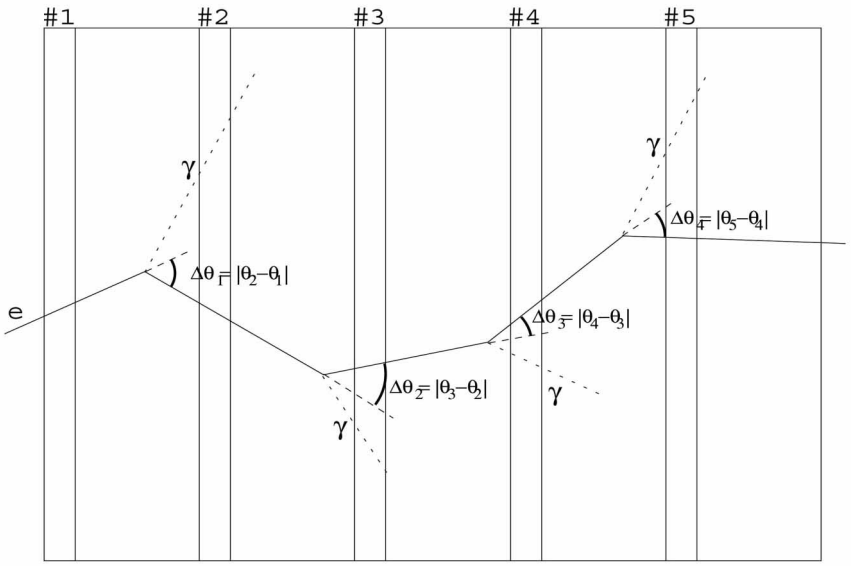

Fig. 6.19: Schematic view of an electron propagating through a brick.

We consider only volume tracks with at least two base-tracks and require them to be consecutive in the first and second plates. This "trigger" defines our normalization sample. Monte Carlo simulation shows that tracks outside this trigger definition (mostly back-scattered particles) are negligible. According to this request, a total of 578 tracks are selected in the 2 GeV brick, 660 tracks in the 4 GeV brick and 688 in the 6 GeV brick. Some of them are followed only in two or three plates and are not classified (the reason will be explained in the following).

The number of events classified as passing through, shower, stopped or scattered are reported in Tab. 6.2. The last row of this table reports the fraction of events not classified ($N_{seg} \leq 3$) with respect to the number of classified events. For this sample, we note a factor $\sim$2 difference between data and Monte Carlo simulation due to the presence of background. The not-classified event sample of experimental data has been epurated from background considering the difference of these fractions.

Although the $\Delta\chi^2$ separator is used only for events classified as stopped, we

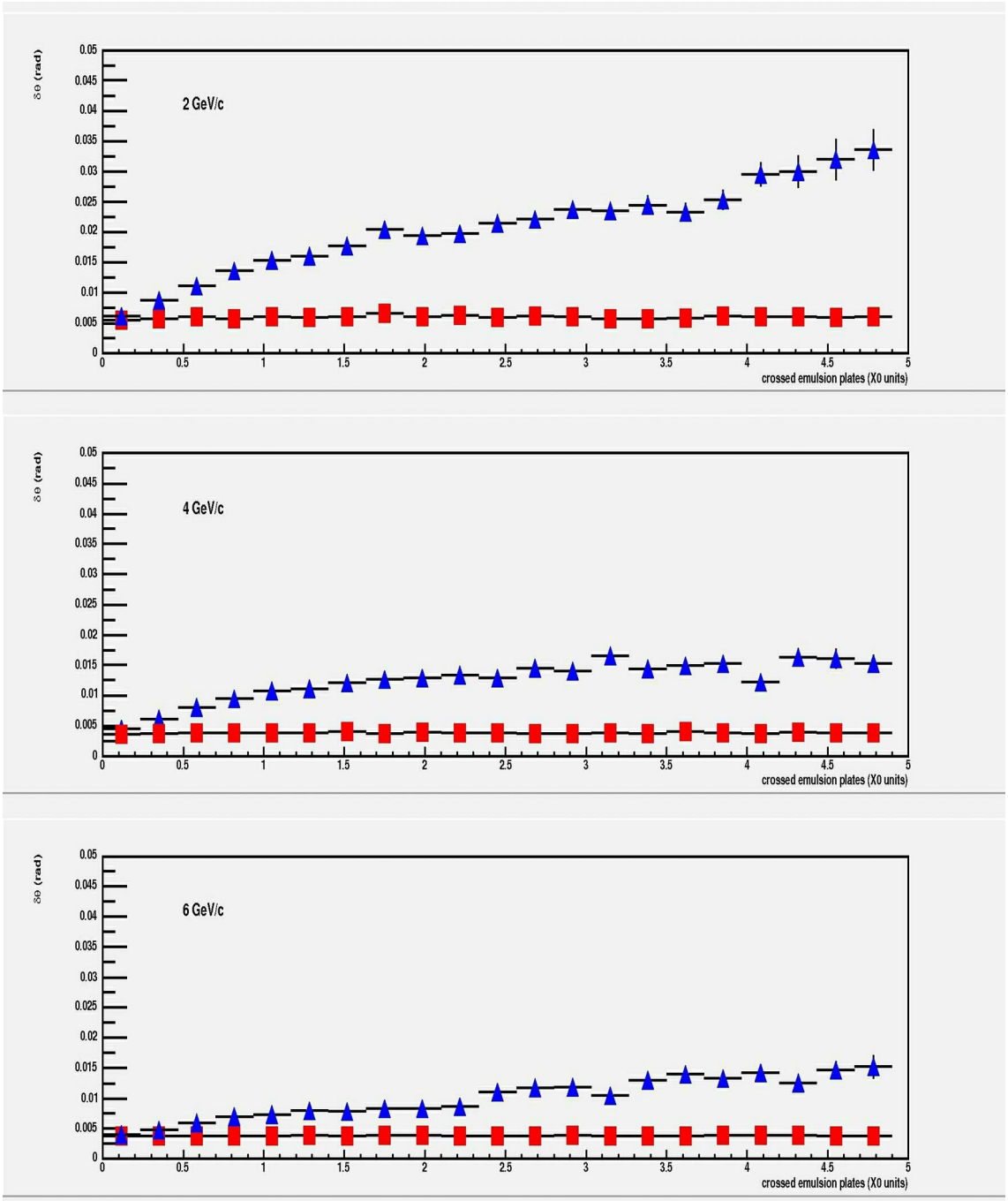

Fig. 6.20: Scattering angle distributions for simulated pions (red rectangles) and electrons (blue triangles), with an initial momentum of 2, 4 and 6 GeV, as a function of the crossed emulsion plates (X_0 units).

	Data			Monte Carlo		
p_{beam} (GeV/c)	2	4	6	2	4	6
Passing through	431 (79%)	473 (77%)	393 (62%)	411 (75%)	495 (79%)	895 (61%)
Shower	16 (3%)	15 (2%)	21 (3%)	11 (2%)	10 (2%)	33 (2%)
Stopped	71 (13%)	115 (19%)	191 (30%)	101 (18%)	89 (14%)	452 (31%)
Scattered	26 (5%)	12 (2%)	33 (5%)	26 (5%)	36 (6%)	84 (6%)
Not classified	34 (6%)	45 (7%)	50 (8%)	22 (4%)	22 (3%)	46 (3%)

Tab. 6.2: Number of analysed tracks for data and Monte Carlo pions. In brackets are reported percentages with respect to the total number of classified events. Note that data events with $N_{seg} \leq 3$ (not classified sample) contains a sizable of not simulated background, evaluated by comparing the Monte Carlo sample.

calculated $\Delta\chi^2$ for all the classified tracks for consistency checks. Fig. 6.21 shows the $\Delta\chi^2$ distributions for data and Monte Carlo simulation. Monte Carlo pions and muons are mixed with the measured ratio.

Passing through tracks, scattered tracks and stopped tracks with a $\Delta\chi^2 > 0$ are identified as pions while shower tracks and stopped tracks with $\Delta\chi^2 < 0$ are identified as electrons. The pion identification efficiency ($\epsilon_{\pi\to\pi}$) is defined as the fraction of tracks identified as pions over the total number of selected tracks; the probability to identify a pion as an electron ($\eta_{\pi\to e}$) is defined as the fraction of tracks identified as electrons over the total number of tracks.

In Fig. 6.22 we show the identification efficiencies and the mis-identification probabilities for simulated 2 GeV/c pions (left panels) and electrons (right panels) as a function of the minimum number of segments requested for classification. The fraction of selected events over the total number of events (trigger efficiency) is also shown.

The classification of tracks with a number of segments smaller than 4 provides a small efficiency gain and a sizable increase in the mis-identification probability. Moreover, as we know, this sample contains a sizable fraction of background tracks in the data. This result reinforces the choice $N_{seg} \leq 4$ requested for classification.

The resulting pion identification efficiency (and the mis-identification probabil-

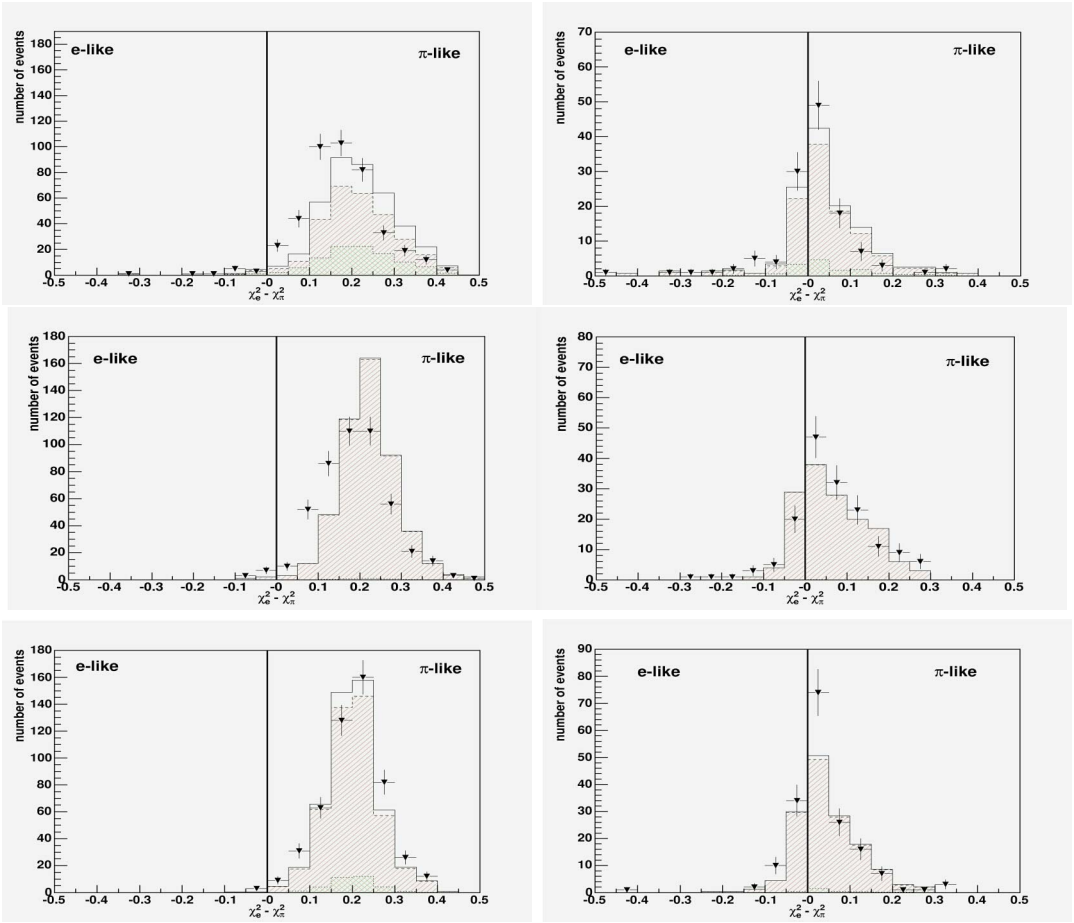

Fig. 6.21: $\Delta\chi^2$ distribution for tracks classified as passing through (left) and for all the other classified tracks (right). Black triangles are data, histograms are Monte Carlo for 2 GeV/c (top), 4 GeV/c (center) and 6 GeV/c (bottom). Monte Carlo pions and muons are mixed with the measured ratio.

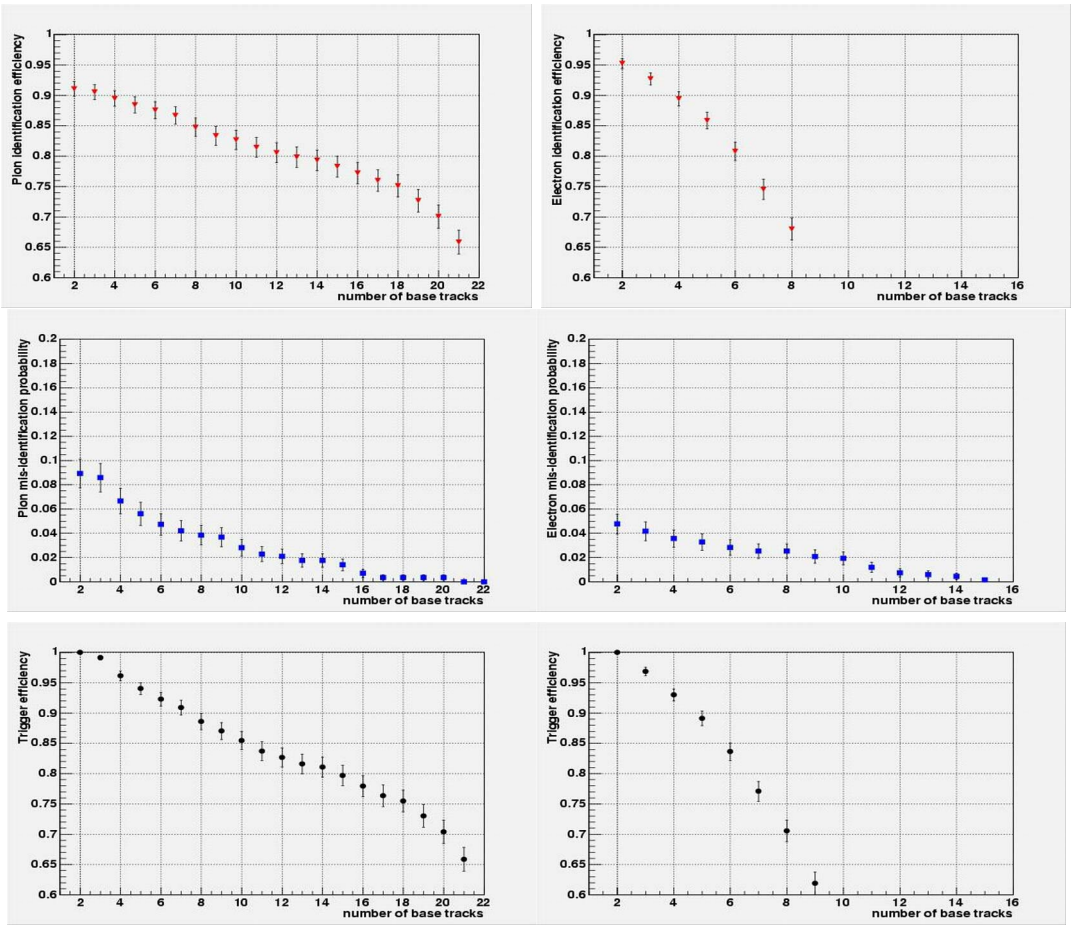

Fig. 6.22: 2 GeV/c Monte Carlo simulations. Top: pion (left) and electron (right) identification efficiencies and middle: mis-identification probabilities as a function of the minimum number of segments requested for classification. On the bottom panels are shown the fractions of classified events over the total triggered events.

ity) is finally computed taking into account the muon contamination:

$$\epsilon_{\pi\to\pi}^{measured} = \frac{N_\pi}{N_{tot}}\epsilon_{\pi\to\pi} + \frac{N_\mu}{N_{tot}}\eta_{\mu\to\pi} \tag{6.12}$$

where the $\epsilon_{\pi\to\pi}^{measured}$ is the fraction of events classified as pions over the total selected events. $\eta_{\mu\to\pi}$ and $\eta_{\mu\to e}$ are evaluated according to Monte Carlo and reported in Tab. 6.3. The experimental pion identification efficiencies and the pion mis-identification probabilities are reported in Tab. 6.4 together with the Monte Carlo results.

	Monte Carlo		
p_μ (GeV/c)	2	4	6
$\eta_{\mu\to\pi}$	0.94	0.98	0.99
$\eta_{\mu\to e}$	0.03	0.01	0.01

Tab. 6.3: Probability to identify a muon as a pion or as an electron for the three different energies, as obtained with a Monte Carlo simulation.

	Data			Monte Carlo		
p_{beam} (GeV/c)	2	4	6	2	4	6
$\epsilon_{\pi\to\pi}$	0.88	0.92	0.89	0.89	0.92	0.91
$\eta_{\pi\to e}$	0.09	0.05	0.08	0.07	0.04	0.06
ϵ_{NC}	0.03	0.03	0.03	0.04	0.03	0.03

Tab. 6.4: Pion identification efficiencies and mis-identification probabilities for the 3 exposed bricks. Data and Monte Carlo results are reported.

These results clearly depend on the number of segments per track. In other words, if we select sub-samples of volume-tracks with an ever increasing number of segments, we expect an increase of the identification efficiency and a decrease of the mis-identification probability. Fig. 6.23 shows the identification efficiencies and the mis-identification probabilities, obtained from experimental data, selecting volume-tracks having a minimum number of segments ranging from 2 to 18.

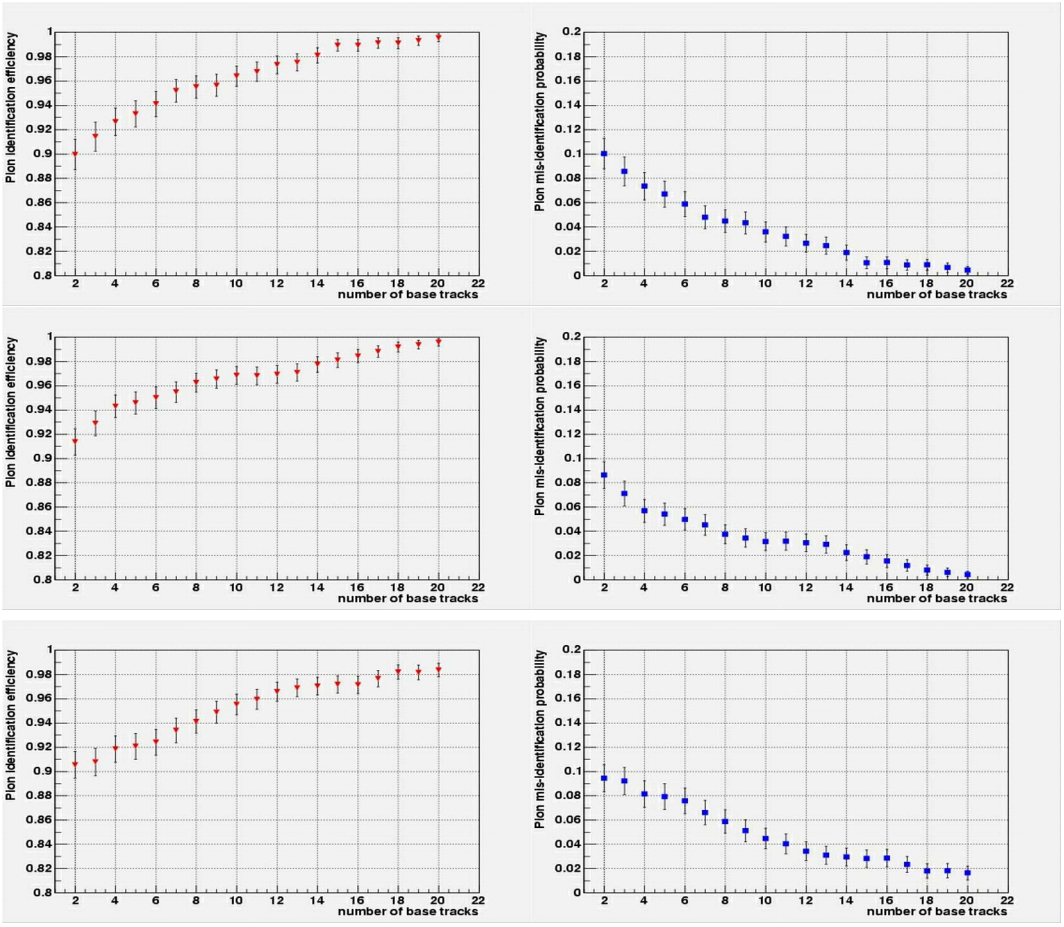

Fig. 6.23: Experimental data (hadron exposure at CERN): Pion identification efficiencies (left) and pion mis-identification probabilities (right) for the tree analyzed bricks: 2 GeV (top), 4 GeV (centre) and 6 GeV (bottom). These results are obtained taking into account only volume tracks with a minimum number of segments from 2 to 18.

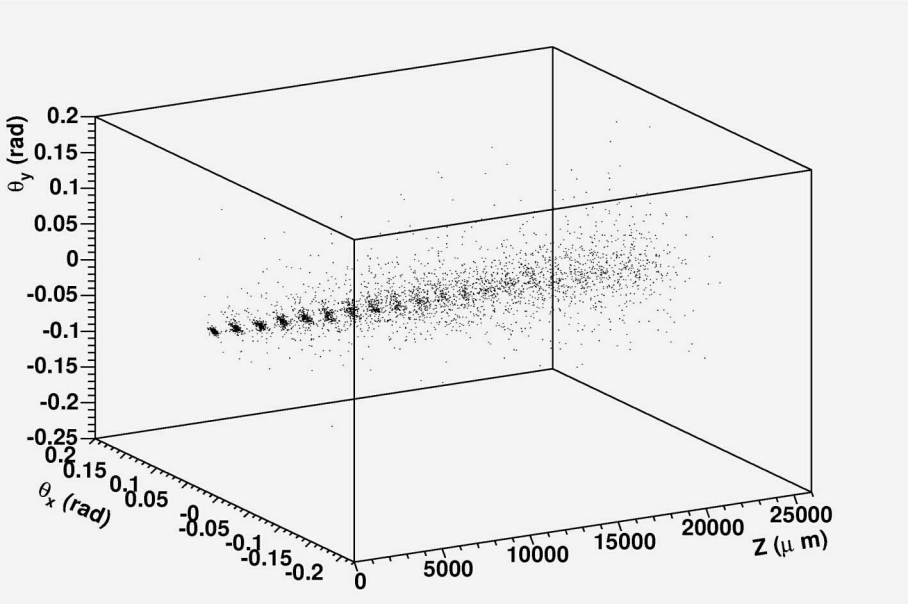

Fig. 6.24: Angular spread for reconstructed tracks as a function of the z position along the brick in the 6 GeV "electron brick" exposed at DESY.

6.7.4 The pure electron data

Pure pion exposures have been complemented with pure electron exposures at DESY. A detailed description of this test is given in [2]. 15 emulsion plates have been exposed to 1 and 3 GeV, with a density of about 50 electrons/cm^2 and 100 electrons/cm^2 respectively; 20 emulsion plates have been exposed to 6 GeV electrons with a density of about 100 electrons/cm^2.

Data have been reconstructed with the propagation algorithm described in Sec. 6.7. As an example of the results of this propagation, we show in Fig. 6.24 the angular spread of the reconstructed tracks in the 20 plates exposed to 6 GeV electron beam. The trajectories inside the brick of some reconstructed tracks are shown in Fig. 6.25.

Before we apply the classification scheme and the χ^2 analysis described in the previous sections, we show in Fig. 6.26 scattering profile as a function of crossed ECC cells both for experimental data and Monte Carlo simulation. We note the different behaviours of electrons and pions and the nice agreement between data

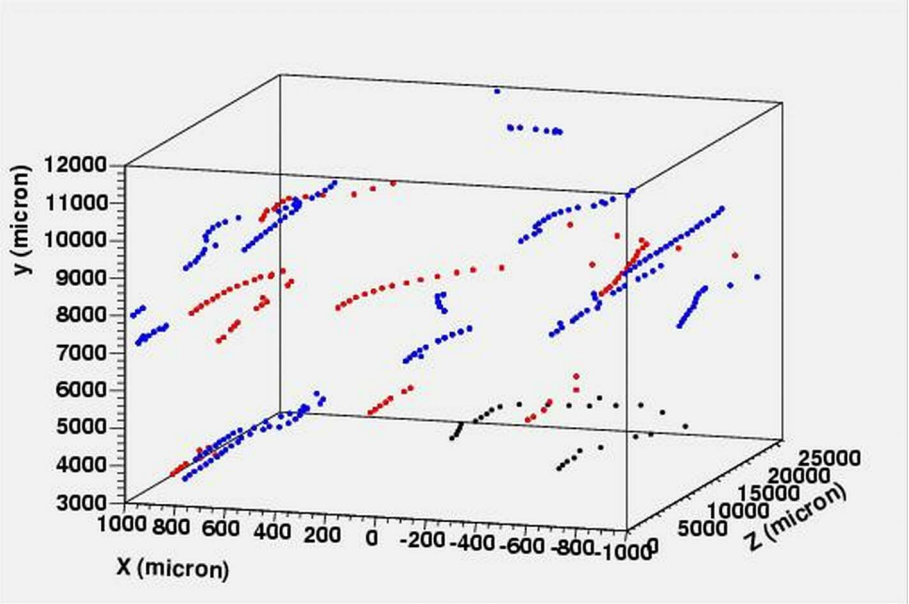

Fig. 6.25: Some of the reconstructed electron tracks in the brick exposed at 6 GeV/c. Tracks classified as showers are shown in red.

and Monte Carlo.

We estimated the electron identification efficiency (and mis-identification probability) with the same classification scheme described in the previous section (tracks with $N_{seg} \leq 3$ are not classified). Since we have a limited number of cells, passing-through tracks are always analysed in terms of $\Delta\chi^2$ and not automatically interpreted as pions. Comparison between data and Monte Carlo is shown in Fig. 6.27 in terms of $\Delta\chi^2$ for all events. Tab. 6.5 reports, for each exposed brick, the number of tracks that have been propagated and classified.

According to the analysis scheme we have previously described, the fraction of electrons correctly identified ($\epsilon_{e\to e}$) is 0.87, 0.85 and 0.92 for 1, 3 and 6 GeV electron beams respectively. The probability of mis-identify electrons with pions ($\eta_{e\to\pi}$) is 0.09, 0.01, 0.03 for 1, 3 and 6 GeV electron beams respectively.

Differently from what observed in the case of pions, the electron identification

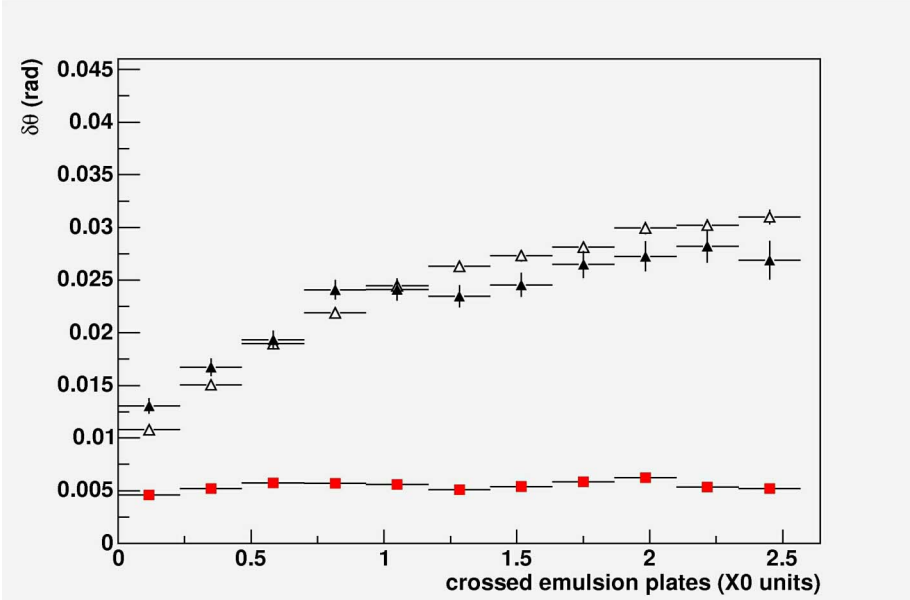

Fig. 6.26: DESY exposure at 1 GeV: electron scattering profile for experimental data (black filled triangles) and Monte Carlo simulation (empty triangles). For comparison the scattering profile for 2 GeV experimental pions are plotted (red squares).

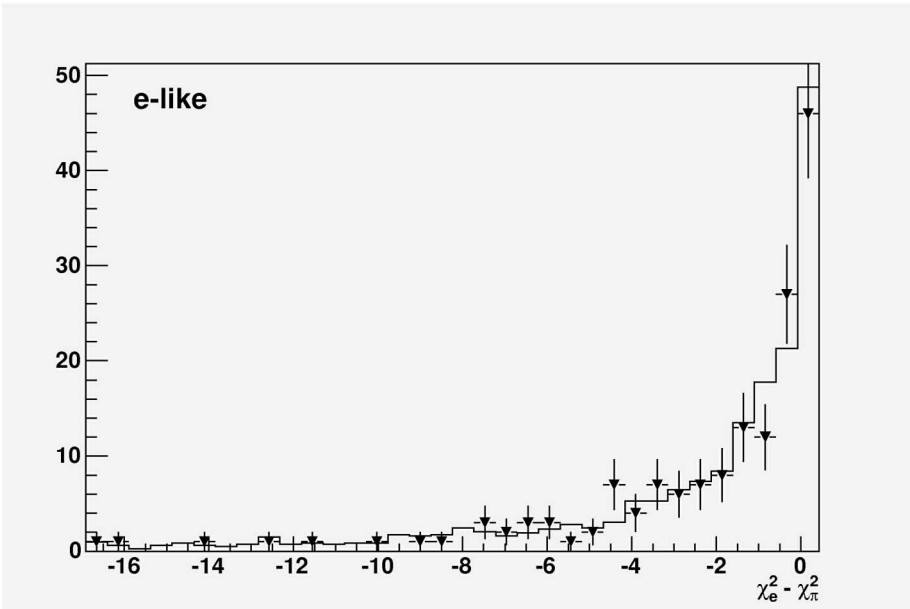

Fig. 6.27: Distribution of the $\Delta\chi^2$ distribution for the pure electron data exposed to 1 GeV/c (black dots). For comparison, $\Delta\chi^2$ for Monte Carlo events are also shown (black histogram).

efficiencies and mis-identification probabilities do not change when track samples with increasing number of segments are selected (see Fig. 6.28 and, for comparison, Fig. 6.23).

In Tab. 6.6 we give an overall survey of the results, both for pion and electron data, compared with the results reported in Ref.[64] and obtained with electron enriched pion beam exposures.

p_{beam} (GeV/c)	1	3	6
Passing-trough	207	379	290
Shower	0	181	177
Stopped	0	46	14
Scattered	0	3	3
Not classified (MC corrected)	8	25	23

Tab. 6.5: DESY electron data. Number of experimental events analysed and classified. Differently from pion analysis, here the $\Delta\chi^2$ separator has been used also for passing-through tracks.

p_{beam} (GeV/c)	1	2	3	4	6
$\epsilon_{\pi\pi}$		0.88 (0.93)		0.92 (0.95)	0.89
$\eta_{\pi e}$		0.09 (0.06)		0.05 (0.04)	0.08
ϵ_{ee}	0.87	(0.88)	0.95	(0.91)	0.92
$\eta_{e\pi}$	0.09	(0.10)	0.01	(0.08)	0.03

Tab. 6.6: Pion and electron identification efficiencies and mis-identification probabilities as obtained with this analysis. In brackets are reported results given in [64].

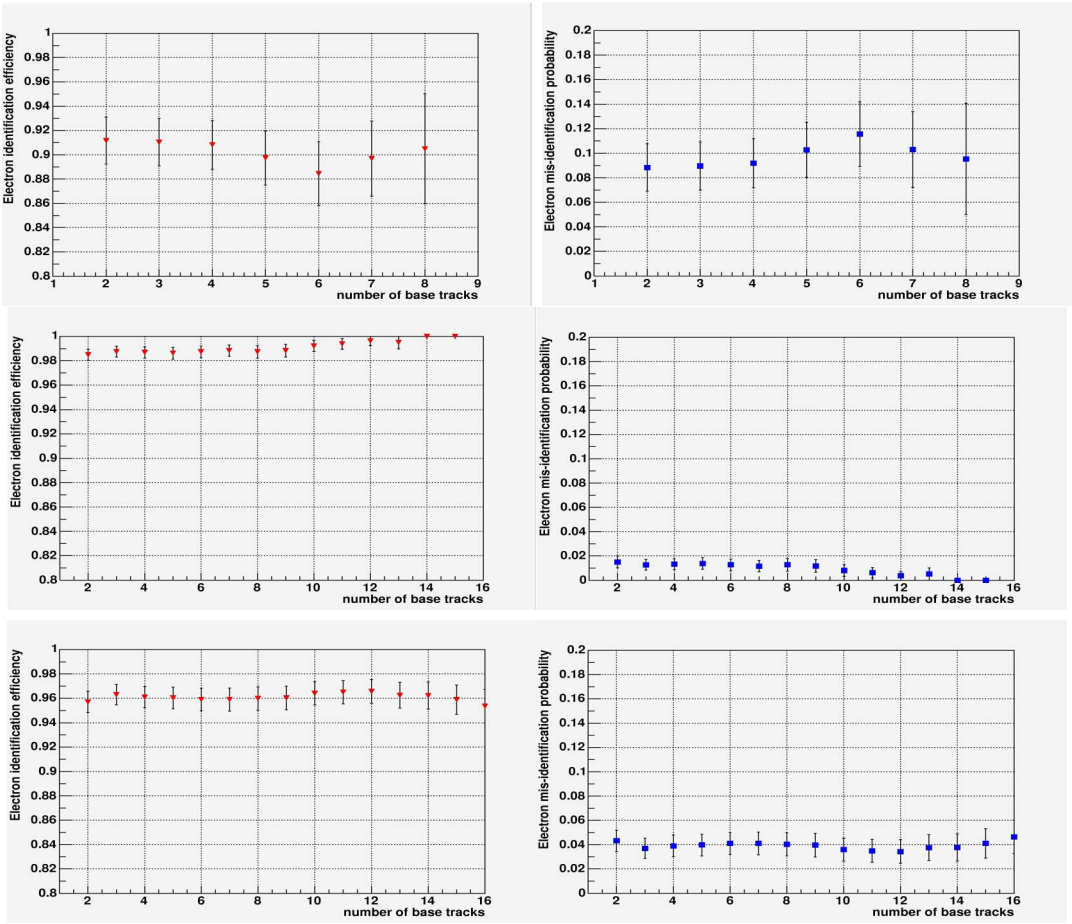

Fig. 6.28: Experimental data. Electron identification efficiencies (left) and electron mis-identification probabilities (right) for the tree analyzed brick: 1 GeV (top), 3 GeV (centre) and 6 GeV (bottom). These results are obtained taking into account only volume track with a minimum number of segments from 2 to 16.

Conclusions

The OPERA experiment is attacking a key problem for the knowledge of neutrino physics. If tau neutrinos will be observedin the CNGS beam, the hypothesis of neutrino oscillations will be completely and undoubtly confirmed.

The detector construction is going smoothly and in slightly more than one year from now the first neutrinos from CERN will be delivered and detected at Gran Sasso. One of the striking features of the experiment is the very low number of expected background events, less than one event in five years running with a counterpart of 10-20 signal events.

The most challenging task of the experiment will be the quasi on-line scanning of a large amount of nuclear emulsions. This task will be fulfilled by a dedicated battery of completely automated optical microscopes, characterized by high scanning speed, and high efficiency. These requirements boosted a large R&D effort which is going to be completed. Many bricks per day will be shared among a network of scanning laboratories, both in Europe and in Japan. The Bologna scanning Lab. is included in the network and partecipated in the crucial steps of the R&D project.

The first part of this thesis reported on the work done in Bologna in order to reach the performances required for scanning OPERA emulsions. After a 3 years effort our microscopes have reached a scanning speed of 20 cm^2 per hour, an order of magnitude larger of analogous systems of the past generation. The reconstruction of particle tracks in emulsion is performed at the sub-micrometric level with an efficiency larger than 96%. The corresponding angular resolution is at the level of 1 mrad, well below what is required for a precise reconstruction of a typical tau

lepton decay kink. The instrumental background of the system, i.e. the number of reconstructed fake-tracks, has been evaluated to be at the level of $\sim$2 tracks/cm^2 in the nominal angular acceptance of the experiment. The system calibration has been carried out with dedicated test-beam exposures performed at the CERN-PS with charge hadrons of known momenta and directions.

Once the automatic scanning microscopes were tested and checked, they have been used to make measurements of emulsions exposed to pions and electron beams. The second part of the work presented in this thesis is an experimental study of the particle identification capability by OPERA ECC bricks, in particular for electron-hadron separation. A correct identification of particles is important both to reject the background and to gain in efficiency and sensitivity. Up to now, these performances were estimated via Monte Carlo or with experimental tests relying on simulations. Here we presented a measurement of electron and pion identification efficiencies as obtained from exposures to pure pion and electron beams. The discrimination principle is based on the different energy loss and Coulomb multiple scattering behaviors of hadrons and electrons in matter. We developed a propagation algorithm to follow tracks along the brick, having in mind that we ignore *a priori* the particle identities and their momenta.

We obtained identification efficiencies of the order of 90%, both for pions and electrons, in the energy range 1$\div$6 GeV. The mis-identification probabilities are few percents at energy above 3 GeV while, at lower energies, they reached 9%. These results must be considered as lower limits to what is expected in the real OPERA case, since the quality and small thickness of the emulsions used in the pion exposures deteriorated the scanning efficiencies. Further improvements could also be obtained by merging the tecnique presented in this thesis with a complete shower analysis, complementing the information coming from the multiple Coulomb scattering before the shower development.

Bibliography

[1] B. Pontecorvo, Zh. Eksp. Teor. Fiz. 33 (1957) 549;
B. Pontecorvo, Zh. Eksp. Teor. Fiz. 33 (1957) 549;
Zh. Eksp. Teor. Fiz. 34 (1958) 247; Zh. Eksp. Teor. Fiz. 53 (1967) 1717.

[2] L. S. Esposito, *Study of electron identification in the emulsion cloud chambers of the OPERA experiment*, PhD Thesis, Bologna (2005).

[3] W. Pauli, letter to a physicist's gathering at Tubingen, December 4, 1930. Reprinted in *Wolfgang Pauli, Collected Scientific Papers*, ed. R. Kronig and V. Weisskopf, Vol. 2, p. 1313 (Interscience: New York, 1964).

[4] S.L. Glashow, Nucl. Phys., **22** (1961) 579;
S. Weinberg, Phys. Rev. Lett. **19** (1967) 1264;
A. Salam, Proceedings of the 8th Nobel Symposium on *Elementary particle theory, relativistic groups and analyticity*, (1968), ed. Swartholm, Almquist and Wiksells, p.367.

[5] L. Landau, Nucl. Phys. **3** (1957) 127.

[6] T.D. Lee and C.N. Yang, Phys. Rev. **105** (1957) 1671.

[7] E. Majorana, Nuovo Cim. **14** (1937) 171.

[8] M. Gell-Mann, P. Ramond and R. Slansky, *Supergravity*, ed. D. Freedman and P. van Nieuwenhuizen (North-Holland, Amsterdam, 1979), p. 315;
T. Yanagida, *Proceedings of the Workshop on Unified Theory and Baryon Number in the Universe*, ed. O. Oswada and A. Sugamoto (Japan, 1979);

R. Mohapatra and G. Senjanovic, Phys. Rev. Lett. **44** (1980) 912; Phys. Rev. Lett. D **23** (1981) 165.

[9] C.K. Jung, C. McGrew, T. Kajita and T. Mann, Ann. Rev. Nucl. Part. Sci. **51** (2001) 451.

[10] S. Eidelman et al. (Particle Data Group), Phys. Lett. B **592** (2004) 467.

[11] Z. Maki, M. Nakagawa and S. Sakata, Progr. Theor. Phys. 28 (1962) 870.

[12] B. Kayser, *Neutrino physics as explored by flavor change* in K. Hagiwara et al. (Particle Data Group), Phys. Rev. D **66** (2002) 392.

[13] L. Wolfenstein, Phys. Rev. D **17** (1978) 2369;
S. Mikheyev and A. Smirnov, Sov. J. Nucl. Phys. **42** (1986) 913; Sov. Phys. JETP **64** (1986) 4; Nuovo Cim. **9C** (1986) 17.

[14] F. Boehm and P. Vogel, *Physics of Massive Neutrinos*, Cambridge Univ. Press, (Cambridge 1987).

[15] B. T. Cleveland et al., Astrophys. J. **496** (1998) 505.

[16] R. Bionta et al. (IMB Coll.), Phys. Rev. Lett. **54**, 22 (1985);
R. Becker-Szendy et al., Phys. Rev. D **46** (1992) 372.

[17] K. S. Hirata et al. (Kamiokande Coll.), Phys. Lett. B **280**, 146 (1988); Phys. Lett. B. **280**, 146 (1992);
Y. Fukuda et al. (Kamiokande Coll.), Phys. Lett. B **335**, 237 (1994).

[18] W.W.M. Allison et al., *Phys. Lett.* B **449**, 137 (1999);
M. Sanchez et al., Phys. Rev. D **68** (2003) 113004.

[19] M. Ambrosio et al. (MACRO Coll.), *Phys. Lett.* B **434**, 451 (1998).

[20] Y.Fukuda et al. (SuperKamiokande Coll.), *Phys. Rev. Lett.* **81**, 1562 (1998); *Phys. Lett.* B **433**, 9 (1998); *Phys. Rev. Lett.* **85**, 3999 (2000).

[21] S.H. Ahn et al., Phys. Lett. B **511** (2001) 178;
S.H. Ahn et al., Phys. Rev. Lett. **90** (2003) 041801.

[22] Q. R. Ahmad et al. (SNO Coll.), Phys. Rev. Lett. **87** (2001) 071301.

[23] S. Fukuda et al., Phys. Rev. Lett. **86** (2001) 5651.

[24] Q. R. Ahmad et al. (SNO Coll.), Phys. Rev. Lett. **89** (2002) 011301;
S. Ahmad et al., nucl-ex/0309004.

[25] K. Eguchi et al. (KamLAND Coll.), Phys. Rev. Lett. **90** (2003) 021802.

[26] J. N. Bahcall, Astrophys. J. **467** (1996) 475;
J. N. Bahcall, S. Basu, M. H. Pinsonneault, Phys. Lett. B **433** (1998) 1.

[27] J. N. Abdurashitov, et al., Phys. Rev. C **60**, 055801 (1999);
W. Hampel, et al., Phys. Lett. B **447**, 127 (1999).

[28] M. Ambrosio et al., Phys. Lett. B **517** (2001) 59.

[29] M. Ambrosio et al., Phys. Lett. B **566** (2003) 35.

[30] Y. Ashie et al., Phys. Rev. Lett. **93** (2004) 101801.

[31] E. Aliu et al. (K2K Collaboration), Phys. Rev. Lett. **94** (2005) 081802.

[32] M. V. Diwan, hep-ex/0211026.

[33] C. Albright et al., *Physics at a Neutrino Factory*, Fermilab-FN-692 (May 2000).

[34] M. Apollonio et al. (CHOOZ Coll.), Eur. Phys. J. C **27** (2003) 331;
F. Boehm et al. (Palo Verde Coll.), Phys. Rev. D **64** (2001) 112001.

[35] Ch. Weinheimer et al., Phys. Lett. B **460**, 219 (1999); Phys. Lett. B **464**, 352 (1999); Nucl. Phys. B **118**, 279 (2003).

[36] A. Osipowicz et al., *Proposal KATRIN experiment*, Preprint hep-ex/0109033 (2001).

[37] S. Eidelman et al. (Particle Data Group), Phys. Lett. B **592**, 438 (2004).

[38] K. Assamagan et al., Phys. Rev. D **53**, 6065 (1996).

[39] R. Barate et al., Eur. Phys. J. C **2**, 395 (1998).

[40] H. V. Klapdor-Kleingrothaus et al., Eur. Phys. J. A **12** (2001) 147.

[41] H. V. Klapdor-Kleingrothaus et al., Phys. Lett. B **586**, 198 (2004).

[42] D. N. Spergel et al., Astrophys. J. Suppl. **148** (2003) 175;
M. Tegmark et al., Phys. Rev. D **69** 103501 (2004).

[43] M. Guler et al. (OPERA Coll.) *Experimetal proposal*, CERN-SPSC-2000-028;
M. Guler et al. (OPERA Coll.) *Status report on the OPERA experiment*, CERN-SPSC-2001-025.

[44] G. Acquistapace et al., CERN 98-02 and INFN/AE-98/105 (1998);
R. Bailey et al. *Addendum to Report CERN 98-02*, CERN-SL 99-034 and INFN/AE-99/05 (1999);
A. E. Ball et al., SL-Note 2000-063 (2000).

[45] A. E. Ball et al., CERN-EP-2001-017 (2001).

[46] R. Cappi et al.,CERN-SL-2001-032 (2001).

[47] B. Van de Vyver, Nucl. Instr. and Meth. A **385** (1997) 91.

[48] M.C. Gonzalez-Garcia and J.J. Gomez-Cadenas, Phys. Rev. D **55** (1997) 1297.

[49] A. Kayis-Topaksu et al. (CHORUS Coll.), Phys. Lett. B **549** (2002) 48.

[50] M. Komatsu, P. Migliozzi and F. Terranova, OPERA Internal Note (2004), hep-ph/0210043.

[51] M. Blau, Nature **142** (1938) 613.

[52] C. Lattes, H. Muirhead, G. Occhialini, C. Powell, Process involving charged mesons, Nature **159** (1947) 694.

[53] D. Allasia et al., Nucl. Phys. B **176** (1980) 13.

[54] N. Ushida et al., Nucl. Instr. Meth. **224** (1984) 50.

[55] S. Aoki et al., Nucl. Instr. Meth. A **274** (1989) 64.

[56] K. Kodama et al., Phys. Lett. B **504** (2001) 218.

[57] A.J. Apostolakis et al., Appl. Phys. **8** (1957) 9.

[58] S. Aoki et al., Nucl. Instr. Meth. B **51** (1990) 466.

[59] S. Aoki, Nucl. Instr. Meth. A **473** (2001) 192.

[60] G. Rosa et al., Nucl. Instr. Meth. A **394** (1997) 357.

[61] G. Sirri, *Automatic scanning of emulsion films for the OPERA experiment*, PhD Thesis, Bologna (2003).

[62] FEDRA home page: http://ntslab01.na.infn.it/fedra.

[63] E. Barbuto et al., Nucl. Instr. Meth. A **525** (2004) 485.

[64] K. Kodama et al., Review of scientific instruments, vol.74 n.1, (2003).

[65] H.A. Bethe, Phys. Rev. **89**, 1256 (1953).

[66] V.L. Highland, Nucl. Instrum. Methods 129, **497** (1975);
Nucl. Instrum. Methods 161, **171** (1979).

[67] GEANT 3.21 Pakage, CERN Program Library W5013 (section PHYS334).

[68] ORFEO home page: http://people.na.infn.it/ marotta/ORFEO.

[69] M. De Serio et al., Nucl. Instr. Meth. A **512** (2003) 539.

Acknowledgments

At the end of this work I would like to thank, first of all, Giovanni De Lellis for his professionality in the organization of the test beam and fruitful discussions. I acknowledge the whole Napoli scanning Lab. for providing part of the pion data, and the Neuchatel and Bari Labs. for the sharing of electron data. I also thank Valeri Tioukov and Alberto Marotta for their support in the software business and Cristiano Bozza for his crucial intervention in on-line related problems.

Of course I have to thank the whole Bologna group, especially Gabriele Sirri and Luigi Salvatore Esposito, without them this thesis would not have been possible.